FLORIDA STATE UNIVERSITY

COLLEGE OF ARTS AND SCIENCES

THE STUDY OF BEAM-RECOIL POLARIZATION OBSERVABLES FOR $\gamma p \to K^0\Sigma^+$

By

JOSE FRANCISCO GONZALEZ LEDESMA

A Thesis submitted to the
Department of Physics
in partial fulfillment of the
requirements for the degree of
Master of Science

2020

Jose Francisco Gonzalez Ledesma defended this thesis on July 3, 2020.
The members of the supervisory committee were:

Volker Credé
Professor Directing Thesis

Simon Capstick
Committee Member

Sean Dobbs
Committee Member

The Graduate School has verified and approved the above-named committee members, and certifies that the thesis has been approved in accordance with university requirements.

“Let us *confine* ourselves, therefore, to the purification of our opinions and value judgements, and to the creation of our own original standards of goodness – but let us no longer brood over the ‘moral worth of our actions’! Yes, my friends! The time has come for us to turn away in disgust from all this nonsense of some standing in moral judgement over others! The whole thing is in such bad taste! Let us leave this nonsense and this bad taste to those who have nothing better to do than to keep the past alive a little bit longer and who never live in the here and now – let us leave them to the many, to the great majority! We, however, *want to become who we are* – something new, unique, incomparable, self-legislating and self-creating! And to that end, we must become the best students and discoverers of all the laws and necessities in the world. We must be *physicists* in order to be *creators* in that sense – whereas hitherto all value judgements and ideals have been based on an ignorance of physics, or in contradiction with it. And so I say, hurrah for physics! And an even louder hurrah for that which impels us to it – our honesty.”

-Friederich Nietzsche, *The Joyous Science.*

ACKNOWLEDGMENTS

Every journey has a beginning, a middle which builds up to a crescendo, only to eventually coalesce into a final state of being. Consequently, this thesis is *no* different. A project of this scope cannot by definition be the intellectual product of one person alone, but instead relies on the collected efforts of many, of those whose brilliance, diligence, tenacity and struggles inherent to their life's work resulted in the theoretical edifice whose fruits we enjoy (and continue building upon), on whose shoulders we stand to make scientific progress, large or small. To all of those who came before me, near and far, here and gone, I thank you, for this wonderful field of Physics is one of the most human, most pure and most wondrous of endeavors that represents who we are as a species.

That being said, this work could never have transpired beyond the abstract confines of the imagination into reality were it not for the support and encouragement of many wonderful people. At Florida State I wish to thank my research advisor, Dr. Volker Credé, for his support, guidance, patience and kindness as I entered the realm of hadronic spectroscopy, and graduate school. I've been fortunate to be apprenticed to one who is not only extremely knowledgeable about his field, but also very understanding about one's own struggles. Volker cares very much for each and every one of his students and their future success, and that is something I shall miss dearly as I leave FSU. Thank you for providing me with the opportunity to become a better researcher, and scientist.

To Dr. Simon Capstick, I thank you for welcoming my family and I into Florida, and for the enthusiasm, kindness and support that you provided me with while being a graduate student within the Physics Department; you were the first person I met in Florida, and I would not have had it any other way. To Dr. Jorge Piekarewicz, thank you for your friendship, advice, candor and discussions on Physics and otherwise; I shall miss you, vising your office, and our many fruitful conversations.

I wish to thank my professors at FSU for making their courses rigorous, yet accessible, and for doing each of their subjects justice and providing me with invaluable tools that shall serve me well as I move on to the next chapter of my graduate education. From Dr. Bonesteel's Quantum Mechanics and Dr. Manousakis' Statistical Mechanics, to Dr. Reina's Quantum Field Theory and Dr. Dobbs' Hadronic Physics; thank you all for your dedicated efforts as professors of Physics, and for exposing me to some of the most fascinating ideas and subjects that I've ever had the pleasure of knowing and learning about.

To my fellow graduate students: Edmundo Barriga, Jason Barlow, Ashley Ernst, Eilens Lopez, Mehmet Kaplan, Jesse Hernandez, Lawrence Ng, Caleb Benetti, Gabriel Rodriguez, Alicia Remington, Ronald Meledrez, Robert Stewart, Luz Vela, and Ruojun Wang, thank you all for your friendship, advice, support and for making me a better physicist. From my first year cohort I thank Mari Gogilashvili for her continuous help with the arduous assignments that every first year Physics grad student must gruel with; from Theoretical Dynamics to QFT, I wouldn't have done as well as I did without her support. To Jing Lu, thank you for helping me navigate my first semester as a TA. To Irene Roman and Joey Guzman, thank you for helping my family and I familiarize ourselves with Tallahassee, and for providing your time and friendship while I was at FSU.

Tackling a CLAS analysis is no simple feat, especially when you have little familiarity with its most popular languages, C++ and ROOT. I wish to specially thank Gabriel Rodriguez, Edmundo Barriga, Tianqi Hu and Dr. Zulkaida Akbar, for helping me with my many questions to start and execute a physics analysis. Particularly, I'd like to immensely thank the recently graduated Dr. Ashley Ernst for all of her incredible help, not only in getting me started with my analysis, but in helping me see it through, and for making me understand that being a good graduate student doesn't mean that one has to know and have all of the answers to every problem. The progress I made towards the work presented within this thesis would *not* have been possible *without* her help.

With regards to the Maximum Likelihood portion of my analysis, I wish to thank Dr. Shankar Adhikari, currently at the Jefferson Lab, for all of the extremely useful discussions, in person and otherwise, that allowed me to employ the Maximum Likelihood technique to my work.

To the amazing professors I had as an undergraduate student at Cal Poly, to my first research advisor Dr. Jennifer Klay and my Senior Project mentor Dr. Thomas Gutierrez, thank you both for your support and advice over the years; to my second research advisor Dr. Matthew Mewes, thank you for your friendship, and teachings. To all other professors and peers I knew, my dear *Physics family* at Cal Poly, I thank you all for your friendship, support, for believing in me, and for making my undergraduate years some of the best I have ever had.

To my extraordinary high school Physics teacher, Josh Thompson, thank you for being the catalyst that propelled me to the path of science in America. Thank you for your contagious enthusiasm for learning and philosophizing all things Physics. Attending Cal Poly *and* pursuing Physics were both your suggestions, and looking back on it, I'm so glad I took your advice to *heart*.

Closer to home, my most *heartfelt* thanks goes to my parents Francisco and Bertha Gonzalez, for each and every single sacrifice they have ever made for me, and continue making. From leaving everything they ever knew behind to bring my siblings and I to America for a *better* future, to the strong emphasis they always made on the importance of having an education and working hard to achieve one's dreams. To my father, the *strongest* man I've ever known, thank you for instilling in me a pleasure for finding things out, and for Science. Thank you for tutoring me in math, and *awakening* my scientific spirit. To my mother, thank you for always making sure I finished my homework, making my meals, taking me to school, making sure I had a clean home environment in which to study, reading to me at night, and for always taking an interest on how every single one of my school days went, something you still do even to this day. To *both* of my parents, thank you for your boundless love and support, and from the bottom of my heart, I hope to make you proud. I would not be where I am *without* you. *Con mucho amor y cariño, su hijo Francisco.*

To my dear siblings Alejandro and Berthita, thank you for all of the wonderful childhood memories I made with you (and our former dear dog, perrustis). I miss both of you dearly, and I'm very proud to see how much you have achieved, and will continue achieving. Your love, friendship and support are never lost on me; thank you for being the best siblings one could ask for.

To Diane Englund, Dr. Camille O'Bryant, Dr. Philip S. Bailey, and my friends and former undergrad peers: Melanie Goble, Max Yarbrough, Caroline Paciaroni, Ben Miller, Carlos Alas, Alex Kemnitz, Sophie Ford, Mady Larkin, Adeel Ali, Sara Jones and Eddy Bañuelos, I thank you all for your friendship, support, and providing much help to my wife and I when our daughter was born, and in our most *desperate times* of need; without you, things would've been much *harder*.

And last, but *not least*, I want to thank my *life-long partner*, my best friend and the *love* of my life, my beautiful wife Sierra Gonzalez. You complete me and have supported me in all of my dreams and goals since the day we met, I could not have asked for a more selfless and wonderful partner than you. Thank you so much for everything you have done, and continue doing every day for me. Thank you for your love and care, and for putting up with the long, arduous and complicated life of an aspiring physicist; *accomplishing my dreams would not be possible without you darling; I love you.* And *most importantly*, this thesis is dedicated to our *beautiful* daughter, *Josephine Francesca Gonzalez*, who fills my life with love, strength, meaning, and is my reason for being. *Con muchísimo amor y cariño, para mi hermosa hija Josephine; con amor siempre, tu papá.*

TABLE OF CONTENTS

LIST OF TABLES

LIST OF FIGURES

ABSTRACT

The realm of hadronic spectroscopy offers a window into the inner workings of quark-gluon interactions within hadrons, while providing new insights into the existence of excited hadrons. The knowledge gained from the further study of baryon resonances are manifold, as they proffer a deeper understanding of strong interactions hitherto unknown and glimpsed only through the properties of the ensuing excited baryon states. Moreover, the study of these excited states is a well-established tool implemented to further understand the non-perturbative (low-energy) regime of Quantum Chromodynamics (QCD).

Nonetheless, even after decades of intense theoretical and experimental investigations, most of the predicted excited resonance states proposed by different theoretical programs, including Lattice QCD and Constituent Quark Models (CQM), have yet to be experimentally confirmed. Current theoretical calculations predict a greater number of baryon resonances than what has actually been observed. This disagreement between models and experimental studies in hadronic physics is known as the *missing baryon problem*.

The missing resonances are excited state particles that decay quickly, and might be responsible for filling in the intermediate steps in processes such as $\gamma N \to N^* \to YZ$. Excited nucleon states are typically found in broadly overlapping (across a wide range of masses and spin-parity combinations J^P) resonances, such as N^* states (these have the potential to decay into a plethora of final-states YZ composed of baryons and mesons), which can account for the intermediate particle involved in the reaction. Consequently, these states are difficult to isolate via the use of cross-sectional data alone. Therefore, it becomes necessary to introduce a set of *polarization observables*, as they are an instrumental tool in the disentanglement process of contributing single resonant and non-resonant amplitudes, leading to the identification of the missing baryons. It is theorized that Nucleon (N^*) resonances can decay into final-state pairs like the ΛK or $K\Sigma$ channels.

The data employed in this thesis was recorded at the Thomas Jefferson National Accelerator Facility (JLab) under the CLAS $g12$ experiment as part of their N^* spectroscopy program, via the use of the CEBAF Large Acceptance Spectrometer (CLAS) detector. This experiment recorded photoproduction data from the application of a circularly-polarized photon beam incident on an unpolarized liquid Hydrogen (lH_2) target, using a photon energy range of $1.1 < E_\gamma < 5.4$ GeV.

In this work we determined the beam-recoil polarization transfer observables C_x and C_z, as well as the hyperon-recoil polarization observable P, for the photoproduction reaction $\gamma p \to K^0\Sigma^+$, within the energy range $1.15 < E_\gamma < 3.0$ GeV. Each of the aforementioned observables $\{C_x, P, C_z\}$ were extracted individually via the use of a linear fit, and simultaneously via the implementation of a Maximum Likelihood fit.

The main motivation behind studying the photoproduction reaction $\gamma p \to K^0\Sigma^+$ stems from the fact that it is relatively understudied amongst the other isospin-related $K\Sigma$ channels. Furthermore, the $K^0\Sigma^+$ final-state has no published measurements of its double-polarization observables, thus the work herein presented will be the first of its kind in providing results for the observables C_x and C_z, which will in turn aid in the determination of contributing baryon resonances.

CHAPTER 1

INTRODUCTION

Humans are an inquisitive species. Not easily satisfied with meek and superficial explanations about the workings of our enveloping existence, we have, since time immemorial, sought to expand our horizons of reality, peeling away the layers of uncertainty from the veils obscuring our senses to an objective existence. And after generations of unrelentingly questioning and proving nature, humanity's greatest intellectual achievement gave birth to the *Standard Model* of particle physics.

Armed with this magnificent theoretical framework, physicists have catalogued and separated the building blocks of our Universe into three distinct *families* of particles: two families of matter particles, *quarks* and *leptons*, and one family of force carrier *mediator* particles (also known as *gauge bosons*). There are a total of six leptons (e, ν_e, μ, ν_μ, τ, ν_τ), and six anti-leptons, which naturally fall into three distinct *generations* classified in accordance to their charge, electron number, muon number, and tau number. Similarly, there are a total of six quarks (u, d, c, s, t, b), and anti-quarks, which come in six distinct *flavors* and are classified according to their charge, strangeness, charmness, bottomness, topness, upness, and downess. These quarks also fall into three distinct generations as well and come in three distinct *colors* (red, blue, green) each (here, color does not have the more traditional meaning of *visible* color but rather serves as an *analogue* of the electric charge). Naturally, each color has an *anti-color* counterpart as well.

The interactions between particles are mediated by the exchange of *bosons.* Bosons posses integer *spin* in units of $\hbar$, and adhere to *Bose-Einstein statistics*, while *fermions* (i.e. quarks, baryons and leptons) possess half-integer spin in units of $\hbar/2$ and are governed by *Fermi-Dirac statistics.* In contemporary particle physics, each force is mathematically described by a renormalizable gauge-invariant *Quantum Field Theory* (QFT), with the exception of gravity as we still lack a theory of *quantum gravity.* The spin-1 photon is the mediator for the *electromagnetic force*, while the charged $W^{\pm}$ bosons, along with the electrically neutral Z boson, mediate the *weak force.* As for the *strong force*, its mediating particle is the *gluon* which, like the photon, is massless. The QFT utilized to describe quark-gluon interactions is given the name of *Quantum Chromodynamics* (QCD). Due to the nature of QCD interactions, quarks *cannot* be observed as free particles (since all naturally occurring particles are *colorless*), but instead are always found confined in bound states known as *hadrons*. Hadrons can be categorized into two distinct families based on their intrinsic spin: *baryons* (bound states consisting of three quarks with half-integer spin, i.e. fermions) and *mesons* (bound states consisting of a quark/anti-quark pair and integer spin).

However as things currently stand, QCD does not have an analytic solution within its *low energy* (also known as *non-perturbative*) regime. As a consequence, physicists have developed techniques in order to study Nucleons within this non-perturbative regime. *Baryon Spectroscopy* is one of said tools, and it is employed to study excited Nucleons in an attempt to gain further insights into how the dynamics of quarks and gluons give rise to the rich spectrum of hadrons, and the inner-workings of the strong interaction.

In this thesis, we shall make use of Baryon Spectroscopy in order to extract a set of *polarization observables*, which are of crucial importance for isolating single-resonance contributions from interfering excited baryon states.

1.1 Quantum Chromodynamics

The Universe as we know it is governed by four distinct forces of nature (listed in order of decreasing strength): *strong*, *electroweak*, *electromagnetic* and *gravitational*. Each of these fundamental forces (excluding gravity) is described in terms of a Quantum Field Theory. For the strong force there is Quantum Chromodynamics (QCD), a gauge field theory with an underlying $SU(3)$ symmetry, used to describe the interactions between colored quarks and gluons. The quarks have the distinction of being the *irreducible fundamental representations* of the $SU(3)$ color group algebra (one can think of color as a label for the three distinct orthogonal states that inhabit the $SU(3)_c$ color space). The corresponding *Lagrangian density* for Quantum Chromodynamics is given by,

$$\mathscr{L}_{\text{QCD}} = \sum_q \bar{\psi}_{q,a}\big(i\gamma^\mu \partial_\mu \delta_{ab} - g_s \gamma^\mu t^C_{ab} \mathscr{A}^C_\mu - m_q \delta_{ab}\big)\psi_{q,b} - \frac{1}{4} F^A_{\mu\nu} F^{A\,\mu\nu}, \tag{1.1}$$

where we use the convention of summing over repeated indices, γ^μ denotes the Dirac γ-matrices, $\psi_{q,a}$ are quark-field spinors representing a quark with flavor q, mass m_q and color-index a (running from 1 to $N_c = 3$, since there's three colors for quarks), and $\mathscr{A}^C_\mu$ represents the gluon fields (with C spanning 1 to $N_c^2 - 1 = 8$, since there are eight different kinds of gluons). Furthermore, the t_{ab}^{C} correspond to the generators of the $SU(3)$ group, which are represented by eight 3×3 matrices (known as the *Gell-Mann matrices*; they are to $SU(3)$ what the *Pauli spin matrices* are to $SU(2)$), and serve to indicate the fact that a gluon interacting with a quark can *rotate* the quark's color within $SU(3)$ space. Of great importance is also the quantity g_s, known as the *coupling constant*, which dictates the strength of the interaction among particles subject to QCD. The coupling constant g_s, along with the mass of the quarks m_q, are the fundamental parameters of QCD. Lastly, the field strength tensor $F_{\mu\nu}^{A}$ is defined via,

$$F_{\mu\nu}^{A} = \partial_\mu \mathscr{A}_\nu^A - \partial_\nu \mathscr{A}_\mu^A - g_s f_{ABC} \mathscr{A}_\mu^B \mathscr{A}_\nu^C, \tag{1.2}$$

where f_{ABC} are the *structure constants* of the $SU(3)$ symmetry group and are defined via the commutator relation of the Gell-Mann matrices,

$$[t^A, t^B] = i f_{ABC} t^C. \tag{1.3}$$

While the intrinsic theory of QCD seems to have similar foundations to those of QED (the QFT responsible for the electromagnetic force binding the constituent amounts of an atom, electrons and nucleons), the nature of QCD is intrinsically richer as it replaces the single charge of QED by three distinct colored charges. Furthermore, while for QED charged particles interact amongst each other via the exchange of photons, they *cannot* interact amongst themselves, since photons are neutrally-charged particles; on the other hand, the gluons responsible for mediating the strong interactions between quarks *can* in fact interact with each other since they are *not* color-neutral. This is a direct consequence of the non-commuting nature of the $SU(3)$ algebra, due to the presence of the additional term ($g_s f_{ABC} t^C$) in the field strength tensor $F_{\mu\nu}^{A}$ (1.2), which is responsible for giving rise not only to quark and anti-quark interactions, but also to the aforementioned gluon self-interactions. As such QCD is said to be a *non-Abelian* gauge theory. It is this theoretical framework that describes the strong interaction amongst hadrons (composed of a concoction of quarks and gluons).

By its very nature the strong force exerts a short-range influence with the particular property of varying rapidly as a function of *distance*. A profound consequence of gluon self-interactions is *color confinement*, defined as the constraining of colored objects to color *singlet* states (baryons and mesons) so that no objects with non-zero color charge can freely propagate. This peculiarity of QCD is hardwired within the underlying structure of its *strong coupling constant*, α_S.

It is a known fact from QED that the strength of the electromagnetic force is encoded within the ubiquitous and dimensionless *fine-structure constant*,

$$\alpha = \frac{e^2}{4\pi} \approx \frac{1}{137}. \tag{1.4}$$

Due to the low-value of this coupling constant α, one can bring the powers of perturbation theory to bear on QED calculations. The story is a bit more complicated in the case of QCD, since the value of its coupling constant depends on the energy scale of the interaction under consideration, making α_S an *energy-dependent* parameter (since α_S depends on the momentum transfer q^2). As such, this behavior effectively *divides* QCD into two distinct energy *regimes* as the momentum transfer q^2 becomes *large* or *small*. At sufficiently *high-energies*, α_S takes on a *small* enough value so as to render perturbation theory a viable tool to use. Phrased differently, the strong coupling constant vanishes asymptotically at short distances, such that the attraction between quarks grows weaker as one approaches the other. This particular property of QCD is known as *asymptotic freedom*, a behavior proposed by David Gross and Frank Wilczek, and also independently by David Politzer, in 1973. Their magnificent accomplishment was awarded the 2004 Nobel Prize in Physics.

On the other hand, at *low-energies*, α_S takes on *large* values exponentially, such that at long distances color confinement becomes an emergent property. It is within this energy-regime that the large value of α_S prevents the separation of a hadron into its constituent quarks. Thus, the philosophy of confinement lies in the idea that the strong force binding the quarks together does not decrease as a function of distance. Currently there exists no analytic proof for color confinement as this occurs in the non-perturbative regime of QCD.

Lastly, using perturbation theory in the high-energy regime of QCD, the energetic evolution of the strong coupling constant α_S is given by [26],

$$\alpha_S(|q^2|) = \frac{\alpha_S(\mu^2)}{1 + [\alpha_S(\mu^2)/12\pi](11n - 2f)\ln(|q^2|/\mu^2)}, \tag{1.5}$$

where $|q^2| \gg \mu^2$, n represents the number of colors, and f is the number of flavors. For any theory in which $11n > 2f$, an *antiscreening* effect (since gluons can interact amongst themselves) dominates such that the strong coupling constant decreases as the momentum transfer $|q^2|$ increases, which renders the so-called strong force weak at short distances. This is the basis for asymptotic freedom. Figure 1.1 is a summary of α_S as a function of momentum transfer extracted from various high-energy experiments.

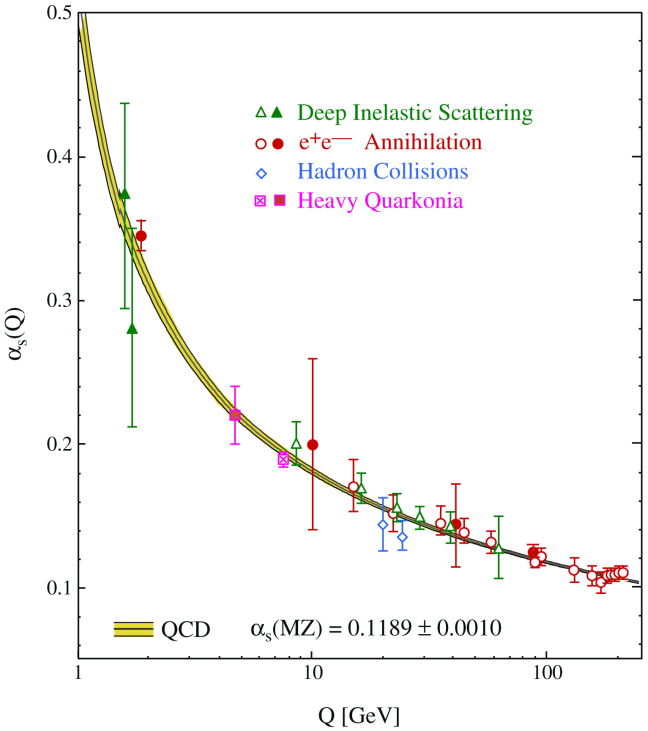

Figure 1.1: Measurements of the strong coupling constant α_S as a function of the momentum transfer Q, from different experiments. The curves represent QCD predictions from world-average values of α_S. The open (closed) circles represent next-leading-order (next-next-leading-order) QCD calculations used in the extraction of α_S. These results prove a direct confirmation of the theoretically expected behavior of QCD at high-energies (large momentum-transfers), i.e. the predicted decrease in α_S as Q increases is observed. Image source: [6]. Licensed under CC BY-NC-ND 4.0.

1.2 Hadron Properties and Nomenclature

Hadrons are particles subject to the strong force, which is mathematically described by QCD. The building blocks of this field theory constitute the quarks and the gluons (the force carriers). Hadrons are divided into two categories: *baryons* and *mesons*. The nomenclature for hadrons is structured in accordance to their mass and a set of quantum numbers: isospin (I), total spin (S), total orbital angular momentum (L), total angular momentum (J), parity (P), flavor and charge conjugation (C). These quantum numbers can be used to build baryon and meson states.

Introduced by Heisenberg in 1932, *isospin* tells us the number of distinct charged states of the same particle that exist within nature. For a given isospin I, there are a total $(2I{+}1)$ particles in a hadronic multiplet state. The total angular momentum $\vec{J}$ can be determined by the vector addition of the total spin $\vec{S}$ and total orbital angular momentum $\vec{L}$. As such, J can only take on values constrained within the range $|L - S| \leq J \leq |L + S|$. In the early days of hadronic spectroscopy, physicists used the particular values of S, L and J, to name hadronic states based on the atomic spectroscopy notation, ${}^{2S+1}L_J$ (as an example, one uses s for $l = 0$ and p for $l = 1$).

The *parity* operator P is an example of a discrete symmetry transformation, corresponding to the spatial inversion of a set of coordinates through their origin. Applying the parity operator twice takes a discrete transformation back to its starting point ($P^2 = \mathbb{1}$). Hence, the eigenvalues of P are ± 1. Scalars and pseudovectors have an eigenvalue of $+1$, while pseudoscalars and vectors have eigenvalue -1. Furthermore, the parity operator P serves as a good quantum number for hadrons. As for the mesons, and due to the fact that they are composed of a fermion/anti-fermion pair, their intrinsic parities are opposite, resulting in them having a parity of $P = (-1)^{L+1}$. Baryons have a parity of $P = (-1)^L$; it thus follows that the ground state baryons ($L = 0$) have positive parity.

Next we have the flavor quantum number, which simply refers to quark content. The six known quarks can be further split up into two different classes, the *light quarks*, (u, d, s), and the *heavy quarks* (c, b, t). Furthermore, since gluons are flavor neutral, it follows that, while the strong force is flavor independent, it is color dependent. Next is the *charge conjugation* operator C, which has the peculiar property of turning a particle into its own antiparticle. Similar to the parity operator P, a double application of C brings one back to the original state, since $C^2 = \mathbb{1}$; consequently, it has eigenvalues of ± 1. However, only those particles which are their *own* antiparticles can be eigenstates of C. For hadrons, the neutral mesons fit this prescription, thus making C a good quantum number for said particles; their charge conjugation is $C = (-1)^{L+S}$. Lastly, the applicability of C can be extended to the charged (non strange, non baryonic) states as well, by defining the *G-parity* operator (a 180° rotation about I_2 in isospin space, followed by the application of C) as $G \equiv Ce^{i\pi I_2}$.

Therefore, the nomenclature for hadrons is the following: for baryons, their quark content and isospin I are sufficient labels to give them an unambiguous symbol. As an example, consider a delta baryon Δ, with three u and/or d quarks, and isospin $I = 3/2$. All delta states are represented as $\Delta(\text{mass})J^P$, with the Δ ground state being $\Delta(1232)3/2^+$, where 1232 is the Δ mass (in MeV/c^2). For mesons, mass (in MeV/c^2), quark content and quantum numbers I, J^{PC} are enough to specify their symbol. Consider for instance the pion mesons (of relevance to this body of work) π. Their nomenclature would have them denoted as $J^{PC} = 0^{-+}$, with a given mass of roughly 140 MeV/c^2.

1.3 Baryon Spectroscopy

The realm of *hadronic physics* belongs to an extensive field of research which concerns itself with the study of matter at a fundamental level. In some sense, it sits at the boundary of high-energy particle and nuclear physics, as it adopts the reductionist approach of the former, while adopting an interest in the underlying *structure* of composite particles from the latter.

The intrinsic energy dependence of QCD renders it immune to a regular perturbative theory approach in the low-energy regime. As such, one cannot predict the spectra of baryons using perturbation theory *alone*. In order to circumvent said issue, physicists developed techniques to study QCD in the form of *baryon spectroscopy*. This consists of mapping and studying the spectrum of all excited states (known as *resonances*). It is also a superb tool for studying the dynamics responsible for color confinement. Similar in spirit to atomic spectroscopy (where one studies atoms by observing their decay spectrum), baryon spectroscopy comprises of exciting the ground state of a Nucleon via the use of a high-energy particle beam (using electrons, photons, or pions), thus resulting in radiation in the form of γ's, K's, Σ's, π's, among other particles.

The overarching goals of baryon spectroscopy are concerned with achieving an understanding of all relevant degrees of freedom within a baryon, and unraveling the mystery of how the strong quark-gluon interactions give rise to the excited hadron states observed in nature. Therefore, by analyzing the properties of the emerging excited baryon states, physicists can construct hypothetical models in order to account for their observations. Generally speaking, the full wavefunction of a baryon state, accounting for all its degrees of freedom, may be written as [64],

$$\Psi = \Psi_{\text{flavor}} \Psi_{\text{spin}} \Psi_{\text{color}} \Psi_{\text{space}}, \tag{1.6}$$

where each wavefunction component describes, respectively, the flavor, spin, color and spatial properties of the baryon in question. Since quarks are fermions, the overall wavefunction of a baryon is required to be *antisymmetric* under the exchange of any two of its constituent quarks. Furthermore, since all observed hadrons are color singlets, then the baryon color wavefunction (Ψ_{color}) *must be* totally antisymmetric. Hence, the remaining portion of the wavefunction, $\Psi_{\text{flavor}} \Psi_{\text{spin}} \Psi_{\text{space}}$, must be symmetric under the exchange of any pair of identical quarks. Two important models used to explain and describe the underlying dynamics within hadrons, and their spectra, include the *Constituent Quark Model* (CQM) and *Lattice QCD*, which we now briefly recount.

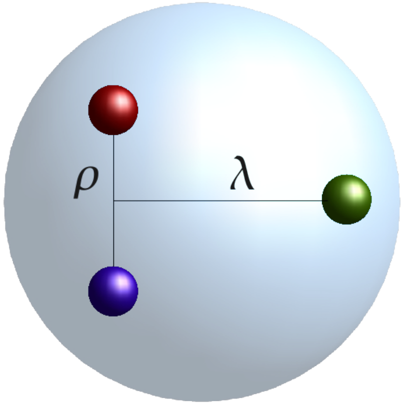

Figure 1.2: A baryon as described by the Constituent Quark Model (CQM). Here, a baryon consists of three quarks bounded by two independent harmonic oscillators ρ and λ. Image source: [27]. Courtesy of Dr. Charles Hanretty (Jefferson Lab).

Constituent Quark Model (CQM). This model assumes that quarks move in a harmonic oscillator potential. This potential is chosen due to its simplicity in allowing to separate the center of mass motion by a choice of suitable coordinates describing two harmonic oscillators ρ and λ (see Figure 1.2). Thus, a baryon is treated as a system with three constituent quarks acting as its degrees of freedom; its spatial wavefunction (Ψ_{space}) is described by the Jacobi-coordinates of the oscillators ρ and λ. The sum of the constituent quark masses (with the appropriate binding energy corrections) is enough to account for the baryon mass. The energy of this 3-quark system is,

$$E = (N+3)\hbar\omega, \tag{1.7}$$

where the total quantum numbers N of an excited baryon are $N = 2(n_\rho + n_\lambda) + l_\rho + l_\lambda$, l_ρ and l_λ denote the orbital angular momentum of the oscillators ρ and λ, while n_ρ and n_λ denote the radial excitation and $\omega = \sqrt{3k/m}$. The light-flavor quarks (u, d, s) can be dealt with using an approximate $SU(3)_{\text{flavor}}$ group symmetry framework. This symmetry is approximate since the mass of the strange quark is different from the masses of the up and down quarks; nonetheless, the mass difference between m_{s} and $m_{\text{u/d}}$ is relatively small (on the order of 100 MeV) compared to typical binding energies of baryons (on the order of 1 GeV) [64]. Furthermore, the flavor and spin groups ($SU(3)_{\text{flavor}}$, $SU(2)_{\text{spin}}$) can be combined into an approximate spin-flavor group $SU(6)_{\text{flavor}\times\text{spin}}$, such that the resulting multiplet states stemming from combining the light-flavor quarks are,

$$\mathbf{6}\otimes\mathbf{6}\otimes\mathbf{6} = \mathbf{56}_S \oplus \mathbf{70}_M \oplus \mathbf{70}_M \oplus \mathbf{20}_A, \tag{1.8}$$

where S, M and A denote *symmetric*, *mixed* and *antisymmetric* wavefunctions. The $SU(6)_{\text{flavor}\times\text{spin}}$ spin-flavor group can be decomposed into $SU(3)$ flavor decuplet and octet multiplet states,

$$\mathbf{56} = {}^4\mathbf{10} \otimes {}^2\mathbf{8} \tag{1.9a}$$

$$\mathbf{70} = {}^2\mathbf{10} \otimes {}^4\mathbf{8} \otimes {}^2\mathbf{8} \otimes {}^2\mathbf{1} \tag{1.9b}$$

$$\mathbf{20} = {}^2\mathbf{8} \otimes {}^4\mathbf{1}, \tag{1.9c}$$

where the superscript $(2S+1)$ denotes the total spin-projections for each $SU(3)$ multiplet. Ground state baryons ($N = 0$) (proton, neutron, Δ) belong to the **56**plet, where the angular momentum between any constituent quarks is zero. These ground states are further decomposed as follows: protons/neutrons have 8 members with two spin-1/2 projections (${}^2\mathbf{8}$) and spin/parity $J^P = \frac{1}{2}^+$; the Δ baryons have 10 members with four spin-3/2 projections (${}^4\mathbf{10}$) and spin/parity $J^P = \frac{3}{2}^+$ (see Figure 1.3). Baryons can thus be cataloged into different *excitation bands* based on the quanta of excitation N. Each supermultiplet is specified by ($\mathbf{D}$, L^P_N), where $\mathbf{D}$ is the dimensionality of the representation (**56**, **70**, **20**), L is the total angular momentum and P is the parity. The spectra of Nucleon (N^*) and Delta (Δ^*) resonances can be constructed by applying the symmetric/antisymmetric properties of the spatial and $SU(6)$ multiplet wavefunctions. Thus, for the CQM the hadronic spectrum stems from the harmonic oscillator potential and the angular momentum.

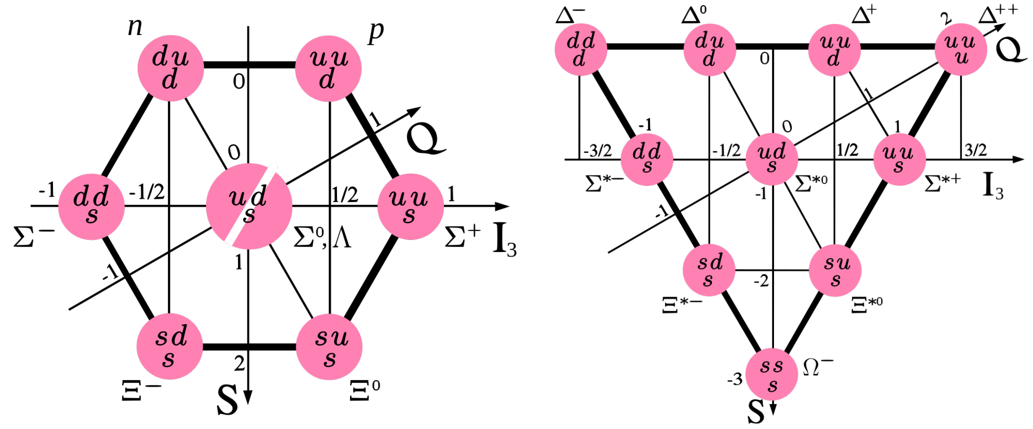

Figure 1.3: Ground state baryons ($N = 0$). (Left): Baryon octet (${}^2\mathbf{8}$) for spin-1/2 ground state baryons. (Right): Baryon decuplet (${}^4\mathbf{10}$) for spin-3/2 ground state baryons. Q represents the electric charge, S is strangeness, and I_3 is the third component of isospin. Image source: Wikipedia.

Lattice QCD. Currently, the only *ab initio* approach to the non-perturbative regime of QCD relies on *lattice simulations* [17]. This approach discretizes QCD within its non-perturbative regime on a space-time lattice, allowing for the extraction of an approximate solution to QCD via numerical methods. The regular path-integral approach from QFT over infinitely many Minkowski space-time points is relaxed and approximated by a finite number of points over a Euclidean space lattice, by using the appropriate periodic boundary conditions. The *Minkowski metric* can be transformed into the *Euclidean metric* by a *Wick rotation*, which extends the degree of *analytic continuation* of the time variable t into the realms of a complex space ($\mathbb{C}$), into an *imaginary time* it.

In this framework, the quark fields are defined at the lattice sites, while the gluon fields are defined on the links between the lattices as 3×3 unitary matrices so as to conserve *gauge invariance*. Any result stemming from this lattice approach is extrapolated to the continuous (physical) limit of infinite box size and zero lattice spacing. Taking these limits however is problematic as they vastly increase the computational time of a lattice simulation; the finite lattice spacing produces an *ultraviolet cut-off*, while the finite-box size introduces an *infrared cut-off*. Regardless of the aforementioned limitations, recent advances in computing capabilities have allowed Lattice QCD to make significant progress in the prediction of the light baryon spectrum (see Figure 1.4), demonstrating consistency with the predictions extracted from the Constituent Quark Model.

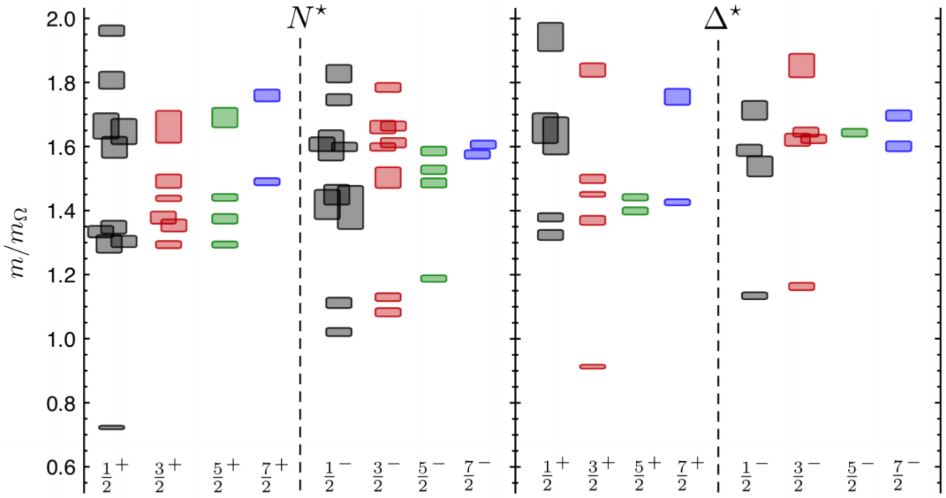

Figure 1.4: Light baryon spectrum of Nucleons (N^*) and Deltas (Δ^*) obtained via Lattice calculations from lattices at $m_\pi = 396$ MeV, spacing ≈ 0.123 fm and box-size ≈ 2 fm. Reprinted figure with permission from reference [52]. Copyright 2011 by the American Physical Society.

1.3.1 Experimental Challenges in Baryon Spectroscopy

Unlike atomic spectroscopy, whose execution in the task of finding atomic states can be achieved in a classroom, baryon spectroscopy offers more complexity and challenges in its application to find the excited states of a baryon, since it requires a particle accelerator, along with *avant-garde* machinery and detector systems. The crux of the matter lies in the fact that baryon resonances are far more unstable than their atomic counterparts, with a typical lifetime in the order of 10^{-24} s for a strongly decaying resonance. Additionally, in accordance to *Heisenberg's uncertainty principle*,

$$\Delta E \Delta t \geq \hbar, \tag{1.10}$$

the width of the resonance is inversely proportional to its lifetime. The energy width is on the order of 100 MeV, which in many cases is larger than the average separation between the baryon resonances. Consequently the ensuing baryon states *overlap*, leading to the complexity behind identifying baryon resonances. Figure 1.5 shows the contrast between atomic and baryon spectroscopy.

While atomic resonances are sharp and simple to identify within the atomic spectrum, the overlapping nature of the baryon states makes it a difficult task to tell different baryon resonance peaks apart. For instance, Figure 1.5 shows a broad peak within the center-of-mass energy range of $W \in [1.4, 1.6]$ GeV (known as the *second resonance region*) for the $\pi^- p \to X$ cross section, which is actually comprised of *three* overlapping baryon states. To complicate matters further, the interaction of photons with protons leads to the production of a host of different particles, including pions, photons, electrons, etc, whereas for atomic spectroscopy the final-state consists of photons *alone*. Furthermore at higher energies, the peaks shown in Figure 1.5 are washed out due to the highly overlapped baryon states. Due to these issues, knowledge of the unpolarized cross sections is insufficient to extract resonant contributions of a reaction under consideration, since that only grants information on the *magnitude* of the amplitudes. Therefore, to disentangle these overlapped states one needs the *phase* information from the scattering amplitudes, as well as their magnitudes. The introduction of *polarization observables* becomes an *essential* tool to untangle the overlapping baryon states, as these observables are highly sensitive to the presence of a resonance, providing knowledge of the phase of the interfering scattering amplitudes from the different baryon states. This can lead to unambiguous results for the resonant contributions to a reaction.

Additionally, since the proton can be excited with the use of different beam probes (π, γ, etc.), the resonances will couple *differently* depending on the probe. Thus, to disentangle a Nucleon (N^*,

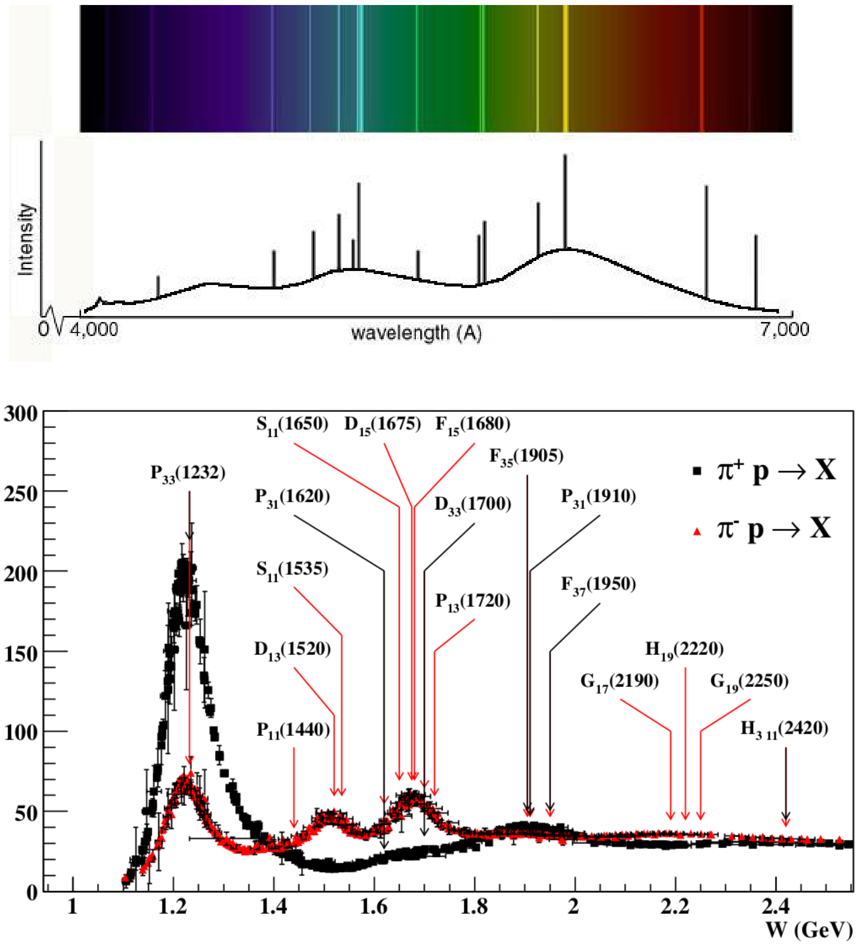

Figure 1.5: (Top): Atomic spectrum, with visible resonance peaks. Image source: [42]. (Bottom): Cross sections of π^+ and π^- scattering off a proton. Arrows show Nucleon resonances with a 4-star rating from the PDG [62]. The x-axis is the center-of-mass energy W (GeV). Resonances are labeled using the notation $L_{2I2J}(M)$, where I is the isospin, L is the orbital angular momentum of the $p\pi$ system, J is the spin, and M is the resonance mass (in MeV/c^2). Image shows baryon resonances are indeed broad and overlapping. Image source: [65]. Courtesy of Dr. Michael Williams (MIT).

$I = 1/2$) from a Delta (Δ^*, $I = 3/2$) state, an isospin filter channel, such as $K\Lambda$ ($I = 1/2$), which couples to N^* but not Δ^* states, is needed. Table 1.1 summarizes the known N^* resonances from various decay channels, including an overall and individual channel rating, highlighting the $K\Sigma$ channel of interest. While most baryon states with masses < 1800 MeV have ratings of **** to ***, the more massive states > 1800 MeV have ratings of * or **. It has been proposed that many of the higher mass states might have significant branching ratios into $K\Lambda$ or $K\Sigma$ channels [10].

Table 1.1: Status of Nucleon excited states at distinct decays channels. Two salient features from this table suggest that vector-meson photoproduction needs further exploration, and Kaon-Hyperon (KY) photoproduction channels hold promise for further analysis. Reprinted table with permission from reference [61]. Copyright 2018 by the American Physical Society.

			Status as seen in									
Particle	J^P	overall	$N\gamma$	$N\pi$	$\Delta\pi$	$N\sigma$	$N\eta$	ΛK	ΣK	$N\rho$	$N\omega$	$N\eta'$
N	$1/2^+$	****										
$N(1440)$	$1/2^+$	****	****	****	****	***						
$N(1520)$	$3/2^-$	****	****	****	****	**	****					
$N(1535)$	$1/2^-$	****	****	****	***	*	****					
$N(1650)$	$1/2^-$	****	****	****	***	*	****	*				
$N(1675)$	$5/2^-$	****	****	****	****	***	*	*	*			
$N(1680)$	$5/2^+$	****	****	****	****	***	*	*	*			
$N(1700)$	$3/2^-$	***	**	***	***	*	*			*		
$N(1710)$	$1/2^+$	****	****	****	*		***	**	*	*	*	
$N(1720)$	$3/2^+$	****	****	****	***	*	*	****	*	*	*	
$N(1860)$	$5/2^+$	**	*	**		*	*					
$N(1875)$	$3/2^-$	***	**	**	*	**	*	*	*	*	*	
$N(1880)$	$1/2^+$	***	**	*	**	*	*	**	**		**	
$N(1895)$	$1/2^-$	****	****	*	*	*	****	**	**	*	*	****
$N(1900)$	$3/2^+$	****	****	**	**	*	*	**	**		*	**
$N(1990)$	$7/2^+$	**	**	**			*	*	*			
$N(2000)$	$5/2^+$	**	**	*	**	*	*				*	
$N(2040)$	$3/2^+$	*		*								
$N(2060)$	$5/2^-$	***	***	**	*	*	*	*	*	*	*	
$N(2100)$	$1/2^+$	***	**	***	**	**	*	*		*	*	**
$N(2120)$	$3/2^-$	***	***	**	**	**		**	*		*	*
$N(2190)$	$7/2^-$	****	****	****	****	**	*	**	*	*	*	
$N(2220)$	$9/2^+$	****	**	****			*	*	*			
$N(2250)$	$9/2^-$	****	**	****			*	*	*			
$N(2300)$	$1/2^+$	**		**								
$N(2570)$	$5/2^-$	**		**								
$N(2600)$	$11/2^-$	***		***								
$N(2700)$	$13/2^+$	**		**								

****	Existence is certain.
***	Existence is very likely.
**	Evidence of existence is fair.
*	Evidence of existence is poor.

1.4 Hyperon Photoproduction

A hyperon is a baryon which contains at least a single strange (s)-flavor quark, excluding the presence of charm (c), bottom (b) and top (t) quarks. The photoproduction of strangeness off the proton, leading to a $K\Sigma$ state, is part of the field of elementary pseudoscalar meson production. Hyperon photoproduction is described fully by $2 \times 2 \times 2 = 8$ complex amplitudes [5]. However, due to constraints imposed by parity invariance, these amplitudes are reduced to only 4, which define a total of 16 experimental observables [13]. The 16 observables for Kaon (pseudoscalar) photoproduction are divided into groups based on what is polarized for a reaction: beam, target and hyperon-recoil polarization. The set of 4 *transversity amplitudes* b_i are defined by [1, 5],

$$b_1 = -\frac{i}{\sqrt{2}}(\mathcal{F}_1 - \mathcal{F}_2 e^{-i\theta_{\text{c.m.}}})e^{i\theta_{\text{c.m.}}/2} \tag{1.11a}$$

$$b_2 = \frac{i}{\sqrt{2}}(\mathcal{F}_1 - \mathcal{F}_2 e^{i\theta_{\text{c.m.}}})e^{-i\theta_{\text{c.m.}}/2} \tag{1.11b}$$

$$b_3 = -b_1 - \frac{\sin\theta_{\text{c.m.}}}{\sqrt{2}}(\mathcal{F}_3 + \mathcal{F}_4 e^{-i\theta_{\text{c.m.}}})e^{i\theta_{\text{c.m.}}/2} \tag{1.11c}$$

$$b_4 = -b_2 - \frac{\sin\theta_{\text{c.m.}}}{\sqrt{2}}(\mathcal{F}_3 + \mathcal{F}_4 e^{i\theta_{\text{c.m.}}})e^{-i\theta_{\text{c.m.}}/2}, \tag{1.11d}$$

where $\theta_{\text{c.m.}}$ denotes the center-of-mass angle in the reaction plane, and $\mathcal{F}_1 - \mathcal{F}_4$ are the Chew, Goldberger, Low and Nambu (CGLN) amplitudes [12]. The amplitudes (1.11a)−(1.11d) give a complete description of the photoproduction process. Furthermore, armed with their bilinear combinations, 16 polarization observables can be derived. Of these 16 observables, besides the unpolarized differential cross section ($d\sigma/d\Omega$), there are 3 *single*, and 12 *double-polarization observables* [50].

The first group of observables consists of the unpolarized differential cross section ($d\sigma/d\Omega$), the hyperon-recoil polarization P, the linearly polarized photon beam asymmetry Σ, and the transversely polarized target beam asymmetry T. On the other hand, the double-polarization group of observables characterize combinations where two of the reaction participants are polarized, such as beam and target, beam and hyperon or target and hyperon. Furthermore, in order to fully resolve any underlying ambiguities and uniquely determine the complex amplitudes, it is enough to measure the unpolarized cross section, the three single polarization observables, and at least four double-polarization observables [50]. Table 1.2 summarizes the aforementioned sets of observables.

The analysis presented within this thesis aims to measure the double beam-recoil ($\mathcal{BR}$) polarization observables C_x and C_z, along with the single hyperon-recoil ($\mathcal{S}$) polarization observable P, for $\gamma p \to K^0\Sigma^+$. When the photon beam is unpolarized, conservation of parity in electromagnetic interactions allows for an induced polarization P of the hyperon to arise exclusively along an axis perpendicular to the reaction plane (see Section 4.1) [50]. However, in the event that the incoming photon beam is circularly polarized, where the photons are spin polarized parallel or antiparallel to the beam direction (i.e. giving the beam a net *helicity*, defined as the normalized component of a particle's spin along its direction of flight), this polarization may be fully or partially transferred to the spin orientation of the ensuing hyperon in the reaction plane [50]. The C_x and C_z observables characterize the transfer of circular polarization from a circularly polarized photon beam to a recoiling Σ^+ hyperon along orthogonal axes defined by the scattering plane [50].

Table 1.2: The 16 spin-observables for pseudoscalar meson photoproduction, for $\gamma p \to K^0\Sigma^+$, reported in their *transversity representation*; here $\Re$ and $\Im$ denote the real and imaginary parts of the amplitudes b_i. Photon polarization is denoted l for a linearly polarized beam and c for circular polarization. $\mathcal{S}$ refers to single polarization observables, $\mathcal{BT}$ to Beam-Target observables, $\mathcal{BR}$ to Beam-Recoil observables, and $\mathcal{TR}$ to Target-Recoil observables. Axis conventions for the scattering plane (x', y', z') are given in Section 4.1. Table reprinted from [5], with permission from Elsevier.

	Polarization				
Observable	Beam	Target	Hyperon	Transverse Representation	Set
$(\frac{d\sigma}{d\Omega})$	–	–	–	$\lvert b_1\rvert^2 + \lvert b_2\rvert^2 + \lvert b_3\rvert^2 + \lvert b_4\rvert^2$	$\mathcal{S}$
Σ	l	–	–	$\lvert b_1\rvert^2 + \lvert b_2\rvert^2 - \lvert b_3\rvert^2 - \lvert b_4\rvert^2$	
T	–	y	–	$\lvert b_1\rvert^2 - \lvert b_2\rvert^2 - \lvert b_3\rvert^2 + \lvert b_4\rvert^2$	
P	–	–	y'	$\lvert b_2\rvert^2 + \lvert b_4\rvert^2 - \lvert b_1\rvert^2 - \lvert b_3\rvert^2$	
E	c	z	–	$-2\Re(b_1 b_3^* + b_2 b_4^*)$	$\mathcal{BT}$
F	c	x	–	$2\Im(b_1 b_3^* - b_2 b_4^*)$	
G	l	z	–	$2\Im(b_1 b_3^* + b_2 b_4^*)$	
H	l	x	–	$-2\Re(b_1 b_3^* - b_2 b_4^*)$	
O_x	l	–	x'	$-2\Re(b_1 b_4^* - b_2 b_3^*)$	$\mathcal{BR}$
O_z	l	–	z'	$-2\Im(b_1 b_4^* + b_2 b_3^*)$	
C_x	c	–	x'	$2\Im(b_1 b_4^* - b_2 b_3^*)$	
C_z	c	–	z'	$-2\Re(b_1 b_4^* + b_2 b_3^*)$	
T_x	–	x	x'	$2\Re(b_1 b_2^* - b_3 b_4^*)$	$\mathcal{TR}$
T_z	–	x	z'	$2\Im(b_1 b_2^* - b_3 b_4^*)$	
L_x	–	z	x'	$2\Im(b_1 b_2^* + b_3 b_4^*)$	
L_z	–	z	z'	$2\Re(b_1 b_2^* + b_3 b_4^*)$	

1.4.1 Photoproduction of $K^0\Sigma^+$

From conservation of strangeness, present in strong and electromagnetic interactions, the photoproduction of Kaons (strangeness = +1) must always be accompanied by the production of hyperons (strangeness = −1). The production of strange quarks in a particle generates an extra degree of freedom, providing new information absent from nucleon-nucleon scattering processes. For this analysis, the hyperon production channel of interest is the Σ^+ baryon, which is photoproduced off the proton and is accompanied by the production of a K^0 meson. The photoproduction of neutral Kaons offers a distinct advantage over the production of charged Kaons ($K^\pm$), given that photons cannot directly couple to the (vanishing) charge of the pseudoscalar K^0 meson. This property of neutral Kaons, coupled with the lack of $K^0\Sigma^+$ photoproduction data, lends motivation for the study and analysis of the reaction $\gamma p \to K^0\Sigma^+$. In addition, since the reactions $\gamma p \to K^+\Sigma^0$ and $\gamma p \to K^0\Sigma^+$ are isospin related channels, one requires data from both channels in order to disentangle any contributions stemming from the N^* and Δ^* resonances.

Table 1.3: Spectroscopic notation, and quark content, for the $\gamma p \to K^0\Sigma^+ \to p\pi^+\pi^-\pi^0$ reaction, adhering to the nomenclature from Section 1.2. Table compiled via use of the 2018 PDG [61].

Particle(q content)	γ	$p(uud)$	$K^0(d\bar{s})$	$\Sigma^+(uus)$	$\pi^\pm(u\bar{d}/d\bar{u})$	$\pi^0((u\bar{u}-d\bar{d})/\sqrt{2})$
$I^G(J^{PC})$						$1^-(0^{-+})$
$I(J^{PC})$	$0,1(1^{--})$					
$I(J^P)$		$\frac{1}{2}(\frac{1}{2}^+)$	$\frac{1}{2}(0^-)$	$1(\frac{1}{2}^+)$		
$I^G(J^P)$					$1^-(0^-)$	

Exploiting the fact that the $\Sigma^0(uds)$ and $\Sigma^+(uus)$ hyperons are members of an isotriplet, any coupling constant occurring in the photoproduction amplitude for the $K^+\Sigma^0$ process may be readily converted into the corresponding parameter for the $K^0\Sigma^+$ reaction. This is due to the fact that their strong coupling constants are linked by the following $SU(2)$ Clebsch-Gordan coefficient [16],

$$g_{K^0\Sigma^+p} = \sqrt{2}g_{K^+\Sigma^0p}. \tag{1.12}$$

However, developing a representation for isospin-related channels could lead to complications, as subtle interference effects could cause a set of certain contributions in one channel to be masked, while enhancing those contributions in another channel. This may be mitigated by counterbalancing the strength in the $K^0\Sigma^+$ channel via destructive interferences from other contributions [16].

CHAPTER 2

CLAS AT THE JEFFERSON LAB AND THE $g12$ EXPERIMENT

The data set used for the extraction of the set of observables $\{C_x,\ P,\ C_z\}$, for the $\gamma p \rightarrow K^0\Sigma^+$ reaction, was recorded at the Thomas Jefferson National Accelerator Facility (commonly known as the Jefferson Lab, or simply JLab) as part of the $g12$ run, using a continuous electron beam provided by the Continuous Electron Beam Accelerator Facility (CEBAF). Located in Newport News, Virginia, the Jefferson Lab (shown in Figure 2.1) is one of the 17 national laboratories funded by the United States Department of Energy (DOE).

The $g12$ experiment generated events using a circularly polarized photon beam incident upon an unpolarized liquid Hydrogen (lH_2) target, with an incident photon-energy range of $1.1 < E_\gamma < 5.4$ GeV. The *bremsstrahlung tagging technique*, hosted by the broad-range photon tagging facility at Hall B, was capable of tagging photon energies with a range of 20% to 95% of the incident electron beam energy. Within 44 days of beam time between April 1st and June 9th, 2008, over 126 TB of data was collected for the $g12$ experiment. The "g" in "$g12$" stands for *gamma* (as it is a *photoproduction experiment*), while the number "12" is indicative of the fact that it is the twelfth such experiment approved and carried out at the Jefferson Lab.

In order to detect the outgoing charged particles created by the interaction between the photon beam and the target, the CEBAF Large Acceptance Spectrometer (CLAS) detector, located in Hall B of JLab, was employed. CLAS was a nearly-4π spectrometer specifically built and optimized for hadronic spectroscopy, and the detection of multi-particle charged final-states.

At the time of the experiment, the Jefferson Lab hosted three halls, Hall A, B and C, for which the CEBAF Accelerator was capable of delivering beam energies of only up to 6 GeV. However, since then JLab has added a Hall D; consequently, the CEBAF Accelerator has also been upgraded in order to support continuous electron beams with energies of up to 12 GeV, and the CLAS detector has been replaced by the upgraded CLAS12 detector. Therefore this thesis will, in the following Sections, describe the experimental facility as it was when the $g12$ experiment was conducted.

Figure 2.1: An aerial view of the DOE's Thomas Jefferson National Accelerator Facility, located in Newport News, VA. Image source: [32]. Licensed under CC BY-NC-SA 2.0.

2.1 Continuous Electron Beam Accelerator Facility (CEBAF)

The Continuous Electron Beam Accelerator Facility (CEBAF) is an electron beam accelerator based on Superconducting Radiofrequency (SRF) technology. Built in the 1980's, the purpose behind CEBAF was to explore the confinement regime of QCD. CEBAF delivers high-luminosity electron beams to the three experimental Halls (A, B and C) at the Jefferson Lab, with an energy of up to 6 GeV, and has a racetrack geometry with a circumference roughly $\sim 7/8$ of a mile. The continuous delivery of electrons allows for the quick acquisition of data sets with high statistics, even at low currents. The CEBAF electrons are obtained by illuminating a Gallium Arsenide (GaAs) photocathode with pulsed lasers at a frequency of 499 MHz (roughly a third of the accelerator's frequency), thus resulting in 2 ns bunches of electrons. Three synchronized laser pulses are then temporarily fixed in order to simultaneously supply each Hall with an electron beam.

After being ejected from the photocathode, two of the first SRF cavities boosted the beam energy to 5 MeV, and then two accelerating modules, each containing 8 SRF cavities, boosted the energy of the electrons in the beam to a final energy with a range of $23 - 68$ MeV. Subsequently,

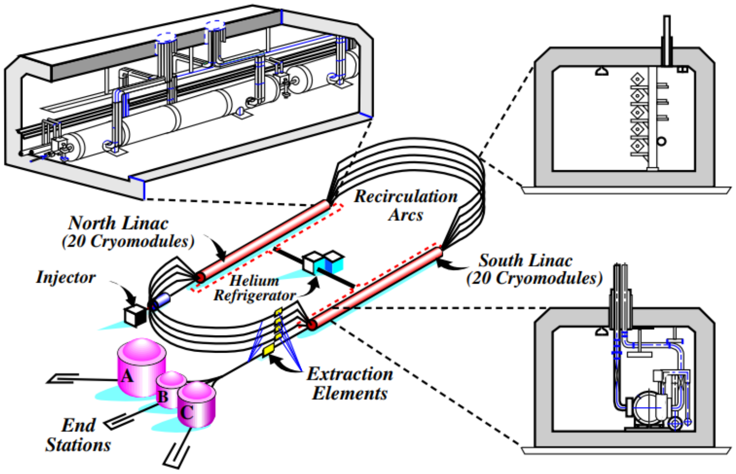

Figure 2.2: Schematic of CEBAF and its major components. Reprinted figure with permission from reference [37]. Copyright 2016 by the American Physical Society. Licensed under CC BY 4.0.

the injector system employed an optical chopper to separate the 2 ns bunches prior to sending them to the CEBAF's recirculating linear accelerators (LINACs), located along the straightaways of CEBAF's racetrack course. The two LINACs (shown in Figure 2.2) accelerated the electrons by approximately $\sim$ 600 MeV per pass. Connected by nine recirculating arcs, the LINACs allowed the electron beam to make up to five passes, achieving a maximum energy of 6 GeV.

Each recirculating LINAC consists of 21 cryomodules, and each module was equipped with 8 Niobium RF cavities, making for a total of 168 cavities per each LINAC. In order to sustain their superconductivity, each cavity was submerged in a liquid Helium bath, maintained at a temperature of 2 K. The acceleration gradient for the electron beam was induced by setting up standing radio-frequency waves within the cavities. Keeping the standing waves in phase with the ensuing electron bunches resulted on a continuous positive electric force on each bunch as they passed through a cavity (Figure 2.3). After passing through a single LINAC, the electron beam was bent using a series of dipole magnets in the recirculation arcs and directed to the other LINAC, further accelerating the electrons. The resulting beam was further divided into five sub-beams according to energy, so that electrons of different energies could be sent through a different recirculation arc before re-accessing the LINACs. Once the beam had passed through the accelerator a desired number of times, it could then be sent to one of the three appointed Halls using RF separator cavities with a 120° phase separation. The electron beam energy current for the $g12$ experiment was set to 65 nA.

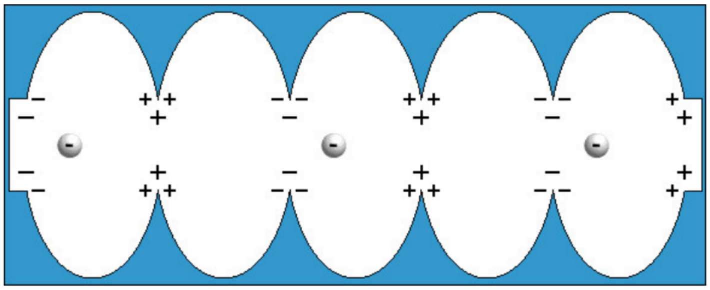

Figure 2.3: Diagram illustrating the acceleration gradient across a cryomodule. Image source: [21].

2.2 Photon Tagger

A photoproduction experiment such as $g12$ requires the use of a real photon beam. To that end, Hall B employed a tagging ("tagger") system (see Figure 2.4) to convert the incoming electron beam into a photon beam by means of *bremsstrahlung radiation*. When the electron beam comes into contact with a very thin radiator sheet, the radiator's electromagnetic field slows the electrons down, leading to the emission of photons due to energy-momentum conservation. Using a thin radiator sheet ensures that a single electron is correlated to a single photon. The $g12$ experiment employed a gold (Au) foil radiator since the high atomic number of gold aids in reducing any photon contamination produced by electron-electron scattering. Having passed through the radiator, the beam was composed of a mixture of non-interacting electrons, photons and recoil electrons.

A tagger magnetic spectrometer, producing a uniform magnetic field of 1.75 T, was used to sweep the full-energy non-interacting electrons downwards and outside of the beamline into a beam dump. The magnetic field redirected the recoil electrons towards two hodoscope planes, each composed of overlapping arrays of scintillators, to tag the energy and time of the photons produced via bremsstrahlung. Since the mass of a gold atom is much higher than that of an electron, most of the ensuing momentum is transferred into the recoil electron, while a negligible amount is transferred to the nucleus. Hence the bremsstrahlung reaction obeys the following energy conservation relation,

$$E_\gamma = E_0 - E_e, \tag{2.1}$$

where E_0 is the energy of the electron incident on the radiator, E_e is the energy of the outgoing scattered electron, and E_γ is the energy of the emitted bremsstrahlung photon. Since E_0 can be uniquely determined from the accelerator, a measurement of the outgoing recoil electron energy E_e

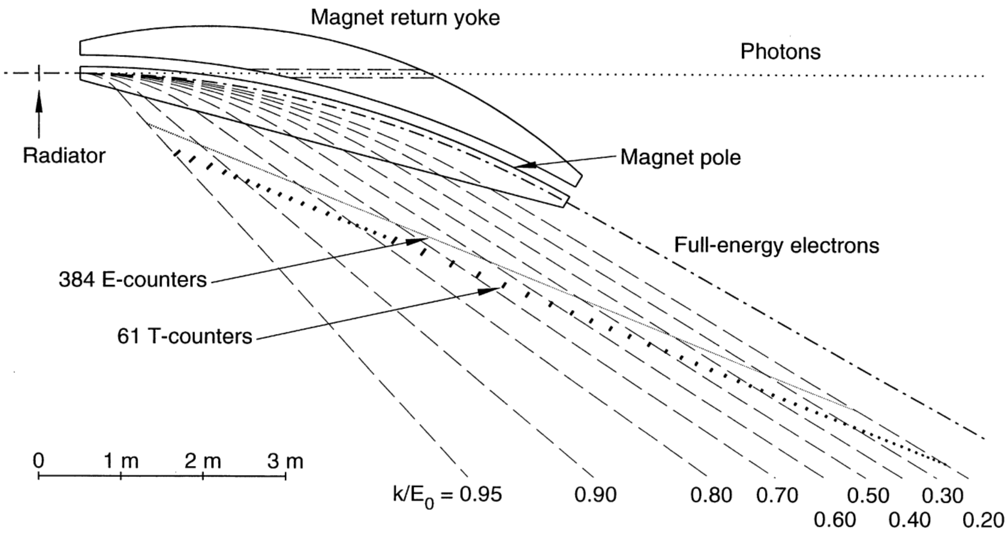

Figure 2.4: Schematic diagram of the photon tagger spectrometer. The electron beam enters from the left and goes through a radiator, where a few electrons generate photons via *bremsstrahlung* radiation. The black-dashed lines represent the trajectories taken by the recoil electrons at different fractional energies, guided by the dipole magnet to a set of scintillator counter planes, the E- and the T-counters. These are properly depicted in the diagram, in accordance to their geometry, and with the correct segmentation. Image reprinted from [45], with permission from Elsevier.

by a magnetic tagger spectrometer can furnish a measurement of the photon energy E_γ. In order to determine said energy, a scintillator plane (known as an E-counter) was used to determine the momentum of the recoiling electrons. Therefore, since the radius of curvature of the electron's trajectory due to a magnetic field is proportional to the electron's momentum, knowing the electron's exact position along a plane provides sufficient information to determine its energy and momentum.

The E-counter consisted of 384 plastic scintillators, each 20 cm long, 4 mm thick, and $6-18$ mm wide. The scintillators were arranged in an overlapping manner, resulting in 767 distinct channels to determine a scattered electron's position, energy and momentum. Thus, the spectrometer could tag photons ranging from $20\%-95\%$ of the incident electron beam energy, with a resolution of 0.1%. The second scintillator plane (the T-counter) was used to obtain accurate timing measurements of recoiling electrons and the associated photon time. Positioned parallel to and 20 cm behind of the E-counter, it was composed of 61 overlapping scintillators, each 2 cm thick with varying length from 20 cm at high electron momentum to 9 cm at low electron momentum, with 121 distinct channels. The added thickness to the scintillators gave a timing resolution of ~ 110 ps.

2.3 The $g12$ Cryotarget

Target cells of a variety of shapes and sizes have been employed under different experiments using the CLAS detector. Built at the Jefferson Lab, and originally commissioned for a different CLAS run experiment ($g11a$), the cylindrical $g12$ liquid Hydrogen (lH_2) target cell had a length of 40 cm with a radius of 2 cm (see Figure 2.5). On the other hand the incoming photon beam had a radius of approximately 1.5 cm as it excited the target. The target cell's walls and substructure were composed of aluminum, while the target cell's window was composed of Kapton. The particular choice of Kapton was due to its advantageous performance under high levels of radiation and temperature. For the $g12$ experiment the target cell was moved 90 cm upstream of the CLAS detector center in order to achieve a geometric acceptance starting at roughly 6° from the beamline, in order to avoid any loss of high momentum tracks in the forward direction (which is where the beam passed through), thus increasing the forward geometric acceptance of the detector. Once every hour, the target's pressure and temperature were measured to calculate the *density* of lH_2 in the cell. This measurement is needed for the extraction of *cross section* measurements.

Figure 2.5: Diagram of the $g12$ cryotarget, filled with liquid Hydrogen. Image source: [14].

2.4 The CLAS Detector

The CEBAF Large Acceptance Spectrometer (CLAS) was the primary physics detector housed within Hall B of JLab. At roughly 10 m in diameter, the main purpose of CLAS was to detect charged and multi-charged final particle states produced by the interaction of a circularly-polarized photon beam with a cryotarget. Its design was based on a non-homogeneous toroidal magnetic field, generated by a set of six superconducting coils arranged around the beamline, which created

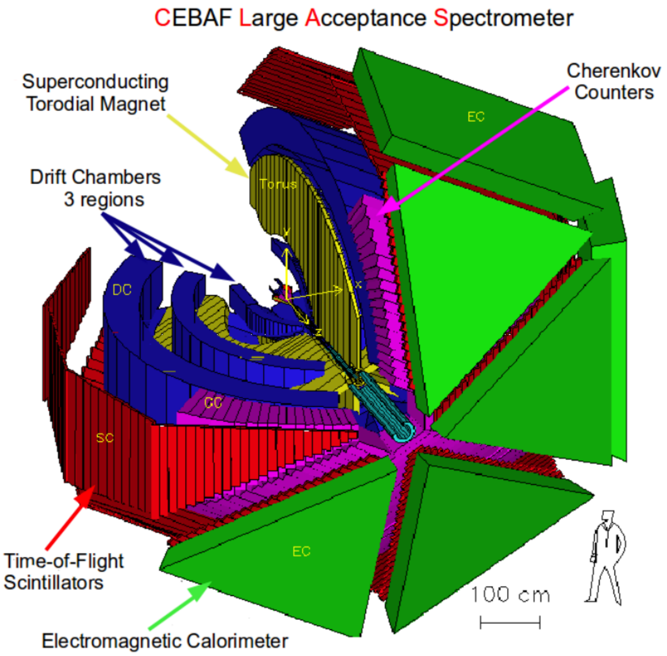

Figure 2.6: A 3D-schematic cutaway of CLAS showing its major components. Image reprinted from [51], with permission from Elsevier. Image adapted from [33]. Licensed under CC BY-NC-ND 2.0.

a field pointing primarily along the ϕ-direction. The purpose of this field was to bend any negatively charged particles towards the beamline and any positively charged particles away from the beamline.

The CLAS detector was structured in multi-layered arrangements of different particle detectors symmetrically about the beam axis. Consequently, the CLAS detection system had a six-fold symmetry about the beam axis (see Figure 2.6), and an almost 4π solid angle coverage (spoiled only by the forward beam hole, beamline, support structure for the magnet, etc.). Therefore, the CLAS detector was azimuthally divided into six independent ϕ segments called *sectors*; each consisted of the following detectors: a *Start Counter* (ST), used to detect charged particles traveling from the target region, three layers of *Drift Chambers* (DCs), used to determine the trajectories of charged particles, a gas *Cherenkov counter* (CC), for electron identification, a series of *Scintillation Counters*, to measure the *Time-of-Flight* (TOF), and an *Electromagnetic Calorimeter* (EC), to detect showering particles (photons and electrons) and neutrons. Due to the fact that neither the CCs nor the ECs were employed for the $g12$ experiment (these are only used in experiments with electron beams), these subsystems shall *not* be discussed with any detail in any further Sections.

2.4.1 The Start Counter (ST)

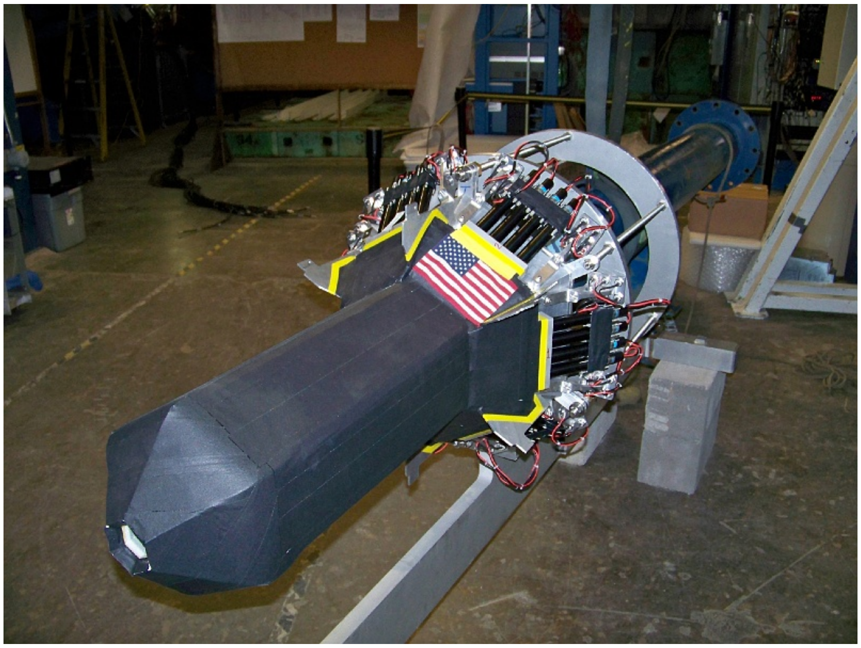

Figure 2.7: Picture of the Start Counter (ST), outside of the CLAS detector, displaying the tapered "nose" formed by the scintillator paddles on the forward end, attached to an acrylic guide and a photomultiplier tube (PMT) on the back end. Image source: [31].

The first detector component that a charged particle encountered in CLAS, after traveling through the target, was the multi-segmented Start Counter (ST) directly surrounding the target cell. This CLAS detector component provided initial raw timing information on the charged particles as they proceeded from the target; the timing resolution of the ST was ~ 350 ps. As such, the ST provided accurate measurements of the start and end times of all trigger events recorded by CLAS.

Similar to the CLAS detector, the ST was divided into six segments, each consisting of four 502 mm long scintillator paddles coupled to an acrylic light guide. The upstream ends of the SC were attached to Photomultiplier Tubes (PMTs), while the downstream ends were inwardly bent, converging into a hexagonal cone (known as the "nose") and granting coverage for smaller angles of θ. Hence, incoming charged particles traveling from the target and traversing the scintillator paddle produced light within the scintillator, which then traveled to the light guide attached to the PMT. Once at the PMT, the photon signal was collected, then converted and amplified into an electric signal stored for future analysis. See Figure 2.7 for a picture of the ST outside of CLAS.

2.4.2 Torus Magnet

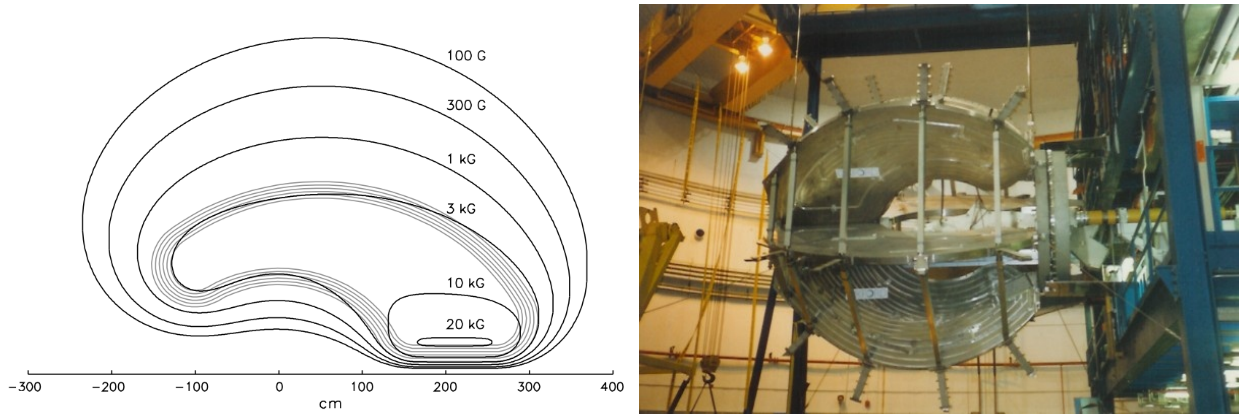

Figure 2.8: (Left): Strength contours of the constant absolute magnetic field generated by the CLAS torus magnet in the midplane between the two coils. For the $g12$ run the magnets were operated at half their capacity current (1930 A). Image reprinted from [43], with permission from Elsevier. (Right): The CLAS torus magnet during its installation in Hall B. Image source: [30].

At the heart of the CLAS detector lied a superconducting toroidal magnet. The magnetic field employed for bending charged particles was generated via the use of six kidney-shaped superconducting coils arranged in a toroidal geometry about the beamline axis and separated by 60° angles in the azimuthal direction; see Figure 2.8 (Right). This resulted in a magnetic field whose main component was along the ϕ-direction; see Figure 2.8 (Left). This field lead to charged particles traveling along non-linear paths through the drift-chambers (DC). This tracking system (Sub-section 2.4.3) was used to determine the trajectory followed by each charged particle. Consequently, the force supplied by this field acting on the charged particles left their azimuthal angles unchanged, while bending the particles towards or away from the beamline. For a positive (negative) current, the magnetic field bent negatively-charged particles towards (away from) the beamline.

Having knowledge on the strength and direction of the magnetic field, the particle's trajectory was then used to determine its momentum. However the magnetic field generated by the toroidal magnet was not completely uniform, as it had significant deviations from a pure ϕ-field close to the coils. This effect on the particle trajectories was minimized by the inner circular shape of the coil.

At approximately 5 m in diameter and 5 m in length, each of the six superconducting coils of the torus magnet had four layers of 54 turns of aluminum-stabilized niobium-titanium NbTi/Cu conductors. The coils were cooled down to a temperature of 4.5 K by forcing super-critical Helium through cooling tubes placed at the edge of the windings. The torus magnet was capable of generating a maximum current of 3860 A, resulting in a maximum magnetic field strength of 3.5 T. At this current the magnetic field reached 2.5 T in the forward direction, dropping down to 0.6 T in the perpendicular direction (with a scattering angle of 90°).

2.4.3 Drift Chambers (DCs)

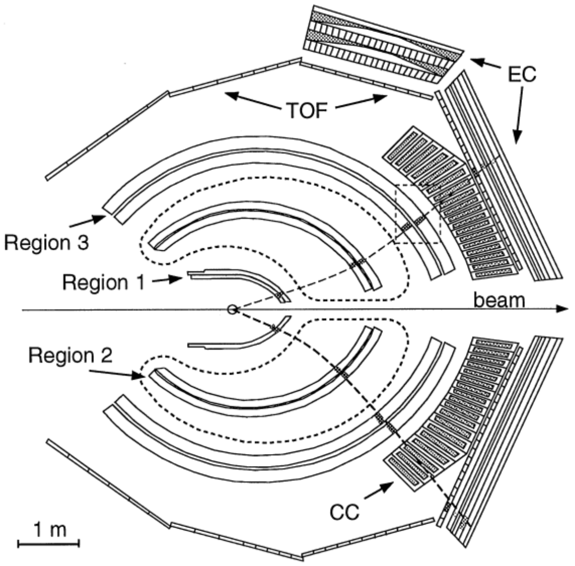

Figure 2.9: Cross sectional diagram of the CLAS detector, displaying the relative positions of its subsystems, and the DCs regions. The kidney-shaped dashed lines denote a projection of the torus coils along the sector mid-plane. Also shown are the curved trajectories of two charged particles traversing the DC along opposite sectors. Image reprinted from [48], with permission from Elsevier.

The task of tracking charged particles as they traveled through the magnetic field generated by the toroidal magnet (sub-Section 2.4.2) was carried out by drift chambers (DCs), a CLAS subdetector system. The DCs determined the momenta of the charged particles from their curved trajectories. The geometry of the torus magnet was such that it divided the DCs into six independent tracking areas (known as sectors), each of which were further divided into three distinct regions located at different radial positions from the target, based on the magnetic field strength.

The Region 1 (R1) chambers surrounded the target in an area of low magnetic field, and were used to determine the initial trajectory of the incoming charged particles. The Region 2 (R2) chambers were located between the magnetic coils, near the point of maximum track sagitta, and

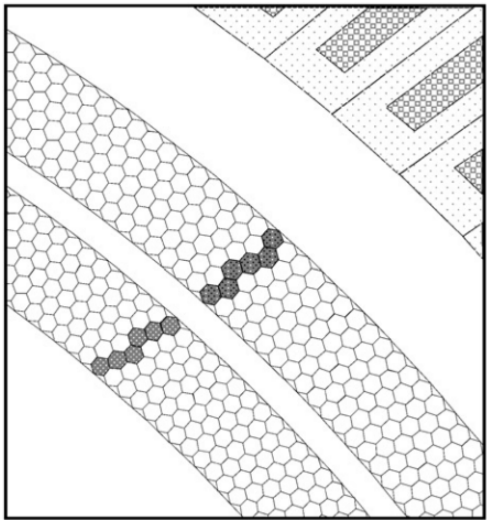

Figure 2.10: A schematic showing the superlayers of Region 3 of the DCs. The hexagonal perimeters are for illustrative purposes. The trajectory of a charged particle is shown as recorded by the shaded region of the drift cells that have fired. Image reprinted from [48], with permission from Elsevier.

as such occupied the region where the magnetic field was the strongest, and were used to determine a particle's track curvature, and hence its momentum. Lastly the Region 3 (R3) chambers were outside of the magnetic torus coils, where the magnetic field was again weak, and were used to determine the final position of the particle's trajectory, before reaching the time-of-flight (TOF) system. The DC system arrangement provided an angular coverage of $8^\circ - 142^\circ$ in the polar angle, and an 80% coverage of the azimuthal angle ϕ. A cross sectional diagram showing the arrangements of these Regions is shown by Figure 2.9. The wire layers in each of the DC regions were divided into two *superlayers*, with each superlayer composed of six wire layers (see Figure 2.10).

Within each DC, all drift cells had a 20 μm gold-plated tungsten sense wire located at the center of a quasi-hexagonal arrangement of six 140 μm gold-plated aluminum alloy field wires. The sense wires had an intrinsically positive potential, whereas the field wires were kept at a negative high voltage; the number of sense wires in the DC system was 35,418. The DC chambers occupied a considerable portion of the CLAS volume and were filled with a gas mixture of 90% Argon and 10% carbon-dioxide (CO_2), due to its ionization properties and non-flammability. This gas mixture ionized charged particles via electromagnetic interactions or collisions. The ensuing ionized particles were then collected by wires kept at a potential difference, and the flow of current in those wires relayed the particle's position and trajectory, from which its momentum was determined.

2.4.4 Time-of-Flight (TOF) Scintillators

The Time-of-Flight (TOF) detectors were an essential CLAS subsystem for particle identification. Adhering to CLAS geometry, the TOF had six identical and independent panel sections, one per CLAS sector, located roughly 4 m away from the cryotarget, each containing 57 scintillator paddle bars made of Bicron BC-408, with varying lengths and widths (see Figure 2.11). Attached at the end of each scintillator was a photomultiplier tube (PMT). To provide a large signal for traversing minimum-ionizing particles, each scintillator had a uniform thickness of 5.08 cm.

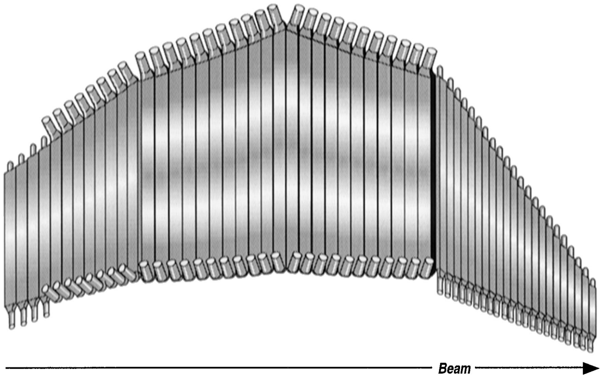

Figure 2.11: Diagram of the (TOF) scintillator counters from one CLAS sector. Each scintillator was positioned perpendicularly to the average particle trajectory. Image reprinted from [47], with permission from Elsevier.

The purpose of the TOF subsystem was to measure the time at which charged particles interacted with the TOF scintillators after traveling through the DCs. This measured time, used in conjunction with the starting hadronic interaction time of the event at the target (measured by the SC), provided the "time-of-flight" of charged particle tracks as they traversed the system's magnetic field. Moreover, with the trajectory and track length measurements provided by the DCs (along with the particle's momentum p) and the TOF, the velocity β of the particles was established. Thus, determining the particle's mass and identity (proton, K, π, etc.) was achieved via,

$$m = \frac{p\sqrt{1-\beta^2}}{\beta}. \tag{2.2}$$

The photon signals created by the TOF scintillators, generated by particle interactions and recorded by the PMTs, were subsequently transformed and amplified into an electric signal. The timing resolution of the scintillators was $80 - 160$ ps and depended on the length of the paddle bar; the longer paddle bars provided a worse resolution.

CHAPTER 3

EVENT SELECTION & DATA CALIBRATION

The data set recorded by the $g12$ experiment consisted of over 126 TB of raw data, containing a set of 26 billion recorded events. However, before any kind of analysis began, the raw data underwent a process of *reconstruction* (colloquially known as *cooking*), meaning that all raw electrical signals and information arriving from the various detector subsystems of the experiment were transformed into a form suitable for physical analysis, such as: physical 4-momentum vectors for all charged tracks recorded for every event, particle IDs, positions, energies and angles. During the cooking process of the raw data, each of the CLAS subsystems underwent extensive individual calibration.

For a data set of this size, the $\gamma p \to K^0\Sigma^+$ reaction made but a small portion of the data, due to its low cross-section. As such, the recorded data was dominated by other far more likely reactions. Therefore, a careful extraction was performed to keep the number of background events low, while enhancing those events of interest to the analysis.

The first step in the cooking process consisted of choosing events that fit a desired description (Section 3.1). Missing particles were reconstructed via the use of the *missing mass technique*, based on energy-momentum conservation (Section 3.2). Afterwards, a series of corrections were performed to account for any loss of energy and momentum that a particle might have experienced as it interacted with any detector subsystems. This was followed by a *kinematic fit*, which enhanced the kinematics of the particles using a set of constraints to their energies and momenta via conservation of energy and momentum (Section 3.3). Cooking of the data culminated with a series of cuts aimed at removing background underneath signal peaks, yielding clean event samples (Section 3.4).

The cooking of the $g12$ data set used for this analysis was performed by Dr. Zulkaida Akbar, and it is documented in a CLAS-approved $g12$ analysis note [55]. The purpose of this chapter is to briefly and succinctly highlight the cooking phase of the data before our data analysis efforts, described in Chapters 4 and 5, began. A more throughout and complete treatment of the cooking process, cuts and corrections applied for the data reconstruction can be found in Reference [3].

3.1 The CLAS-g12 Data Set

Equipped with an array of unique experimental devices, the $g12$ experiment was housed within Hall B at JLab, and employed a circularly-polarized photon beam in conjunction with an unpolarized liquid Hydrogen (lH_2) target. The incident photon beam energy provided for the experiment covered a range of $1.1 < E_\gamma < 5.4$ GeV. The resulting data was divided into a set of 10 distinct run groups (CLAS Collaboration Institutions), each in accordance to a particular trigger condition. The initial information contained within the $g12$ raw data, obtained from the CLAS subsystems, was composed of QDC (Charge to Digital Convertor) and TDC (Time to Digital Converter) channel IDs and values. This information underwent several layers of careful reconstruction, converting the raw data into useful information for our analysis. For a summary of these cuts see Section 3.4.

For the purpose of this analysis (and other analyses at FSU) only Period 2 data was used, since the addition of Period 1 (suffering from low statistics) would not have improved the uncertainties of the ensuing results. Periods $3-8$ used a lepton trigger or an EC (Electromagnetic Calorimeter) photon trigger, which were avoided for this analysis. Triggering conditions for this data set required either three charged tracks with no restriction on the beam energy, or only two tracks with the restriction of having at least a single photon with an energy of $E_\gamma > 3.6$ GeV. Table 3.1 displays the set of trigger configurations used for the $g12$ experiment.

Table 3.1: The set of trigger configurations employed for the $g12$ experiment. Only the events falling within Period 2 were employed for the purpose of FSU analyses. Table compiled from the $g12$ wiki and Reference [54]. Courtesy of Dr. Zulkaida Akbar (University of Virginia).

Period	Runs	Trigger Configuration
1	56519 and earlier	not prescaled, trigger change at 4.4 GeV
2	56520 - 56594, 56608 - 56646	not prescaled, trigger change at 3.6 GeV
3	56601 - 56604, 56648 - 56660	prescaled
4	56665 - 56667	prescaled
5	56605, 56607, 56647	prescaled
6	56668 - 56670	prescaled
7	56897 and later	prescaled
8	57094 and later	prescaled
9	56585, 56619, 56637	single-sector, not prescaled
10	56663 and later	single-sector, not prescaled

3.2 Reaction Channel and Event Selection

The principal reaction for the purposes of this analysis was $\gamma p \to p\pi^+\pi^-(\pi^0)$, where the missing mass of the π^0 was found through the use of the *missing-mass technique* (relativistic kinematics). To that end, the Lorentz four-vector of the incoming photon beam and the proton target were employed. The missing four-momentum of the π^0 was thus determined via the use of the measured three-momenta and energies of the observed particles involved in the reaction, resulting in,

$$x^\mu = k^\mu + P^\mu - \sum_{i=1}^{2,3} p_i^\mu, \tag{3.1}$$

where k^μ denotes the four-momenta of the incoming photon beam, P^μ is the four-momenta of the proton target, while the sum over p_i^μ represents the four-momenta of the two or three final-state particles detected in the reaction. Additionally, the missing mass m_X can be determined via,

$$m_X^2 = x^\mu x_\mu. \tag{3.2}$$

The resulting four-momentum vector x^μ from expression (3.1) served to complete the set of four-momentum vectors for all particles for the reaction under study. For the cooking process, any events whose particle identification numbers (PIDs) failed to meet the constraint of having one proton, one π^+ and a π^- as part of their final-state, were altogether removed from the analysis.

In order to calculate the masses of any detected particles, two quantities were necessary: the particle's momentum p, along with their velocity expressed as a fraction of the speed of light (β). This velocity β was reconstructed by using the particle's time of flight $t_f = t_{TOF} - t_{ST}$, along with its track (or path) length $d_f = \ell_{TOF} - \ell_{ST}$, from the vertex position up to the TOF scintillator paddles where the particle had interacted. This yielded the following expression,

$$\beta = \frac{d_f}{t_f} = \frac{(\ell_{TOF} - \ell_{ST})}{(t_{TOF} - t_{ST})}, \tag{3.3}$$

where the measured velocity β of a detected final-state particle had an uncertainty of up to 5%, and was determined via a combination of the Time-of-Flight (TOF) subsystem (which measured the time at which particles interacted with the TOF scintillators), the Start Counter (ST) detector (which furnished the starting time of interaction of an event at the target) and the Drift Chambers (DCs) subsystem (which provided a particle's trajectory as it traveled through CLAS, along with its momentum p, with an uncertainty of $< 1\%$); more information about the detector subsystems can be found in Section 2.4. Consequently, the detected particle's rest mass was computed via use of its momentum p as follows,

$$E = \gamma m_{\text{particle } X} = \frac{p}{\beta} \quad \Rightarrow \quad m^2_{\text{particle } X} = \frac{p^2(1-\beta^2)}{\beta^2}, \tag{3.4}$$

where γ is a Lorentz factor (where we made use of *natural units*, i.e. $c = 1$); this result was previously stated by equation (2.2). The resulting invariant particle mass was then compared to those of a set of known particles. If the masses were a match (within a certain resolution), then the associated PID (particle ID) of said mass could be bestowed upon the final-state particle.

For the purposes of this analysis, all physical properties of any final-state particles (such as their four-vectors, vertex information, etc.) were obtained from the PART CLAS data bank, a repository containing information about the detected final-state particles of interest. Photon and final-state particle selection saw further improvement via the implementation of a set of cuts and corrections applied to the data, briefly detailed in Section 3.4. Furthermore, kinematic fitting was used (Section 3.3) as a means of fine-tuning initial and final-state momenta by imposing energy-momentum conservation constraints. Lastly, in order to separate signal events from background events, an event-based method, known as the $Q-$factor method, was employed; see Section 3.6.

3.3 Kinematic Fitting

Any set of measured four-vectors from the detected final particle states, carried out in CLAS, had an associated inherent resolution. This resolution resulted from a series of convolutions from various errors and uncertainty procedures carried out during the reconstruction process. Once a given track had been properly associated with a particle, then every measured component of its *raw* Lorentz 4-vector (the magnitude of the momentum p, and the two angles used to describe the detector's geometry, λ and ϕ), along with the initial photon beam energy, were modified until each event satisfied energy-momentum conservation, with the energy and momentum of each particle matching their real masses (as stated in the PDG). Known as *kinematic fitting*, this process uses the *least squares method* to determine the value of a series of unknown quantities from a model by minimizing the sum of the squares of its residuals, via the application of *Lagrange multipliers.*

Accurately determining the *covariance matrix* lead to a correct estimation on the fit uncertainties. Kinematically fitted events had a set of quantities used to inspect the quality of the fits: a *pull value* for every measured quantity, and a χ^2 value (turned into a confidence level).

3.3.1 Confidence Level and Pull Distributions

The main measure of the *goodness of fit* (the agreement between the hypothesis fit and the measured data) employed for the least squares method is known as the *confidence level* (CL),

$$CL = \int_{\chi^2}^{\infty} f(z; n) dz, \tag{3.5}$$

where $f(z; n)$ denotes the χ^2 probability density function for n degrees of freedom. The CL value is effectively a measure of the probability distribution that a χ^2 from a theoretical distribution is greater than the χ^2 originating from the fit. Ideally, a data set for which all events satisfy the fit hypothesis with normally distributed errors would result in a flat confidence level distribution on the $(0, 1]$ range. However, the real data contained background events (events which did not satisfy the enforced energy-momentum conservation constraints) with a confidence level distribution centered near zero. A cut on events with a low confidence level provides an effective way of eliminating the majority of background events, without jeopardizing a fair amount of well-behaved data.

In order to properly apply the confidence level cut to the background, it is necessary to have a firm grasp on each of the fit quantity's errors. To examine the quality of the error estimation, a *pull distribution* (also known as a *stretch function*), which quantifies the extent to which the kinematic fitter needs to alter a measured parameter so as to impose energy-momentum conservation on an event, becomes a necessary tool. The *pull value* of the i^{th} fit parameter was defined as,

$$z_i \equiv \frac{\epsilon_i}{\sigma(\epsilon_i)}, \tag{3.6}$$

where $\epsilon_i = \eta_i - y_i$ represents the residual (η_i is the fitted value, while y_i is the measured value), with a standard deviation of $\sigma(\epsilon_i)$. The pull values z_i's should be normally distribution about zero with a standard deviation of $\sigma = 1$. Alternatively, the i^{th} distribution can be rewritten as,

$$z_i \equiv \frac{\eta_i - y_i}{\sqrt{\sigma^2(\eta_i) - \sigma^2(y_i)}}. \tag{3.7}$$

3.4 A Summary of All Applied Cuts & Kinematic Corrections

This Section contains a brief detailed summary on all cuts and kinematic corrections applied to the raw data recorded by the $g12$ experiment. A more throughout treatment of the ensuing cuts and corrections for this analysis can be found in Reference [3].

3.4.1 Fiducial Volume Cuts

Geometrical fiducial cuts, in accordance to a *nominal scenario* (outlined in Reference [54]), were applied to remove events from the analysis which were found in regions of the detector subsystems where the acceptance was either not well understood or modeled (or both). Hence, all regions for which the detector acceptance was well and reliably modeled by the simulations were designated as the upper and lower limits of the azimuthal difference between the center of a particular sector and a particle track. Consequently due to the inherent hyperbolic geometry of the CLAS detector, coupled with the presence of a toroidal magnetic field, the fiducial boundaries on the upper and lower ϕ were described as functions dependent on the momentum p, charge and polar angle θ of each individual particle track.

3.4.2 Particle ID and Timing Cuts

In order to find the correct initial photon involved in an event, a *coincidence time* Δt_{TBID} was defined per each photon as the difference between the Tagger and Start Counter times at an interaction point, $t_{\mathrm{event}} - t_{\gamma}$. As such, a timing cut of $|\Delta t_{\mathrm{TBID}}| < 1$ ns was applied in the analysis. Furthermore, in order to correctly identify the final-state particles, proton (p), π^+ and π^-, information on the calculated and measured values of β for each particle were employed. Using a CLAS-measured particle momentum from the TBID bank, a theoretical velocity for the particle (i.e. β_{c}) was calculated and compared to the CLAS-measured empirical β_{m} value. Particle identification then proceeded by selecting the β_c value with greatest proximity to the measured value of β_{m}. As such, the difference in β for theoretical/empirical measurements $\Delta\beta$ was given by,

$$\Delta\beta = \beta_{\mathrm{c}} - \beta_{\mathrm{m}} = \sqrt{\frac{p^2}{m^2 + p^2}} - \beta_{\mathrm{m}}. \tag{3.8}$$

The ensuing cut values applied to the data were determined by fitting a Gaussian around the main peak distribution $\Delta\beta = 0$, resulting in a $\Delta\beta = |\beta_{\mathrm{c}} - \beta_{\mathrm{m}}| \leq 3\sigma$ particle ID cut.

3.4.3 Vertex Cut

The liquid Hydrogen target utilized for the $g12$ experiment was 40 cm long, with a radius of 2 cm (see Figure 2.5). For the purpose of the $g12$ experiment the target cell was moved away from the center of the CLAS detector and placed 90 cm upstream from the detector in an effort to achieve a higher angular resolution for heavy-meson photoproduction in the forward direction. Henceforth, due to the geometry of the target's placement, a z-vertex cut with a range given by $-110.0 < z < -70.0$ cm was applied. Figure 3.1 displays the entirety of the z-vertex distribution.

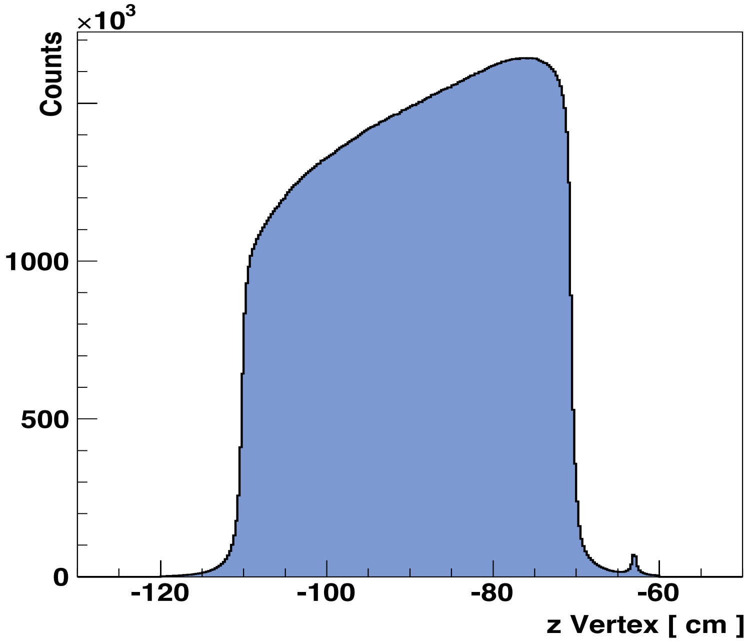

Figure 3.1: The z-vertex distribution (this is the axis along the beamline direction) of all reconstructed particles used in FSU analyses, delineating the geometry of the cylindrical lH_2 $g12$-cryotarget. The slight kink centered around $z = -63$ cm stems from the vacuum chamber's exit region. Image source: [3]. Courtesy of Dr. Zulkaida Akbar (University of Virginia).

3.4.4 Confidence Level (CL) Cut

In order to fix the events of interest to a set of imposed constraints by the kinematic fit, a confidence level cut of CL > 0.001 was applied for the $\gamma p \to p\pi^+\pi^-(\pi^0)$ reaction. Cutting events with a low CL eliminates most background events while sacrificing only a small set of good data.

3.4.5 Tagger-Sag Corrections

Based on observations from previous experiments, a physical sagging of the structure supporting the E-counter scintillator bars could in fact be ascribed to the effect of gravitational forces [53]. Consequently, this time-dependent sagging led to a minuscule shift of the energy of the scattered electrons [19]. This was subsequently corrected and accounted for in the offline reconstruction code.

3.4.6 Energy-Loss (ELoss) Corrections

The 4-momentum vectors of the charged particles of interest, namely the proton (p), π^+ and π^-, were individually corrected for any energy loss they suffered while traveling through different materials of the CLAS detector subsystems. When charged particles travel through matter, with the exception of electrons, they lose energy due to a series of processes, including inelastic scattering, atomic excitations or ionization as they interact with the target material (lH_2) and its walls, beam pipe, the Start Counter, and the air gap situated between the ST and the Region 1 Drift Chambers.

Consequently, the ensuing reconstructed momentum from the drift chambers was smaller than that of a particle at the production vertex. To account for this discrepancy, the 4-vectors of all final-state particles were corrected, event-by-event, via the implementation of the "ELoss" software package, developed for CLAS analyses [36], which determined the lost momentum of each particle after interacting with different detector materials. The individual particle 4-vectors were corrected by multiplying an ELoss correction factor η_{particle} (this modified a particle's momentum by a few MeV) for each particle to the magnitude of their measured raw CLAS momentum $P_{\text{particle (CLAS)}}$,

$$P_{\text{particle (ELoss)}} = \eta_{\text{particle}} \cdot P_{\text{particle (CLAS)}}, \tag{3.9}$$

where $P_{x(\text{ELoss})}$ represents the momentum of a particle x (either a proton p, π^+ or π^-) after the application of energy-loss corrections.

3.4.7 Momentum Corrections

The set of reconstructed momenta required small corrections of up to a few MeV for the final-state particles' momenta on account of two reasons: first, due to the fact that the torus magnetic field map was based on several approximations, whose calculations for a single sector worked under the assumption that all coils and material within the field were symmetric with respect to the six-fold geometry of the CLAS detector, while neglecting to take into account any of the field's variations. Secondly, due to any present ambiguities and inefficiencies in the drift chamber alignments, this resulted in small momentum shifts. Therefore each of the measured track momenta, as measured by the DCs, displayed a systematic shift within each individual sector, with an azimuthal dependence of ϕ on one of the tracks. In the reconstruction analysis, CLAS-approved correction procedures were implemented, as defined in Reference [54].

3.5 Circularly-Polarized Photon Beam

The electron beam employed for the $g12$ experiment was longitudinally polarized. This beam produced circularly-polarized photons via the bremsstrahlung process of longitudinally-polarized electrons emanating from an amorphous radiator (Section 2.2). The energy-dependent degree of circular polarization $P_{\odot}(E_{\gamma})$ of the photons was given by the Maximon-Olson formula [35],

$$P_{\odot}(E_{\gamma}) = P_{\text{elec}} \cdot \frac{4x - x^2}{4 - 4x + 3x^2}, \tag{3.10}$$

where $x = E_{\gamma}/E_{\text{elec}}$ is the fraction of photon energy E_{γ} to initial electron beam energy E_{elec}, while P_{elec} denotes the polarization of the electron beam. For the purposes of the $g12$ experiment, the electron beam (CEBAF) energy used for all of the runs in the analysis was $E_{\text{elec}} = 5.715$ GeV.

The electron beam polarization was regularly measured via the use of the Møller polarimeter, a device which measured the electron polarization by making use of the underlying helicity-dependent nature of Møller scattering [46]. The results stemming from the Møller measurements of the electron beam polarization P_{elec} are summarized in Table 3.2. For the duration of the $g12$ experiment, Hall B did not have beam priority, and consequently the beam polarization was delivered as a byproduct from the requirements of the other Halls. In spite of polarization fluctuations, most of the $g12$ runs had a beam polarization close to 70%, and a total uncertainty of roughly 5%.

Table 3.2: Møller measurements of the electron beam polarization P_{elec} for the $g12$ experiment. Only the Møller measurements within the run range 56476 − 56643 were used in the analysis. Table compiled in Reference [3]. Courtesy of Dr. Zulkaida Akbar (University of Virginia).

Run Range	Electron Beam Polarization, P_{elec} (Møller Readout)
56355 - 56475	$(81.221 \pm 1.48)\%$
56476 - 56643	$(67.166 \pm 1.21)\%$
56644 - 56732	$(59.294 \pm 1.47)\%$
56733 - 56743	$(62.071 \pm 1.46)\%$
56744 - 56849	$(62.780 \pm 1.25)\%$
56850 - 56929	$(46.490 \pm 1.47)\%$
56930 - 57028	$(45.450 \pm 1.45)\%$
57029 - 57177	$(68.741 \pm 1.38)\%$
57178 - 57249	$(70.504 \pm 1.46)\%$
57250 - 57282	$(75.691 \pm 1.46)\%$
57283 - 57316	$(68.535 \pm 1.44)\%$

3.6 Signal-Background Separation: The $Q-$Factor Method

The Quality Factor ($Q-$*value*) method is an event-based technique for which a set of coordinates describing the multi-dimensional phase space of a reaction are categorized in accordance to two distinct types of classes: *reference* (ξ_r) and *non-reference* (ξ) coordinates [66]. For the reference coordinates (this normally being the mass), the signal and background distributions must be known *a priori* in order to cleanly separate the background from the desired event signal. On the other hand, in the case of the non-reference coordinates, this information is unnecessary.

For each event, one seeks to find the set of N_c nearest neighbors within the phase space of the non-reference coordinates. To that end, an appropriate *metric* must be defined for the space spanned by the non-reference coordinates ξ (excluding ξ_r). According to this metric, the minimum distance between any set of two events d_{ij} is given by,

$$d_{ij}^2 = \sum_{k \neq r} \left[\frac{\xi_k^i - \xi_k^j}{\sigma_k} \right]^2, \tag{3.11}$$

where σ_k represents the range of the k^{th} variable within the appropriate phase-space distribution, and the sum is performed over all coordinates with the exception of the set ξ_r. This metric is known as the *normalized Euclidean distance* [66]. For each event then, the closest distance to all other events may be computed while retaining the N_c nearest neighbor events in accordance to expression (3.11). The ensuing mass distribution of the N_c events (including the candidate event) within the reference coordinate was fitted via the use of the total function defined by,

$$f(\xi) = N \cdot [f_s \cdot S(\xi) + (1 - f_s) \cdot B(\xi)], \tag{3.12}$$

where $S(\xi)$ and $B(\xi)$ represent the signal and background probability density functions, respectively, N denotes a normalization constant, and f_s describes a signal fraction with a value constrained within the range $[0.0, 1.0]$. The $Q-$factor for each event was then given by the following,

$$Q = \frac{s(\xi)}{s(\xi) + b(\xi)}, \tag{3.13}$$

where $s(\xi) = f_s \cdot S(\xi)$ and $b(\xi) = (1 - f_s) \cdot B(\xi)$. The $Q-$factor, which has a range constrained within the bound $[0.0, 1.0]$, assigns a probability to each event that is part of the signal, and can be used as an event-weight to determine the contribution of the signal to a given physical distribution.

3.6.1 The $Q-$Factor Method for the Reaction of Interest $\gamma p \to K_S^0\Sigma^+$, Using the g12 Data Sets

For the reconstruction of the final-state $K_S^0\Sigma^+$, the strange K_S^0 state was reconstructed from its decay to the $\pi^+\pi^-$ system, while the remaining π^0 stemmed from the baryon weak decay. Since the $K_S^0 \to \pi^+\pi^-$ and $\Sigma^+ \to p\pi^0$ systems are strongly correlated (via their associated strangeness production), one can use either invariant mass of the $\pi^+\pi^-$ or $p\pi^0$ system as a reference quantity. Table 3.3 displays the non-reference variables applied for the background subtraction of the reaction at hand. For a more throughout discussion on what follows, see Reference [3].

Table 3.3: Set of non-reference coordinates ($\vec{\xi_i}$) used for background subtraction in the reaction $\gamma p \to K^0\Sigma^+$. The quantities in parenthesis denote the set of non-reference coordinates employed for the $Q-$values, and based on the $(p\pi^0)$ invariant mass. Table compiled in Reference [3]. Courtesy of Dr. Zulkaida Akbar (University of Virginia).

$\vec{\xi_i}$	Non-Reference Coordinate	Maximum Range Δ_i
$\vec{\xi_0}$	Incident-photon energy E_γ	50 MeV
$\vec{\xi_1}$ & $\vec{\xi_2}$	$\cos\theta_{\pi^+}$ $(\cos\theta_p)$ & ϕ_{π^+} (ϕ_{π^0}) in the $\pi^+\pi^-$ $(p\pi^0)$ rest-frame	2 & 2π
$\vec{\xi_3}$	$\cos\Theta^{K_S}_{\text{c.m.}}$ in the center-of-mass frame	2
$\vec{\xi_4}$	$\phi^{K_S}_{\text{lab}}$	2π
$\vec{\xi_5}$	cos(opening angle $\angle\ (p,\pi^0)$)	2

Given the fact that the cross section of the $\gamma p \to K^0\Sigma^+$ reaction is relatively small, the observed statistics were low. Consequently, the invariant mass $\pi^+\pi^-$ was engulfed by background within the K_S^0 mass region (Figure 3.2, Top Left). Hence, a set of two different mass cuts were considered before applying the background subtraction $Q-$factor method (see Figure 3.2):

1. Conservation of strangeness is a feature of strong and electromagnetic interactions, which is the reason why a K_S^0 meson is produced accompanied by a Σ^+ baryon (within our analysis). Since the lifetime of the Σ^+ ($\tau = (0.8018 \pm 0.0026) \times 10^{-10}$ s) is considerably long (as it decays weakly), a narrow cut of 20 MeV was applied around the Σ^+ mass of 1189.37 MeV [59].

2. The dominant reaction which contributes to the $p\pi^+\pi^-\pi^0$ final-state is the ω production. This can be seen in the Bottom-Left histogram shown by Figure 3.2. The ω band is clearly prominent, displaying a maximum intensity within the neighborhood of the K_S^0 in its projection onto the $\pi^+\pi^-$ plane. Therefore, a mass cut was applied in order to remove any contributions stemming from ω production, namely: $m_{\pi^+\pi^-\pi^0} < 752$ MeV and $m_{\pi^+\pi^-\pi^0} > 812$ MeV.

Lastly, to subtract the background for the $K^0\Sigma^+$ final-state, the $g12$ data was divided into 50 MeV-wide and 100 MeV-wide incident photon energy bins for cross-sectional and induced polarization measurements, respectively. A set of 1000 nearest-neighbor events were chosen for each signal candidate in the phase space spanned by the non-reference coordinates. Since the Σ^+ recoil polarization was obtained via the asymmetry of the proton count rate above and below the reaction's scattering plane (Sub-section 4.3.2), the invariant $p\pi^0$ mass was used as the reference coordinate for determining the $Q-$values used for the final cross sections and observables $\{C_x,\, P,\, C_z\}$.

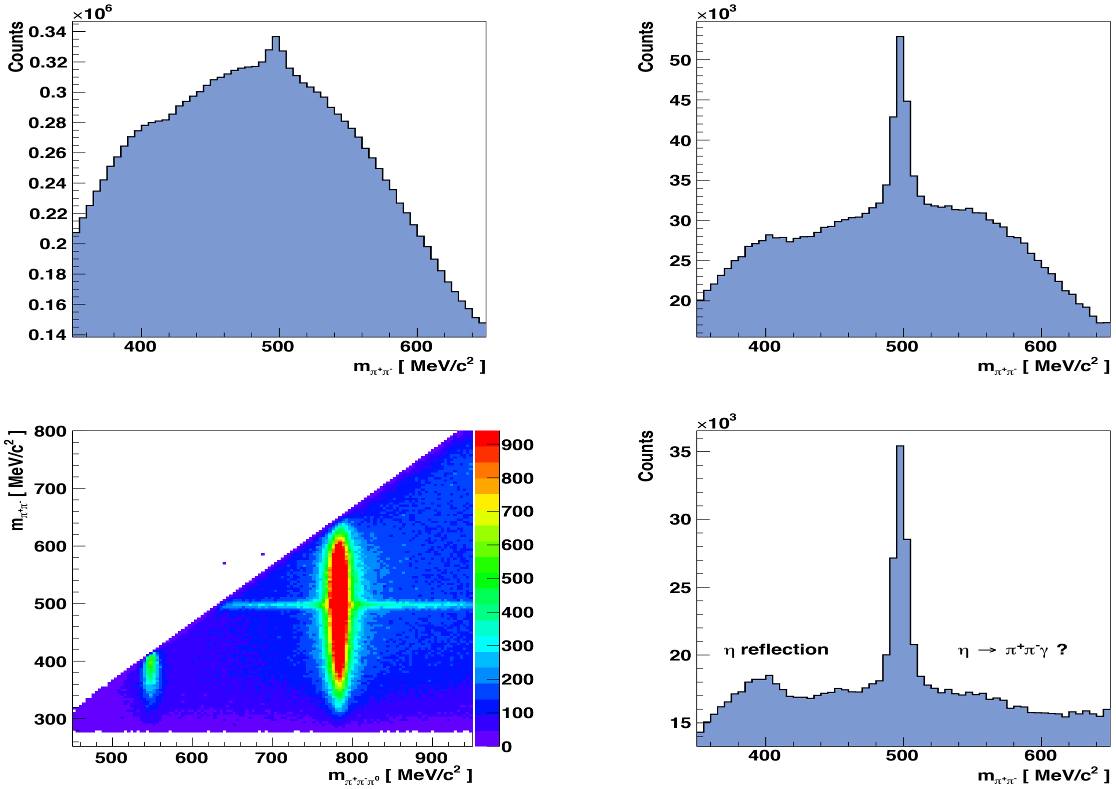

Figure 3.2: (Top row): Invariant *raw* $\pi^+\pi^-$ mass distribution of all $g12$ $\pi^+\pi^-\pi^0$ events contained in Period 2 (Table 3.1) (Left); same invariant mass $\pi^+\pi^-$ distribution after Σ^+ mass cut was applied, resulting in clear visibility of the K^0_S peak (Right). This reduced the background appreciably, while only marginally affecting the $K^0_S\Sigma^+$ statistics. (Bottom row): Invariant $\pi^+\pi^-\pi^0$ mass vs. $\pi^+\pi^-$ mass from all $g12$ $\pi^+\pi^-\pi^0$ events in Period 2 (Left); same invariant mass $\pi^+\pi^-$ distribution (shown in Top-Right figure) after the ω and Σ^+ mass cuts have been applied (Right). The peak around 400 MeV is the $\eta \to \pi^+\pi^-\pi^0$ reflection (cut off at the phase-space boundary), while the enhancement at 550 MeV is most likely due to the η decay into a $\pi^+\pi^-\gamma$ final-state. Comparing the Top and Bottom Right hand-side images, a marginal portion of $K^0_S\Sigma^+$ statistics were lost from the ω mass cut. Image source: [3]. Courtesy of Dr. Zulkaida Akbar (University of Virginia).

CHAPTER 4

GENERAL PHYSICS ANALYSIS

Once the application and calibration of the cuts and corrections was performed on the selected $g12$ data (Section 3.4), along with the appropriate implementation of the signal-background subtraction $Q-$factor method (Section 3.6), we then proceed to extract the set of *polarization observables* of interest to this analysis from the carefully selected $K^0\Sigma^+$ events, namely: the single $\{P\}$ and double-polarization $\{C_x,\ C_z\}$ observables from the $K^0\Sigma^+$ channel. To that end, we employed a 1-Dimensional (linear) fit to extract each double-polarization observable individually, followed by the implementation of a *Maximum Likelihood* fit, which allowed for the *simultaneous* extraction of every polarization observable we sought after.

4.1 Kinematics and Observables of $\gamma p \to K^0\Sigma^+$

The underlying kinematic variables describing the reaction,

$$\gamma(k) + p(p_p) \to K^0(p_{K^0}) + \Sigma^+(p_{\Sigma^+}), \tag{4.1}$$

given that their set of four-momenta, within the overall center-of-mass frame, are,

$$\begin{aligned} k &= (E_\gamma, \vec{k}), & p_{K^0} &= (E_{K^0}, \vec{p}_{K^0}) \\ p_p &= (E_p, -\vec{k}), & p_{\Sigma^+} &= (E_{\Sigma^+}, -\vec{p}_{K^0}), \end{aligned} \tag{4.2}$$

where $E_i = \sqrt{m_i^2 + |\vec{p}_i|^2}$ is the relativistic energy ($\forall\ i \in \{p,\ K^0,\ \Sigma^+\}$) and $E_\gamma = |\vec{k}|$, can be fully specified by a set of two variables: the *incident photon-beam energy* E_γ and the *cosine of the polar angle* of the K^0 meson within the center-of-mass frame of the reaction (i.e. $\cos\theta^{K^0}_{\text{c.m.}}$), with the $\hat{z}$-axis defined along the direction of the incident photon beam (i.e., the helicity axis of the incoming photons); see Figure **??**. This choice of kinematic variables follows from the proceeding argument. Consider then the energy-conservation relation,

$$E_\gamma + \sqrt{m_p^2 + E_\gamma^2} = \sqrt{m_{K^0}^2 + |\vec{p}_{K^0}|^2} + \sqrt{m_{\Sigma^+}^2 + |\vec{p}_{K^0}|^2}. \tag{4.3}$$

It can be seen from the previous expression that the K^0 momentum, namely $|\vec{p}_{K^0}|$, is defined as a function of the incoming photon beam energy E_γ. As such, it follows that the dynamics of the reaction are governed only by two kinematic variables: the cosine of the center-of-mass K^0 scattering angle ($\cos\theta^{K^0}_{\text{c.m.}}$) and the photon beam energy E_γ. In addition, the set of center-of-mass momenta expressions can be used to build the following set of *Mandelstam variables*,

$$s = (p_p + k)^2 = (p_{K^0} + p_{\Sigma^+})^2 \tag{4.4a}$$

$$t = (p_{K^0} - k)^2 = (p_{\Sigma^+} - p_p)^2 \tag{4.4b}$$

$$u = (p_{\Sigma^+} - k)^2 = (p_{K^0} - p_p)^2, \tag{4.4c}$$

which, for photoproduction processes, fulfill the following well-known relation,

$$s + t + u = m_p^2 + m_{K^0}^2 + m_{\Sigma^+}^2. \tag{4.5}$$

The final-state of the $K^0\Sigma^+$ channel consists of a meson ($M = K^0$) and a baryon ($B = \Sigma^+$). The coordinate system employed in this analysis to study the aforementioned reaction is known as the *Adair frame*, where the $\hat{z}$-axis is chosen to be in the *same* direction as the incoming initial photon beam in the overall center-of-mass frame. As such, the axes of the scattering plane are defined in terms of the *vector* components of the four-vectors of the incoming photon and the outgoing Σ^+. The direction normal to the production plane is taken as the $\hat{y}$-axis, the direction along the momentum vector of the incoming photon as the $\hat{z}$-axis, while the $\hat{x}$-axis is chosen so as to make the Adair-frame a right-handed coordinate system. The reaction is parameterized by,

$$\hat{y} = \frac{\vec{k} \times \vec{p}_{\Sigma^+}}{|\vec{k} \times \vec{p}_{\Sigma^+}|} \tag{4.6a}$$

$$\hat{z} = \frac{\vec{k}}{|\vec{k}|} \tag{4.6b}$$

$$\hat{x} = \hat{y} \times \hat{z}. \tag{4.6c}$$

The choice for the Adair frame set of coordinates plays a role in the measurement of the set of polarization observables $\{C_x,\ P,\ C_z\}$, which depend on the axes defined by the scattering plane. Furthermore within the known literature there are two common conventions used to discuss the beam-recoil polarization observable P. The hyperon polarization within the production plane can be described with respect to a $\hat{z}$-axis along the direction of the incoming beam (4.6b), or along

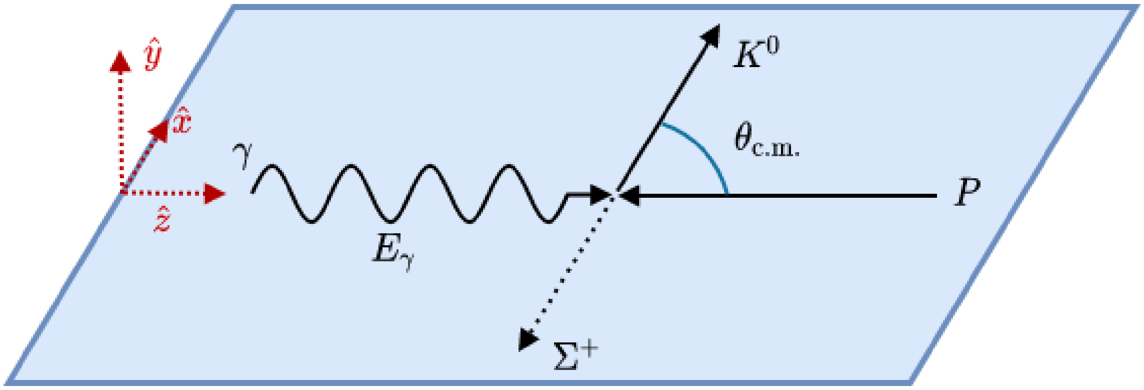

Figure 4.1: Schematic representation of the kinematics of the reaction $\gamma p \to K^0\Sigma^+$. The blue plane represents the center-of-mass production plane for the reaction, spanned by the incoming initial photon and the recoiling hyperon Σ^+ three-vector components. Here, $\theta_{\text{c.m.}}$ denotes the angle between the initial proton (p) and the K^0 meson within the overall center-of-mass frame. The choice of coordinate system employed for this analysis is known as the *Adair frame*, for which the $\hat{z}$-axis is chosen to be pointing along the direction of the incoming photon beam in the center-of-mass-frame. The $\hat{y}$-axis of this coordinate frame is perpendicular to the scattering plane, while the $\hat{x}$-axis lies within the production plane, making this frame a right-handed coordinate system.

the momentum axis of the produced K^0 meson. However, due to the fact that the polarization vector transforms according to the vector rules in three-dimensional space ($\mathbb{R}^3$), this choice makes no fundamental difference [50]. Ultimately, the induced polarization P of the recoiling hyperon Σ^+, within the center-of-mass rest-frame, is measured by determining the y-component of the Σ^+ polarization within the rest-frame of the hyperon. This is accomplished by first Lorentz boosting the proton four-momentum from the Laboratory frame into the center-of-mass frame, and then directly to the Σ^+ rest-frame. By subsequently defining the Σ^+ rest-frame's y-component as the *direction cosine* of the outgoing proton with respect to the scattering plane (Figure 4.1), we find,

$$\cos\theta^{\Sigma^+}_{p,\hat{y}} = \vec{p}_{\Sigma^+} \cdot \hat{y}, \tag{4.7}$$

where $\vec{p}_{\Sigma^+}$ represents the incoming proton vector-component in the Σ^+ rest-frame and $\hat{y}$ is given by (4.6a). Similarly, the double beam-recoil observables C_x and C_z are measured by determining the x and z components of the Σ^+ polarization, defined by the $\hat{x}$ and $\hat{z}$ components of the outgoing proton's direction cosines in the Σ^+ rest-frame, comparable to expression (4.7). This will be discussed further in Section 4.3.

4.1.1 Production, Formalism and Binning of the $\gamma p \to K^0\Sigma^+$ Reaction

Within the theoretical edifice of QCD, the potential between any two charged particles is dependent on the given distance between them. This distance can be interpreted as a momentum transfer (q), which is itself inversely proportional to the aforementioned distance. Unlike the coupling constant for QED, the QCD coupling constant α_S grows larger for smaller momentum transfer (q). As such, the QCD coupling constant satisfies the following *renormalization group equation*,

$$q^2 \frac{d\alpha_S}{dq^2} = \beta(\alpha_S) = -(b_0\alpha_S^2 + b_1\alpha_S^3 + b_2\alpha_S^4 + \cdots), \tag{4.8}$$

where b_i represent the loop correction β-function coefficients, given for the coupling of an *effective theory* in which they depend on the number of quark flavors f, with considerably light masses ($m_q \ll q$). Constraining our attention to an energy regime where the number of flavors is constant, one can arrive at an exact solution for the renormalization equation (see Section 1.1, equation 1.5).

The minus sign in equation (4.8) is indicative of the presence of asymptotic freedom (discussed in Section 1.1), a behavior which renders the strong coupling constant weak at processes involving large momentum transfers ("hard processes"), where $\alpha_S \sim 0.1$ for momentum transfers in the 100 GeV$-$1 TeV energy range. It is within this high energy regime that quarks behave as though they were *free particles*, therefore turning perturbation theory into a viable tool for the purposes of QCD calculations. On the other hand (see Section 1.1), at an energy scale of around 1 GeV the resulting interactions become strong enough to render perturbation theory powerless.

The diverging nature of α_S within this energetic regime is regularly taken as a sign of confinement, which takes place in the momentum transfer scale of $q \approx \Lambda_{\text{QCD}} \sim$100$-$300 MeV [25], where Λ_{QCD} corresponds to the energy scale where QCD is non-perturbative. Therefore, this long range-physics is effectively described by hadrons. For short-range physics, $q \gg 1$ GeV, quarks and gluons take a more direct role in the interactions. Additionally, the confinement domain is probed by reactions taking place at energy scales around the Λ_{QCD} cut-off value. Furthermore, due to the fact that the production scale of the strange quarks is governed by their mass, $m_{\text{s}} \approx 95$ MeV (which itself is within the range of the aforementioned Λ_{QCD} cut-off value), an important conclusion thus ensues: *hyperon production in reactions mediated by strong interactions furnish an unequivocal pathway for the study of the confinement regime of Quantum Chromodynamics* [4].

Hyperons can naturally decay either via strong or electromagnetic interactions so long as there exists a system of daughter particles that shares the same flavor quantum numbers, with a combined total mass lighter than the hyperon. If such decay modes are indeed possible, then they are the dominant ones. Electromagnetic interactions conserve strangeness and parity. Otherwise, if such decay modes are impossible, the hyperon will then decay via a weak interaction, thus *violating* conservation of strangeness and parity. On the other hand, decays which conserve strangeness require a Kaon and a Nucleon (due to baryon number conservation) to be part of their final-states.

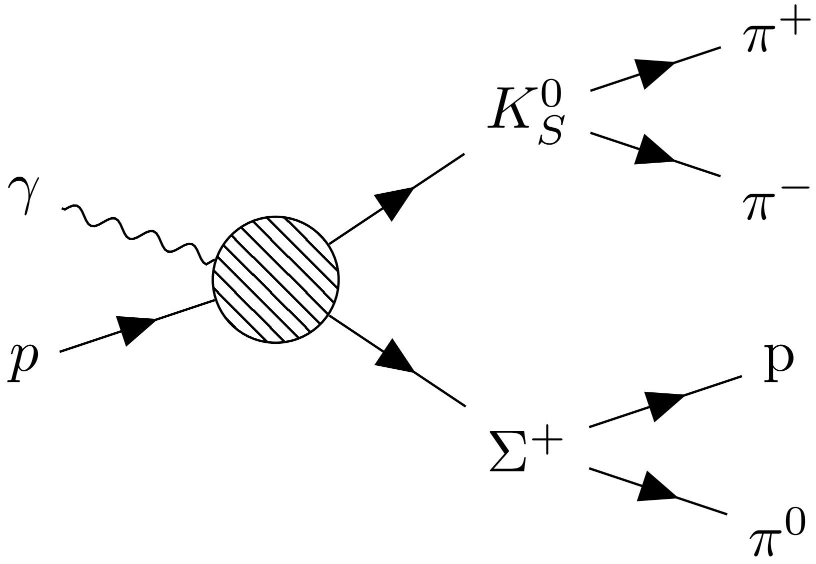

Figure 4.2: Feynman diagram illustrating the $\gamma p \rightarrow K_S^0 \Sigma^+$ reaction. The bubble diagram denotes a series of intermediate steps, represented by an infinite series of Feynman diagrams involved before arriving at the $K_S^0 \Sigma^+$ final-state. One of the main motivations for the extraction of the observables $\{C_x,\, P,\, C_z\}$ from $\gamma p \rightarrow K_0 \Sigma^+$ stems from the fact that their determination enables the study of the non-perturbative confinement regime of QCD, and hence the *intermediate* steps involved in the reaction. The quark content of K^0 is $(d\bar{s})$, while the quark content of Σ^+ is (uus); strangeness is conserved in this reaction. Lastly, the quark content of the final-states are: $K_S^0 \rightarrow \pi^+(u\bar{d}) + \pi^-(d\bar{u})$ and $\Sigma^+ \rightarrow p(uud) + \pi^0\left(\frac{u\bar{u}-d\bar{d}}{\sqrt{2}}\right)$. Strangeness is not conserved in either decay, thus both particles decay weakly. Image source: [15]. Courtesy of Louise Clark (University of Glasgow).

There is no denying of the overwhelming success of the Constituent Quark Model (CQM) in describing all observed baryon states. Nevertheless, there exist a number of baryon resonance states whose predicted existence either has yet to be observed, or have little supporting evidence [9]. Known as the *missing resonance* problem, current predictions claim that some of these states may decay mainly into Hyperon-Kaon (YK) final-states. It is also predicted that missing Nucleon (N^*) and Delta (Δ^*) resonances will decay into final-states of strange particles (ΛK or $K\Sigma$), and other non-strange final-states. Among the reactions studied by CLAS at JLab is $\gamma p \rightarrow K^0\Sigma^+$ (see Figure 4.2). Neither the K^0 nor the Σ^+ are directly measured by the CLAS detector, as they decay shortly after production. Therefore, both must be reconstructed from their detected final-states.

For this reaction, hyperons are polarized normal to the scattering plane (Figure 4.1). An experimental investigation of the hyperon polarization provides a window into the different amplitudes contributing to hyperon production, since the hyperon polarization results from the interfering nature between the spin-dependent and spin-independent parts of the scattering amplitude [44]. The final-state K^0 meson is a mixture of the short and long lived Kaon CP eigenstates K^0_S and K^0_L [22],

$$|K^0\rangle = \frac{1}{\sqrt{2}}(|K^0_S\rangle + |K^0_L\rangle). \tag{4.9}$$

Since the K^0_S is a short-lived meson, it quickly decays into a $\pi^+\pi^-$ pair, with a branching ratio (decay probability) of $69.20 \pm 0.05\%$ [60] via the CP conserving weak decay. On the other hand, the long-lived K^0_L meson decays *beyond* the range of the CLAS detector, with a mean travel distance of 15.34 m [60]; consequently, only the K^0_S mesons were considered in our analysis, as they have a mean travel distance of 2.6844 cm [60], thus decaying well within the range of CLAS. The Σ^+ hyperon decays into a proton and a π^0, with a branching ratio of $51 \pm 0.3\%$ [60] via a weak decay. Therefore the detected final-states of the reaction are composed of a proton (p), π^+ and π^-. The π^0 is reconstructed from the missing mass of the proton and the K^0_S, while the Σ^+ is reconstructed from the missing mass of the K^0_S by requiring the missing mass of the proton and K^0_S to be π^0. Therefore, the reaction can be fully stated as,

$$\gamma + p \rightarrow K^0_S + \Sigma^+ \rightarrow \pi^+ + \pi^- + p + \pi^0. \tag{4.10}$$

For the purposes of this analysis, we extracted the induced hyperon polarization P of Σ^+, along with the double-polarization observables C_x and C_z, using an incident-photon beam with an energy range of $1.15 < E_\gamma < 3.05$ GeV. To perform the extraction of the observables, the $g12$ data was binned into a single layer containing two independent kinematic variables describing the reaction, (E_γ, $\cos\theta^{\Sigma^+}_{\text{c.m.}}$): a set of 19 bins with a 100-MeV-wide photon-energy E_γ width, and 10 angular bins of $\cos\theta^{\Sigma^+}_{\text{c.m.}}$, each 0.1-wide, with an angular coverage of $[-1.0, 1.0]$. To extract the observables, the $\cos\theta^p_{x,y,z}$ angular distributions of the proton in the Σ^+ rest-frame, along with the weight ($Q-$value) for each event, were fed into a *probability density function* (PDF) to use the Unbinned Maximum

Likelihood fit technique. Both the Maximum Likelihood and Linear fitting methods are discussed further in Sub-sections 4.3.1 and 4.3.3.

4.2 The Formalism of Hyperon Polarization

The driving goal behind this thesis was to extract the set of observables $\{C_x, P, C_z\}$ via the application of data sets collected at the Jefferson Lab under the $g12$ experiment.

The photoproduction of a Σ^+ hyperon is generated via an electromagnetic, or a strong, interaction from an N^* state, and as such it is *parity conserving.* The parity conservation inherent to an electromagnetic, or a strong force, production allows for the induced polarization P of the Σ^+ hyperon to be produced exclusively along an axis perpendicular to the reaction's production plane (defined by 4.6a; see Figure 4.1). That being said, the Σ^+ decays into a proton and a π^0 via the weak force, which in turn is *parity violating.*

A direct consequence of this parity violation is that one can measure the polarization of the Σ^+ from the *angular distribution* of the decay products in the Σ^+ rest-frame, since the decay products contain information about their production. If the hyperons were produced with a given degree of polarization P in a reaction, then this polarization will make itself manifest in the angular distribution of the resulting daughter particles. This is known as a *self-analyzing* decay. The degree of parity violation involved in hyperon decay is characterized by the *weak decay asymmetry parameter* α, which is also manifestly observed within the angular distribution of the daughter particles. For the $\Sigma^+ \to p\pi^0$ decay, the angular distribution of the proton in the Σ^+ rest-frame is given by [18],

$$I(\cos\theta_y^p) = \frac{1}{4\pi}(1 + \alpha P \cos\theta_y^p), \tag{4.11}$$

where $\cos\theta_y^p$ is the proton polar angle with respect to the $\hat{y}$-axis in the Σ^+ rest-frame, and α measures the degree of parity mixing, which for our particular (Σ^+) reaction channel is given by $\alpha = -0.98 \pm 0.016$ [59]. Therefore, hyperon-recoil polarization observable P can be extracted by performing a counting experiment of the rate of protons above and below the scattering plane of the reaction (Figure 4.1). A convenient way used to derive the dependence of the angular distributions on the polarization observables is via the application of the *density matrix formalism*, a ubiquitous tool in the realm of Statistical and Quantum Mechanics. The proceeding Sub-sections will shortly digress into the density matrix formalism needed to understand and derive expression (4.11).

4.2.1 A Digression into the Density Matrix Formalism

Developed independently by John von Neumann and Lev Landau in 1927, and by Felix Bloch in 1946, the *density matrix formalism* is a useful tool employed to describe the statistical states of a system (also known as *ensembles*) in Quantum Mechanics [41]. Angular distributions can be parameterized using spin (polarization) observables via the use of the density matrix. In the realm of Quantum Mechanics, a pure ensemble is described by the same state-ket $|\Psi\rangle$, while mixed states, populated by a fraction a_i, are described by distinct state-kets $|\Psi_i\rangle$. Given a pure state $|\Psi\rangle$ the density matrix can be employed to find the expectation value of a given observable E,

$$\langle E\rangle = \langle\Psi|E|\Psi\rangle. \tag{4.12}$$

Using an orthonormal basis $\{\alpha_k\}$ we can insert a *completeness relation* of the eigenkets $|\alpha_k\rangle$ ($\sum_k |\alpha_k\rangle\langle\alpha_k| = \mathbb{1}$) on the expression above to rewrite the expectation value as follows,

$$\begin{aligned}\langle E\rangle &= \langle\Psi|\Big(\sum_k |\alpha_k\rangle\langle\alpha_k|\Big)E|\Psi\rangle = \sum_k \langle\Psi|\alpha_k\rangle\langle\alpha_k|E|\Psi\rangle \\ &= \sum_k \langle\alpha_k|E|\Psi\rangle\langle\Psi|\alpha_k\rangle = \sum_k \langle\alpha_k|(E|\Psi\rangle\langle\Psi|)|\alpha_k\rangle = \mathrm{Tr}(E|\Psi\rangle\langle\Psi|),\end{aligned} \tag{4.13}$$

where the *trace* of an operator X is defined as the sum of its diagonal elements, $\mathrm{Tr}(X) = \sum_{a'}\langle a^{'}|X|a^{'}\rangle$. Defining the density matrix of a pure state $|\Psi\rangle$ to be $\rho \equiv |\Psi\rangle\langle\Psi|$, the expectation value is now given by the trace of the product of the E observable and the density matrix ρ,

$$\langle E\rangle = \mathrm{Tr}(E\rho). \tag{4.14}$$

The power of the density matrix lies in the fact that it contains all physics information pertaining to the ensemble under consideration. On the other hand, in the case of a mixed state $|\Psi_i\rangle$, the density matrix results in the following expectation value for an observable E,

$$\begin{aligned}\langle E\rangle &= \sum_i a_i\langle\Psi_i|E|\Psi_i\rangle = \sum_i a_i\langle\Psi_i|\Big(\sum_k |\alpha_k\rangle\langle\alpha_k|\Big)E|\Psi_i\rangle \\ &= \sum_k \langle\alpha_k|\Big(E\sum_i a_i|\Psi_i\rangle\langle\Psi_i|\Big)|\alpha_k\rangle = \mathrm{Tr}\Big(E\sum_i a_i|\Psi_i\rangle\langle\Psi_i|\Big).\end{aligned} \tag{4.15}$$

In order to arrive at the same relation shown by equation (4.14), we need to redefine our density matrix as $\rho \equiv \sum_i a_i|\Psi_i\rangle\langle\Psi_i|$ (this is really an operator that becomes a matrix in a given basis), where $a_i = n_i/N$ (here, n_i represents the i occupancy numbers of the ensemble) is the probability that a randomly picked system out of the ensemble will be in the mixed-state $|\Psi_i\rangle$. In the case of a pure state the condition $\mathrm{Tr}(\rho) = 1$ holds, which can also hold for a mixed state as well, provided that we have $\sum_i a_i = 1$. Additionally, the density matrix is a *Hermitian operator* since it behaves as follows,

$$\rho^\dagger = (|\Psi\rangle\langle\Psi|)^\dagger = \langle\Psi|^\dagger|\Psi\rangle^\dagger = |\Psi\rangle\langle\Psi| = \rho. \tag{4.16}$$

An essential bit of knowledge about density matrices is their transformation properties; these are needed to describe particle reactions, such as particle decays. Let us then define a transformation operator T, whose physical interpretation is that it transitions an initial state $|\Psi\rangle$ into the final-state of a reaction, such that $T|\Psi_i\rangle = t_i|\Psi_i^{'}\rangle$. Therefore, the translation operator eigenvalues are,

$$t_i = \sqrt{\langle\Psi_i|T^\dagger T|\Psi_i\rangle}, \tag{4.17}$$

which guarantees that our transformed states $|\Psi_i^{'}\rangle$ will be normalized since,

$$\langle\Psi_i^{'}|\Psi_i^{'}\rangle = \frac{1}{t_i^2}\langle\Psi_i|T^\dagger T|\Psi_i\rangle = 1. \tag{4.18}$$

As such, the density matrix of the final-state is expressible in terms of the initial state [63],

$$\rho_{\text{final}} = T\rho_{\text{initial}}T^\dagger. \tag{4.19}$$

We can explicitly rewrite the above by using $\rho_{\text{initial}} = \sum_i a_i|\Psi_i\rangle\langle\Psi_i|$, to find the following,

$$T\rho_{\text{initial}}T^\dagger = T\left(\sum_i a_i|\Psi_i\rangle\langle\Psi_i|\right)T^\dagger = \sum_i a_i T|\Psi_i\rangle\langle\Psi_i|T^\dagger = \sum_i a_i t_i^2|\Psi_i^{'}\rangle\langle\Psi_i^{'}|. \tag{4.20}$$

This expression yields back equation (4.19), so long as both $a_i^{'} = a_i t_i^2$ and $\rho_{\text{final}} = \sum_i a_i^{'}|\Psi_i^{'}\rangle\langle\Psi_i^{'}|$, hold. Lastly, the angular distribution of the daughter particles from a final-state decay follows from expression (4.20), upon taking its trace,

$$I = \mathrm{Tr}(T\rho_{\text{initial}}T^\dagger), \tag{4.21}$$

where the transformation matrix T denotes the hyperon decay.

4.2.2 Single Hyperon Density Matrices

The density matrix formalism can be readily employed to describe the spin configuration of a hyperon. In this instance the density matrix is known as a *spin-density matrix.* In order to obtain the spin-density matrix for a particle with an arbitrary spin j, one can expand the spin density matrix via the use of Hermitian matrices Q^L_M, as follows [49, 63],

$$\rho = \frac{1}{2j+1}\mathscr{I} + \sum_{L=1}^{2j} \frac{2j}{2j+1} \sum_{M=-L}^{L} Q^L_M r^L_M, \tag{4.22}$$

where $\mathscr{I}$ represents the identity matrix, L is the angular momentum, M is the third component of angular momentum, and r^L_M denote a set of real polarization parameters. For the purposes of this thesis, only the spin-1/2 Σ^+ hyperon was considered. The Q^L_M matrices can be readily related to the multipoles T^L_M via the following relations [63],

$$Q^L_0 = \sqrt{\frac{2L+1}{2j}} T^L_0 \tag{4.23a}$$

$$Q^L_M = (-1)^M \sqrt{\frac{2L+1}{j}} \frac{1}{2}(T^L_M + T^{L^\dagger}_M) \tag{4.23b}$$

$$Q^L_{-M} = (-1)^L \sqrt{\frac{2L+1}{j}} \frac{1}{2i}(T^L_M - T^{L^\dagger}_M), \tag{4.23c}$$

where $M > 0$. In order to obtain an explicit expression for the spin-density matrix we can use *Wigner's 3-j symbol* to write the components of the T^M_L multipoles. In the physics literature, these are given by the following [41, 49],

$$(T^L_M)^m_n = \sqrt{2j+1} \begin{pmatrix} m & L & j \\ j & M & n \end{pmatrix} = \langle jnLM|jm\rangle. \tag{4.24}$$

In the case of a spin-1/2 hyperon, the spin-density matrix takes on a rather simple form since the Q^1_M matrices are given by the *Pauli spin matrices* [41],

$$\sigma_x = \begin{pmatrix} 0 & 1 \\ 1 & 0 \end{pmatrix}, \qquad \sigma_y = \begin{pmatrix} 0 & -i \\ i & 0 \end{pmatrix}, \qquad \sigma_z = \begin{pmatrix} 1 & 0 \\ 0 & -1 \end{pmatrix}, \tag{4.25}$$

while the r^1_M parameters are interpreted as the vector *polarization components* $P_{\Sigma^+_x}$, $P_{\Sigma^+_y}$ (given by P in our notation) and $P_{\Sigma^+_z}$. Therefore through the use of equation (4.22) we find that the spin-density matrix for a spin-1/2 hyperon is therefore given by [63],

$$\rho(1/2) = \begin{pmatrix} \rho_{11} & \rho_{1-1} \\ \rho_{-11} & \rho_{-1-1} \end{pmatrix} = \frac{1}{2}(\mathscr{I} + \vec{P}_{\Sigma^+} \cdot \vec{\sigma}) = \frac{1}{2} \begin{pmatrix} 1 + P_{\Sigma^+_z} & P_{\Sigma^+_x} + iP_{\Sigma^+_y} \\ P_{\Sigma^+_x} - iP_{\Sigma^+_y} & 1 - P_{\Sigma^+_z} \end{pmatrix}. \tag{4.26}$$

The vector polarization components of our spin-density matrix are dependent upon the underlying production mechanics of the hyperon. Since the strong production of the Σ^+ hyperon conserves parity, this can be used to impose a series of symmetry constraints on the spin-density matrix elements by defining a reference frame such that the $\hat{x}$ and $\hat{z}$-axes span the production plane, with the $\hat{y}$-axis being perpendicular to the scattering plane (shown in Figure 4.1). Therefore, conservation of parity dictates that the spin-density matrix takes on the following representation,

$$\rho(1/2) = \begin{pmatrix} \rho_{11} & \rho_{1-1} \\ -\rho_{1-1} & \rho_{11} \end{pmatrix}. \tag{4.27}$$

A direct comparison between equation (4.26) and equation (4.27) shows that the following set of constraints can be placed on the spin-density matrix elements,

$$-\rho_{1-1} = \rho_{-11} \tag{4.28a}$$

$$\rho_{11} = \rho_{-1-1}. \tag{4.28b}$$

The implication of this result indicates that the $\hat{x}$ and $\hat{z}$ vector polarization components are in fact zero, $P_{\Sigma^+_x} = P_{\Sigma^+_z} = 0$; therefore the spin-density matrix takes on the simple form,

$$\rho(1/2) = \frac{1}{2}\begin{pmatrix} 1 & iP_{\Sigma^+_y} \\ -iP_{\Sigma^+_y} & 1 \end{pmatrix}. \tag{4.29}$$

This result thus states that the hyperon is exclusively polarized perpendicularly to the scattering plane (i.e. it arises only along the $\hat{y}$-axis). In the case of a spin-1/2 hyperon decaying into a spin-1/2 baryon accompanied by a pseudoscalar spin-0 meson (for our analysis this is the reaction $\Sigma^+ \rightarrow p\pi^0$), described by a transformation matrix T, the angular distribution of the outgoing proton is furnished by employing expression (4.21). Furthermore, conservation of total spin states that the ensuing final-state can either have an angular momentum of 0 or 1 with a parity of $(-1)^{L+1}$. However due to the fact that the hyperon decay is weak, both the parity conserving state P and parity violating state S are equally allowed. The elements of the transformation decay matrix $T(1/2 \rightarrow 1/2\ \ 0)_{2m_{\text{bar}}2m_{\text{hyp}}}$ consist of S and P amplitudes T_s and T_p and the appropriate spherical harmonics (these are functions of the decay angles θ and ϕ) and Clebsch-Gordan coefficients [63],

$$T(1/2 \rightarrow 1/2\ \ 0)_{11} = T_s Y_0^0 + \frac{1}{\sqrt{3}} T_p Y_1^0 \tag{4.30a}$$

$$T(1/2 \rightarrow 1/2\ \ 0)_{-11} = -\sqrt{\frac{2}{3}} T_p Y_1^0 \tag{4.30b}$$

$$T(1/2 \rightarrow 1/2\ \ 0)_{1-1} = \sqrt{\frac{2}{3}} T_p Y_1^{-1} \tag{4.30c}$$

$$T(1/2 \rightarrow 1/2\ \ 0)_{-1-1} = T_s Y_0^0 - \frac{1}{\sqrt{3}} T_p Y_1^0. \tag{4.30d}$$

The relations above can be economically encapsulated by recasting them into a matrix expression (while inserting the corresponding spherical harmonic expressions) [63],

$$T(1/2 \rightarrow 1/2 \;\; 0) = \frac{1}{\sqrt{4\pi}} \begin{pmatrix} T_s + T_p \cos\theta & T_p \sin\theta e^{-i\phi} \\ T_p \sin\theta e^{i\phi} & T_s - T_p \cos\theta \end{pmatrix}, \tag{4.31}$$

where θ and ϕ represent the polar and azimuthal angles in the hyperon rest-frame. In order to simplify the derivation of the angular distribution of the hyperon decay product, one can make use of the fact that the trace of a matrix is invariant under cyclic permutations, i.e. $\mathrm{Tr}(T\rho T^\dagger) = \mathrm{Tr}(\rho T^\dagger T)$. As such the calculation of the matrix $A \equiv T^\dagger T$ is performed as a first step in our calculation,

$$A(1/2 \rightarrow 1/2 \;\; 0) = \frac{1}{4\pi} \begin{pmatrix} 1 + \alpha \cos\theta & \alpha \sin\theta e^{-i\phi} \\ \alpha \sin\theta e^{i\phi} & 1 - \alpha \cos\theta \end{pmatrix}, \tag{4.32}$$

where we have introduced the asymmetry parameter α. The asymmetry parameters are defined in terms of the following combinations of the S and P amplitudes T_s and T_p,

$$\alpha \equiv 2\Re(T_s^* T_p) \tag{4.33a}$$

$$\beta \equiv 2\Im(T_s^* T_p) \tag{4.33b}$$

$$\gamma \equiv |T_s|^2 - |T_p|^2. \tag{4.33c}$$

These asymmetry parameters are numbers defined within the range of $[-1.0, 1.0]$, and need to be individually measured for every specific decay. These parameters also fulfill the following relation by construction: $\alpha^2 + \beta^2 + \gamma^2 = |T_s|^2 + |T_p|^2 = 1$. Armed with this result, and using the spin-density matrix obtained from equation (4.29), the angular distribution takes on the form,

$$I(\theta, \phi) = \mathrm{Tr}(\rho(1/2) A(1/2 \rightarrow 1/2 \;\; 0)) = \frac{1}{4\pi}(1 + \alpha P_{\Sigma_y^+} \sin\theta \sin\phi). \tag{4.34}$$

This angular distribution can be written in terms of Cartesian coordinates by expressing it as a function of the opening angles between the outgoing daughter particle (namely the proton with respect to the Σ^+ hyperon) and the polarization axis. These opening angles are defined via,

$$k_x \equiv \cos\theta_x^p = \sin\theta \cos\phi \tag{4.35a}$$

$$k_y \equiv \cos\theta_y^p = \sin\theta \sin\phi \tag{4.35b}$$

$$k_z \equiv \cos\theta_z^p = \cos\theta. \tag{4.35c}$$

Henceforth, the angular distribution in Cartesian coordinates is given by,

$$I(k_y) = \frac{1}{4\pi}(1 + \alpha P_{\Sigma_y^+} k_y), \tag{4.36}$$

which depends on two parameters, the decay asymmetry α, which describes the hyperon's decay, and the hyperon polarization $P_{\Sigma_y^+}$, which is related to the underlying production process and thus depends on both the scattering angle of the hyperon and the center-of-mass energy of the reaction. Consequently, the spin-observable $P_{\Sigma_y^+}$ (from this point forward, this will be denoted by P) can be extracted from the resulting angular distribution of the hyperon's (Σ^+) decay products, which in this case is the proton.

Armed with this discussion on the single polarization observable P (which represents the hyperon recoil polarization) and the underlying theory of density matrices, we now turn to polarization observables characterizing reactions under a combination of beam and baryon recoil polarization, namely C_x and C_z. The experiment carried out to record the $g12$ data sets made use of a circularly polarized photon beam. The spin-dependent cross section for the $\gamma p \to K^0\Sigma^+$ reaction can be written in terms of the polarization observables of interest for this analysis [50],

$$\rho_{\Sigma^+}\frac{d\sigma}{d\Omega_{K^0}} = \left.\frac{d\sigma}{d\Omega_{K^0}}\right|_{\text{unpol.}} \{1 + \sigma_y P + P_{\odot}(C_x\sigma_x + C_z\sigma_z)\}, \tag{4.37}$$

where $P_{\odot}$ denotes the degree of the circular photon beam polarization with a range spanning $[-1.0, 1.0]$, $\sigma_{x,y,z}$ represent the Pauli spin matrices and ρ_{Σ^+} is twice the density matrix of the ensemble of recoiling Σ^+ hyperons (previously stated by equation 4.26),

$$\rho_{\Sigma^+} = (\mathscr{I} + \vec{P}_{\Sigma^+}\cdot\vec{\sigma}), \tag{4.38}$$

where $\vec{P}_{\Sigma^+}$ represents the measured polarization components of the recoiling hyperons. In order to measure the observables of interest, an appropriate coordinate system describing the reaction *must* be defined (discussed in Section 4.1). A direction relationship between the Σ^+ recoil polarization components $\vec{P}_{\Sigma^+}$ and the set of polarization observables $\{C_x,\ P,\ C_z\}$ can be obtained by taking the expectation value of the Pauli-spin matrix operators $\vec{\sigma}$ acting on the hyperon density matrix ρ_{Σ^+} via the trace relation $\vec{P}_{\Sigma^+} = \mathrm{Tr}(\rho_{\Sigma^+}\vec{\sigma})$. This leads to the following identifications [50],

$$P_{\Sigma_x^+} = P_{\odot}C_x \tag{4.39a}$$

$$P_{\Sigma_y^+} = P \tag{4.39b}$$

$$P_{\Sigma_z^+} = P_{\odot}C_z. \tag{4.39c}$$

It is clear from the previous set of relations that while the $\hat{y}$ component of the induced hyperon polarization $P_{\Sigma^+_y}$ is equivalent to the P observable, the $\hat{x}$ and $\hat{z}$ components of the hyperon polarization within the scattering plane are proportional to the double-polarization observables C_x and C_z, up to a constant given by the beam polarization factor $P_\odot$. The hyperon polarization components $\vec{P}_{\Sigma^+}$ are measured via the angular distribution of the decay protons of the hyperon within its rest-frame. Extending the result obtained from the derivation leading up to expression (4.36), the decay distribution $I_i(\cos\theta^p_i)$, as it relates to the hyperon polarization components (4.39a-4.39c) within the hyperon rest-frame, can be stated as follows [50],

$$I_i(\cos\theta^p_i) = \frac{1}{4\pi}(1 + \alpha P_{\Sigma^+_i}\cos\theta^p_i), \tag{4.40}$$

where $\cos\theta^p_i$ denotes the polar angular component of the proton with respect to a specific axis ($i \in \{\hat{x}, \hat{y}, \hat{z}\}$ is one of the three axes) in the hyperon rest-frame and $P_{\Sigma^+_i}$ denotes the hyperon polarization component of interest. Physically, the polarization observables C_x and C_z characterize the amount of transferred circular polarization (helicity) originating from an incident circularly polarized photon beam on an unpolarized target, and into the produced recoiling hyperon (for this analysis, the Σ^+) along the axes describing the production plane in the hyperon's rest-frame [50]. Further discussion into the fitting procedures implemented for the extraction of the set of observables $\{C_x,\, P,\, C_z\}$ will be detailed within the following Section.

4.3 Analysis Techniques

The analysis contained within this thesis adheres to two different strategies for the extraction of the set of single and double-polarization observables $\{C_x,\, P,\, C_z\}$. The first method uses the photon beam helicity states to construct an *asymmetry.* The beam helicity is defined as the projection of the normalized component of the beam polarization along its direction of momentum. If the electron beam helicity $P_\odot$ can be quickly and regularly flipped, then the most straightforward way to find the double-polarization observables $\{C_x,\, C_z\}$ is to construct the resulting asymmetry $A(\cos\theta^p_i)$ as a function of the proton angular distribution by keeping a record of the number of positive and negative helicity state events $N_\pm$ of the photon-beam in each angular bin. In the case of the $g12$ experiment, the electron beam helicity was flipped at a rate of 30 Hz [55].

When the incoming photons are circularly polarized, so that they are spin polarized parallel or anti-parallel with respect to the direction of the beam, their polarization may then be transferred fully or partially into the ensuing hyperons, thus giving rise to hyperon polarization components within the scattering plane. The double-polarization observables C_x and C_z give a characterization of this polarization transfer from a circularly polarized beam into the recoiling Σ^+ hyperon along the orthogonal axes of the scattering plane.

Once the ensuing asymmetry has been built, the C_i ($i \in \{\hat{x}, \hat{z}\}$) observables are *individually* extracted by performing a 1-Dimensional fit on the asymmetries as a function of the angular distribution of the proton. In the case of the hyperon-recoil polarization observable P, its extraction did not require a 1-Dimensional fit but was instead found via an asymmetry consisting of the counting rate of decay protons above and below the Σ^+ scattering plane; as such, its extraction will be treated separately in Sub-section 4.3.2.

A second far more sophisticated method employed in this analysis is the event-by-event based method known as the *Unbinned Maximum Likelihood fit.* The Likelihood fit employs information from every individual event and does not require binning, thus preventing any potential loss of information in the form of asymmetry features, due to the binning of the data. This method enables the *simultaneous* extraction of the observables $\{C_x, P, C_z\}$. The details underlying each of the aforementioned fitting procedures, as employed by this analysis, are described in Subsections 4.3.1 and 4.3.3.

4.3.1 One-Dimensional Fit Method

The main objective of this analysis was to extract the polarization observables $\{C_x, C_z, P\}$ via the use of $g12$ CLAS data for photon energies of $1.15 < E_\gamma < 3.05$ GeV, as a function of the $\cos\theta_i^p$ scattering angles. The helicity dependent double-polarization observables C_x and C_z were extracted by binning them in two kinematics variables describing the reaction $\gamma p \to K^0\Sigma^+$: 19 energy bins, 100 MeV-wide, of the incoming photon-beam E_γ, and 10 angular bins of the Σ^+ hyperon in the scattering plane within the center-of-mass frame (i.e. $\cos\theta_{\text{c.m.}}^{\Sigma^+}$), with a range of $[-1.0, 1.0]$.

The simplest method, commonly employed in CLAS analyses [8, 50], uses a 1-Dimensional (1D) fit. Given a photon energy E_γ, the general polarized differential cross section for pseudoscalar meson photoproduction off a proton can be readily expressed in terms of sixteen different polarization observables, along with the degrees of polarization of the photon beam and the target. The differential cross-section for the case of a double-polarization experiment with polarized photons and an ensuing recoil hyperon polarization is given by [29],

$$\begin{aligned}\frac{d\sigma}{d\Omega d\phi} = \left(\frac{d\sigma}{d\Omega}\right)\Big|_{\text{unpol.}} &\{1 - P_T\Sigma\cos 2\phi \\ &+ \alpha\cos\theta_x^p(-P_T O_x \sin 2\phi - P_\odot C_x) \\ &- \alpha\cos\theta_y^p(-P + P_T T\cos 2\phi) \\ &- \alpha\cos\theta_z^p(P_T O_z \sin 2\phi + P_\odot C_z)\},\end{aligned} \tag{4.41}$$

where $(d\sigma/d\Omega)|_{\text{unpol.}}$ denotes the unpolarized differential cross section, P_T and $P_\odot$ denote the linear and circular polarization coefficients of the photon beam, respectively, ϕ represents the azimuthal angle between the linear photon polarization vector and the scattering plane, α is the weak decay asymmetry, while $\cos\theta_x^p$, $\cos\theta_y^p$ and $\cos\theta_z^p$ represent the direction cosines of the three-momentum vector components of the decay proton, as defined within the rest-frame of the Σ^+ hyperon. Lastly, the set of observables $\{\Sigma,\ P,\ T,\ O_x,\ O_z,\ C_x,\ C_z\}$ represent, respectively: beam spin asymmetry, Σ^+ induced hyperon polarization, target polarization, polarization transfer components to the Σ^+ from linearly polarized photons, and polarization transfer components to the Σ^+ stemming from circularly polarized photons. A direct integration of the differential cross section given by (4.41) over the azimuthal angle ϕ, in the range of $[0, 2\pi]$, simplifies its form since it cancels out all terms that depend on the linear polarization, along with all the other observables not of interest to this analysis, leading to a differential cross section expressed purely in terms of $\{C_x,\ P,\ C_z\}$ [8],

$$\frac{d\sigma^\pm}{d\Omega} = \left(\frac{d\sigma}{d\Omega}\right)\Big|_{\text{unpol.}} \{1 \pm \alpha P_\odot(C_x\cos\theta_x^p + C_z\cos\theta_z^p) + \alpha P\cos\theta_y^p\}, \tag{4.42}$$

where ± represents the helicity state of the incoming photon beam.

The asymmetry could then be built as a function of the proton angular distribution, so as to perform a linear fit. To that end, the number of positive and negative beam helicity state events were recorded for each angular bin. By directly integrating expression (4.42) over its direction cosines $\cos\theta_{x,y,z}^p$, the beam-helicity asymmetry can be expressed in the following manner [8, 50],

$$\begin{aligned}A(\cos\theta_i^p) &= \frac{N_+ - N_-}{N_+ + N_-} \\ &= \frac{\iint \frac{d\sigma^+}{d\Omega} d(\cos\theta_y^p)d(\cos\theta_i^p) - \iint \frac{d\sigma^-}{d\Omega} d(\cos\theta_y^p)d(\cos\theta_i^p)}{\iint \frac{d\sigma^+}{d\Omega} d(\cos\theta_y^p)d(\cos\theta_i^p) + \iint \frac{d\sigma^-}{d\Omega} d(\cos\theta_y^p)d(\cos\theta_i^p)} \\ &= \alpha P_\odot C_i\cos\theta_i^p,\end{aligned} \tag{4.43}$$

where $\cos\theta_i^p$ ($i \in \{\hat{x}, \hat{z}\}$) represents the angular distribution of the decay protons in the Σ^+ rest-frame, and $N_\pm$ denotes the helicity-dependent hyperon yield for each event. Expression (4.43) shows that the asymmetry is indeed a linear function dependent on the cosine of the proton angle, whose slope results in the double-polarization observables C_x and C_z.

Figure 4.3 displays an example of proton angular distribution asymmetries for the reaction $\gamma p \to K^0\Sigma^+$, for the double-polarization observables $C_{x/z}$, as a function of the proton angular distribution $\cos\theta^p_{x/z}$. Subsequently, the asymmetries were plotted against $\cos\theta^i_p$, and linear fits were used to find the slopes of the angular proton distributions; the free parameters were the product $\alpha P_\odot \cos\theta^p_i$ ($i \in \{x, z\}$), which were equated to the slopes to extract the observables $C_{x/z}$.

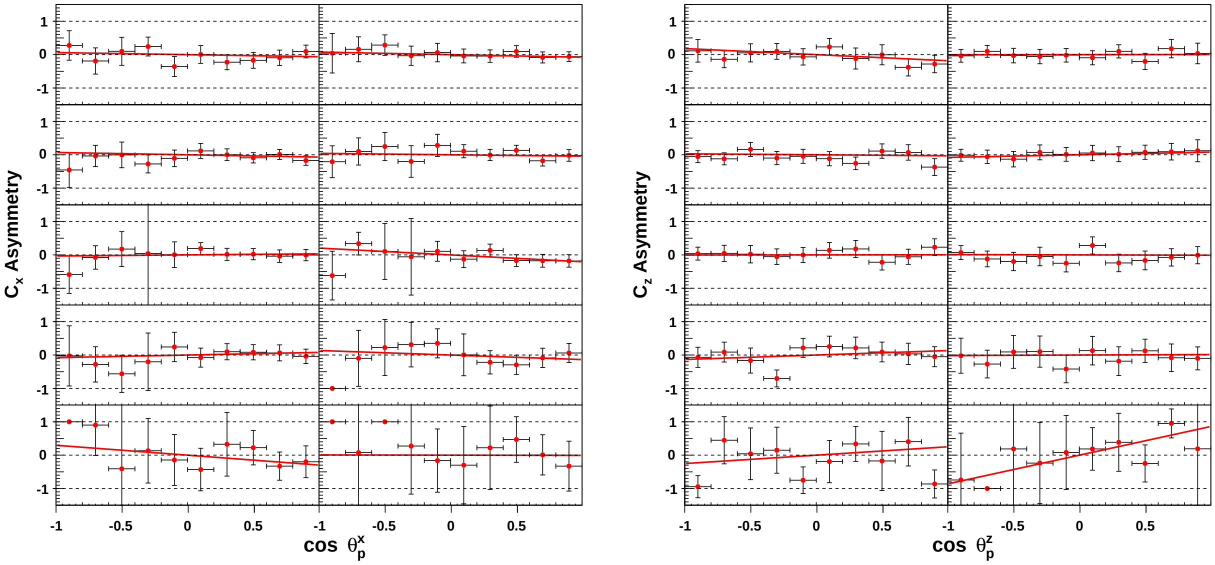

Figure 4.3: (Left/Right): An example of the beam helicity $C_{x/z}$ asymmetries, as a function of the proton angular distribution in the Σ^+ rest-frame ($\cos\theta^{\Sigma^+}_{\text{c.m.}}$), for the lowest energy bin in the analysis ($E_\gamma = 1150$ MeV). The asymmetries were further binned in 10 $\cos\theta^{\Sigma^+}_{\text{c.m.}}$ angular bins, with a range of $[-1.0, 1.0]$. These distributions used a different set of $Q-$values. Performing a linear fit (equation 4.43) to the angular distributions allowed us to extract the C_x and C_z observables.

While a hyperon decay allows for the measurement of asymmetries, from which we linearly extracted the observables $C_{x/z}$ via (4.43), there's a trade-off in the form of low cross-sections inherent to this reaction, which led to consistently large error bars due to the low statistics. Counting statistics were poorest at higher energies and forward angles, where the cross sections were the smallest. The statistics were better behaved at lower energies and backward angles. The uncertainties placed on the observables $C_{x/z}$ are a result of the fit uncertainty originating from the 1-Dimensional fit to the asymmetry angular proton distribution. Overall, we found that both polarization observables $C_{x/z}$ were mostly flat for the energy and angle bins considered for this analysis.

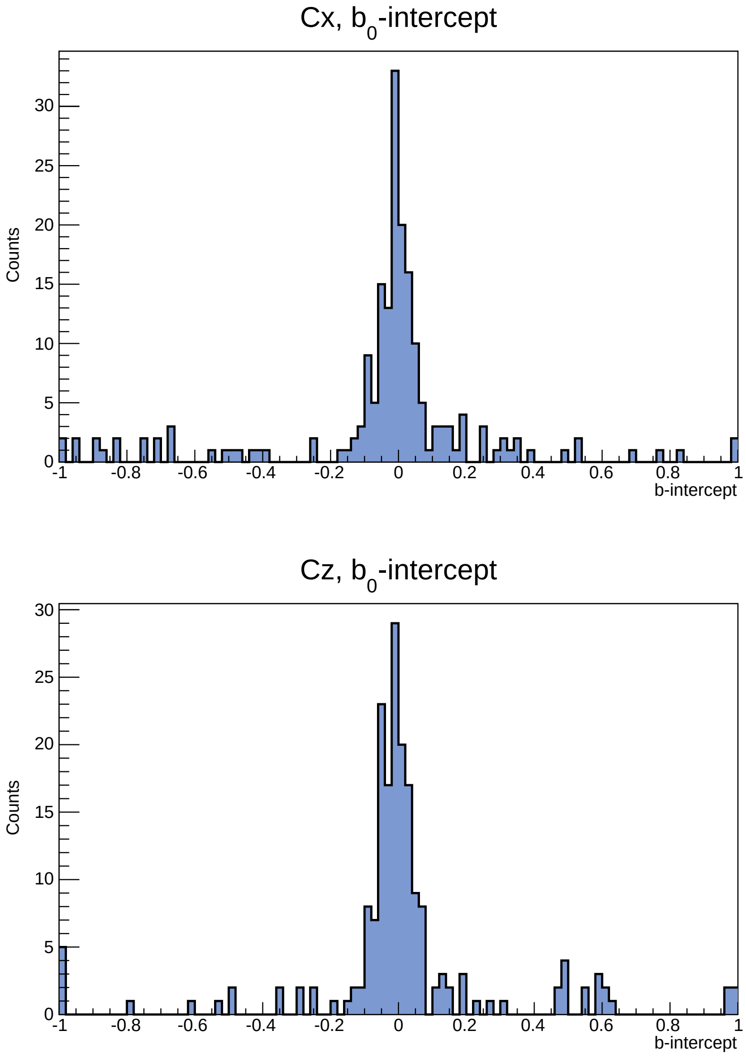

Figure 4.4: (Top/Bottom): Distribution of the b_0-intercept parameter for the extraction of the $C_{x/z}$ observables. It was found that a linear fit, following the prescription of (4.44), had little influence on the extracted observables $C_{x/z}$ (Figure 4.3), as obtained from the asymmetry $A(\cos\theta_i^p)$ (4.43).

In an effort to study if these effects were influenced by the linear fit prescribed by equation (4.43), the data was fitted and uniformly shifted using the following first-order polynomial,

$$A(\cos\theta_i^p) = \alpha P_{\odot} C_i \cos\theta_i^p + b_0, \tag{4.44}$$

where b_0 represents a constant intercept parameter. We found no noticeable differences between the observables $C_{x/z}$ extracted via the fits (4.43) and (4.44). Figure 4.4 shows the Gaussian-like distributions of the b_0-intercept parameters from (4.44), with most fits showing no effect from being shifted by a constant b_0, and thereby leaving the extracted observables unaffected.

The error bars present on the performed asymmetries are purely statistical in nature. Their errors can be analytically calculated via the standard tools of error propagation,

$$\delta_A = \sqrt{\delta^2_{N_+}\left(\frac{\partial A}{\partial N_+}\right)^2 + \delta^2_{N_-}\left(\frac{\partial A}{\partial N_-}\right)^2}, \tag{4.45}$$

where $\delta_{N_\pm}$ represents the yield uncertainties on the number of counts for a specific helicity state. A straightforward calculation shows that,

$$\frac{\partial A}{\partial N_\pm} = \pm\frac{2N_\mp}{(N_+ + N_-)^2}. \tag{4.46}$$

We find that the total statistical uncertainty of the asymmetries, added in quadrature, is given by the following expression,

$$\delta_A = \frac{2}{(N_+ + N_-)^2}\sqrt{\delta^2_{N_+}N^2_- + \delta^2_{N_-}N^2_+}, \tag{4.47}$$

Additionally, without loss of generality, expression (4.48) may be rewritten as,

$$\delta_A = \frac{2}{(N_+ + N_-)^2}\sqrt{N_+N^2_- + N_-N^2_+}, \tag{4.48}$$

where we have made use of the fact that $\delta_{N_\pm} = \sqrt{N_\pm}$. Thus, the uncertainties on the C_x and C_z observables derive from the uncertainty of the linear fit, as performed to the asymmetry distributions given by (4.43).

4.3.2 Extraction of Hyperon Polarization Observables in $\gamma p \rightarrow K^0\Sigma^+$, Using the g12 Data Sets

The equivalence of the hyperon induced recoil polarization $\hat{y}$-component $P_{\Sigma^+_y}$ (4.39b) to the P observable, coupled with equation (4.40), gave a direct path for the extraction of the single polarization observable P. The induced hyperon polarization P was binned in 19 energy bins of the incoming photon beam E_γ, with a range of $1.15 < E_\gamma < 3.05$ GeV. The Σ^+ hyperon is produced via the electromagnetic (or alternatively the strong) force (both being parity conserving), and eventually decays into a proton and a π^0 via the parity violating weak force. This parity violation in turn ensures that the polarization of the Σ^+ can be extracted from the angular distribution of one of its decay products within its rest-frame (see Section 4.1). This is illustrated by Figure 4.5.

Let us then recall that the angular distribution of the outgoing proton in the Σ^+ rest-frame is,

$$I_y(\cos\theta_y^p) = \frac{dN}{d\cos\theta_y^p} = \frac{1}{4\pi}(1+\alpha P\cos\theta_y^p), \tag{4.49}$$

where $\cos\theta_y^p$ represents the angle between the momentum vector of the proton in the Σ^+ rest-frame and the normal direction of the scattering plane, while α is the degree of parity mixing.

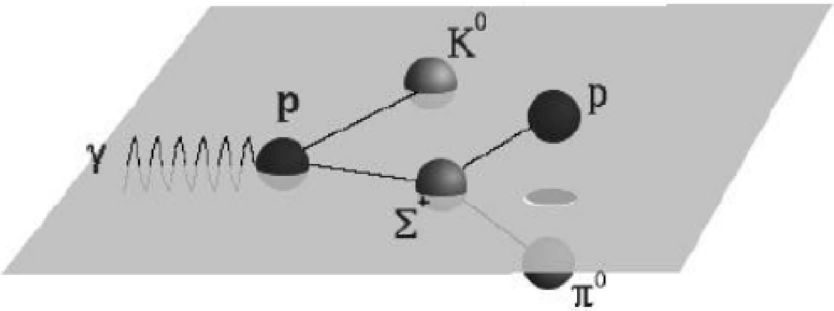

Figure 4.5: Scattering plane of the $\gamma p \to K^0\Sigma^+$ reaction, defined by the momenta of the incoming photon beam γ and the outgoing Σ^+ hyperon in the center-of-mass frame. This arrangement allowed us to find the number of protons above and below the scattering plane, resulting in the P observable of Σ^+ (4.52). Image source: [11]. Courtesy of Dr. Ralph Castelijn (Shell, Netherlands).

Expression (4.49) can be split up into two parts representing the upwards (N_U) and downwards (N_D) proton angular distribution rates with respect to the scattering plane [44],

$$\begin{aligned}
N_\mathrm{U}(\cos\theta_y^p) &= \frac{dN_\mathrm{U}}{d\cos\theta_y^p} \\
&= \frac{1}{4\pi}(1+\alpha P\cos\theta_y^p) \quad \text{for} \quad 0 \le \cos\theta_y^p \le 1, \qquad (4.50\text{a})\\
N_\mathrm{D}(\cos\theta_y^p) &= \frac{dN_\mathrm{D}}{d\cos\theta_y^p} \\
&= \frac{1}{4\pi}(1-\alpha P\cos\theta_y^p) \quad \text{for} \quad -1 \le \cos\theta_y^p \le 0. \qquad (4.50\text{b})
\end{aligned}$$

Adding both of the relations above, we arrive at the following expression for the P observable,

$$\alpha P\cos\theta_y^p = \left[\frac{N_\mathrm{U}(\cos\theta_y^p) - N_\mathrm{D}(\cos\theta_y^p)}{N_\mathrm{U}(\cos\theta_y^p) + N_\mathrm{D}(\cos\theta_y^p)}\right], \tag{4.51}$$

where $\cos\theta_y^p$ is constrained within the range of $[0.0, 1.0]$. The advantage of using the rate of upwards and downwards proton angular distributions is that it cancels acceptance corrections effects in the asymmetry (working under the assumption that their acceptance corrections are indeed the same), since the detector is (approximately) ϕ-symmetric. Therefore, to determine the hyperon polarization observable, a direct integration of all events above and below the reaction plane over $\cos\theta_y^p$, (so that no direct angle dependence on the proton is required, i.e. no angular binning, as it is required for the C_x and C_z observables) yields the following expression for the P observable [44],

$$P = \frac{2}{\alpha} \cdot \left[\frac{N_{\mathrm{U}} - N_{\mathrm{D}}}{N_{\mathrm{U}} + N_{\mathrm{D}}} \right]. \tag{4.52}$$

Therefore, the measurement of the Σ^+ induced recoil polarization P is effectively reduced to a counting experiment as it is based on the asymmetry between the proton count rate above and below the reaction plane. As mentioned in Section 4.1 (equation 4.7), whether a proton is above or below the reaction plane (see Figure 4.5) depends on the following condition,

$$\cos\theta_{p,\hat{y}}^{\Sigma^+} = \begin{cases} \vec{p}_{\Sigma^+} \cdot \hat{y} > 0, & \text{for protons above the scattering plane,} \\ \vec{p}_{\Sigma^+} \cdot \hat{y} < 0, & \text{for protons below the scattering plane.} \end{cases}$$

Here, $\cos\theta_{p,\hat{y}}^{\Sigma^+}$ represents the angle of the $\hat{y}$-component of the outgoing proton in the Σ^+ rest-frame, and $\vec{p}_{\Sigma^+}$ represents the proton momenta in the rest-frame of the Σ^+. Furthermore, since the P observable does not require the beam's helicity data, one can think of the P observable as the "C_y" observable, similar in nature to the double-polarization observables C_x and C_z.

4.3.3 The Maximum Likelihood Fit Method

The process of accurately determining the approximate value of a parameter of interest, given a set of measured data, is known as *parameter estimation.* For the 1-Dimensional method, outlined in Sub-section 4.3.1, the asymmetries of the data were fitted via the use of a *least squares method*, where each asymmetry was binned in accordance to the angular distribution of the proton in the Σ^+ rest-frame. The quality of the binning was in turn dependent on the number of events (i.e. the amount of available statistics). Consequently, the binning of the data can potentially obscure some important characteristics of the asymmetries [40].

In order to mitigate these issues, there exists a far more sophisticated fitting technique, known as the *Unbinned Maximum Likelihood fit* (MLF). In current analyses, a Maximum Likelihood fit is among one of the most essential tools for parameter estimation in high energy physics, due to its many useful features [7]. For instance in its asymptotic limit, the Maximum Likelihood method is normally distributed around the true parameter value, with its variance being equal to the minimum variance bound [39]. Furthermore, the Maximum Likelihood method is an event-by-event based method that requires no binning, hence preventing any potential loss of information inherent to the binning, if the data suffers from low statistics [40]. Therefore, the MLF method enables the *simultaneous* extraction of *all* polarization observables $\{C_x,\, P,\, C_z\}$ for the $\gamma p \to K^0\Sigma^+$ reaction.

In order to apply a Maximum Likelihood fit, a *Likelihood function* is required. Let $\mathcal{P}(\{\vec{x}\}|\{\vec{\lambda}\})$ denote the *Probability Density Function* (PDF) of finding a set of measurements $\{\vec{x}\}$ for a set of events (i.e. the data), given a series of parameters $\{\vec{\lambda}\}$ that the PDF depends on. In addition, this PDF must satisfy the following normalization condition for the set of parameters $\{\vec{\lambda}\}$ [39],

$$\int \mathcal{P}(\{\vec{x}\}|\{\vec{\lambda}\})d\vec{x} = 1. \tag{4.53}$$

A PDF which fails to fulfill the condition above will yield either wrong or nonsensical results. Therefore, the Likelihood function is defined as the probability that a measured data set of interest will be obtained, provided a specific set of fit parameters is specified. Mathematically, this is characterized by the product of a series of N measurements of the probability density functions for each individual event,

$$\mathcal{L} = \mathcal{P}(\{\vec{x}\}|\{\vec{\lambda}\}) = \mathcal{P}(x_1|\{\vec{\lambda}\}) \cdot \mathcal{P}(x_2|\{\vec{\lambda}\}) \cdots \mathcal{P}(x_N|\{\vec{\lambda}\}) = \prod_{i=1}^{N} \mathcal{P}_i(x_i|\{\vec{\lambda}\}), \tag{4.54}$$

where the data set $\{\vec{x}\}$ has been split into subsets (bins), and N represents the total number of observed events for the given distribution. For the analysis at hand, the Likelihood function $\mathcal{L}$ defined by (4.54) furnishes the *probability* of obtaining the observed proton angular distributions from the $g12$ experiment, provided we have a specific set of parameters which maximizes the function $\mathcal{L}$. For this analysis, these parameters are defined as the set of single and double-polarization observables: $\{\vec{\lambda}\} \equiv \{C_x,\, P,\, C_z\}$.

Often times however, there is far too much data to provide an accurate calculation of the Likelihood function. When iterated over a large number of events N, the Likelihood function (4.54) tends to quickly grow towards larger values. Consequently, it is computationally simpler to deal with the negative natural logarithm of the Likelihood function, $-\ln \mathcal{L}$, than it is to deal with the Likelihood function $\mathcal{L}$ itself. Since the natural logarithm is a monotonically-increasing function, the minimization of $-\ln \mathcal{L}$ is far more convenient to work with, as opposed to the maximization of $\mathcal{L}$.

This minimization can be accomplished via the use of standard ROOT packages, such as MINUIT [28]. Therefore, the minimization of $-\ln\mathcal{L}$ is *equivalent* to the maximization of the Likelihood function $\mathcal{L}$. Additionally, it is a simpler task to find the derivative of a sum of terms than it is to find the derivative of a product of terms, which is needed to find the minimum of the Likelihood function. Thus, the negative log-Likelihood function is given by,

$$-\ln\mathcal{L} = -\sum_{i=1}^{N} \ln\mathcal{P}_i(x_i|\{\vec{\lambda}\}). \tag{4.55}$$

The Maximum Likelihood Estimator (MLE) for the parameters $\vec{\lambda}$ are those values which maximize the Likelihood function, or in the case of the log-Likelihood function, minimize. The MLE for a set of continuous N_P parameters $\{\vec{\lambda}\} = \{\lambda_1, \ldots, \lambda_{N_P}\}$, provided a set of N measurements constituting the observed data $\{\vec{x}\} = \{x_1, \ldots, x_N\}$, may be determined by solving the following set of simultaneous Maximum Likelihood minimization condition equations [7, 34],

$$\begin{aligned} \frac{\partial}{\partial\lambda_l}\ln\mathcal{L}(x_1,\ldots,x_N|\{\vec{\lambda}\})\bigg|_{\hat{\vec{\lambda}}} &= 0, \\ \sum_{i=1}^{N}\frac{\partial}{\partial\lambda_l}\ln\mathcal{P}(x_i|\{\vec{\lambda}\})\bigg|_{\hat{\vec{\lambda}}} &= 0. \end{aligned} \tag{4.56}$$

Solutions to the set of equations above (which hold $\forall l = 1, \ldots, N_P$) could also represent the minimum or inflection points of the Likelihood function. Minimizing the log-Likelihood function ($-\ln\mathcal{L}$) is what provides the set of parameters $\{\hat{\vec{\lambda}}\}$ for which the measured data set $\{\vec{x}\}$ becomes the *most likely*. In practice however, most Maximum Likelihood fits are far too complex to be analytically solved. Instead, one relies on numerical packages, the most common in high energy physics being MINUIT. Given a data set, this package minimizes a Likelihood function containing a single or multiple parameters and returns their optimal values, along with their uncertainties [28].

For Likelihood functions that depend on a set of multiple parameters $\{\vec{\lambda}\}$, the correlations between the parameters become important. In the absence of event-weights, these correlations are encapsulated by an $M \times M$ *covariance matrix* for a set of M parameters [7]. The covariance matrix, evaluated at the point $\vec{\lambda} = \hat{\vec{\lambda}}$ (which makes the measured data set $\{x_i\}$ the most likely), is defined as the inverse matrix of second-order derivatives (known as the *Hessian matrix*) of the negative logarithm of the Likelihood function [34],

$$V_{lj} = -\left(\frac{\partial^2}{\partial\lambda_l\partial\lambda_j}\ln\mathcal{L}(x_1,\ldots,x_N|\{\vec{\lambda}\})\bigg|_{\hat{\vec{\lambda}}}\right)^{-1} = -\left(\sum_{i=1}^{N}\frac{\partial^2}{\partial\lambda_l\partial\lambda_j}\ln\mathcal{P}(x_i|\{\vec{\lambda}\})\bigg|_{\hat{\vec{\lambda}}}\right)^{-1}. \tag{4.57}$$

The diagonal elements of the covariance matrix give the variance of the corresponding parameters, while the off-diagonal elements correspond to their covariance. Given a series of event-weights $w_{e=1,\ldots,N}$ for each measurement, the ML minimization condition takes on the following form,

$$\sum_{i=1}^{N} w_i \frac{\partial}{\partial \lambda_l} \ln \mathcal{P}(x_i|\{\vec{\lambda}\})\Bigg|_{\hat{\vec{\lambda}}} = 0. \tag{4.58}$$

However, the *weighted covariance matrix* for a weighted Maximum Likelihood function,

$$V_{lj} = -\left(\sum_{i=1}^{N} w_i \frac{\partial^2}{\partial \lambda_l \partial \lambda_j} \ln \mathcal{P}(x_i|\{\vec{\lambda}\})\Bigg|_{\hat{\vec{\lambda}}} \right)^{-1}, \tag{4.59}$$

will generally *fail* to yield asymptotically correct confidence intervals as the errors will scale proportionally to a factor of $(\sum_{i=1}^{N} w_i^2 / \sum_{i=1}^{N} w_i)$ [23, 34]. Assuming constant event-weights $w_i = w$, the minimization will either result in an over-estimation ($w > 1$) or an under-estimation ($w < 1$) of the sample's statistical power and shall yield confidence intervals that will either be under- or over-covered [34]. In the MLF analysis performed for this thesis, the event-weights w_i were given by the Q_i-values (see Section 3.6) for a series of i events. These Q_i-values predict the probability that the given event is indeed a $K^0\Sigma^+$ by subtracting off any background contributions to the Likelihood function.

In order to derive the asymptotically correct uncertainties, in the presence of event-based weights, we outline an approach that quantifies the parameter variance for a set of weights w_i. Let us then Taylor-expand the Maximum Likelihood condition (4.58), up to first-order, centered around the set of unknown true parameter values $\{\vec{\lambda_0}\}$ to which $\{\vec{\lambda}\}$ converges in the limit of large N. This expansion results in the following [34],

$$\sum_{i=1}^{N} w_i \frac{\partial}{\partial \lambda_l} \ln \mathcal{P}(x_i|\{\vec{\lambda}\})\Bigg|_{\vec{\lambda_0}} + \sum_{i=1}^{N} w_i \sum_{j=1}^{N_P} (\hat{\lambda}_j - \lambda_{0j}) \frac{\partial^2}{\partial \lambda_l \partial \lambda_j} \ln \mathcal{P}(x_i|\{\vec{\lambda}\})\Bigg|_{\vec{\lambda_0}} = 0. \tag{4.60}$$

Re-expressing expression (4.60) via the use of explicit matrix notation, we have,

$$\begin{pmatrix} \sum_{i=1}^{N} w_i \frac{\partial \ln \mathcal{P}(x_i|\{\vec{\lambda}\})}{\partial \lambda_1}\Big|_{\vec{\lambda_0}} \\ \vdots \\ \sum_{i=1}^{N} w_i \frac{\partial \ln \mathcal{P}(x_i|\{\vec{\lambda}\})}{\partial \lambda_{N_P}}\Big|_{\vec{\lambda_0}} \end{pmatrix} = - \begin{pmatrix} \sum_{i=1}^{N} w_i \frac{\partial^2 \ln \mathcal{P}(x_i|\{\vec{\lambda}\})}{\partial \lambda_1^2}\Big|_{\vec{\lambda_0}} & \cdots & \sum_{i=1}^{N} w_i \frac{\partial^2 \ln \mathcal{P}(x_i|\{\vec{\lambda}\})}{\partial \lambda_1 \partial \lambda_{N_P}}\Big|_{\vec{\lambda_0}} \\ \vdots & \ddots & \vdots \\ \sum_{i=1}^{N} w_i \frac{\partial^2 \ln \mathcal{P}(x_i|\{\vec{\lambda}\})}{\partial \lambda_{N_P} \partial \lambda_1}\Big|_{\vec{\lambda_0}} & \cdots & \sum_{i=1}^{N} w_i \frac{\partial^2 \ln \mathcal{P}(x_i|\{\vec{\lambda}\})}{\partial \lambda_{N_P}^2}\Big|_{\vec{\lambda_0}} \end{pmatrix} \times \begin{pmatrix} \hat{\lambda}_1 - \lambda_{01} \\ \vdots \\ \hat{\lambda}_{N_P} - \lambda_{0N_P} \end{pmatrix}. \tag{4.61}$$

Taking the inverse of matrix (4.61), we find that the deviation of the estimator parameters $\hat{\lambda}_j$ from their actual values λ_{0j} is given by the following set of equations,

$$\begin{aligned}\begin{pmatrix}\hat{\lambda}_1-\lambda_{01}\\ \vdots \\ \hat{\lambda}_{N_P}-\lambda_{0N_P}\end{pmatrix} = &-\begin{pmatrix} \sum_{i=1}^N w_i \frac{\partial^2 \ln\mathcal{P}(x_i|\{\vec{\lambda}\})}{\partial\lambda_1^2}\Big|_{\vec{\lambda}_0} & \cdots & \sum_{i=1}^N w_i \frac{\partial^2 \ln\mathcal{P}(x_i|\{\vec{\lambda}\})}{\partial\lambda_1\partial\lambda_{N_P}}\Big|_{\vec{\lambda}_0} \\ \vdots & \ddots & \vdots \\ \sum_{i=1}^N w_i \frac{\partial^2 \ln\mathcal{P}(x_i|\{\vec{\lambda}\})}{\partial\lambda_{N_P}\partial\lambda_1}\Big|_{\vec{\lambda}_0} & \cdots & \sum_{i=1}^N w_i \frac{\partial^2 \ln\mathcal{P}(x_i|\{\vec{\lambda}\})}{\partial\lambda_{N_P}^2}\Big|_{\vec{\lambda}_0}\end{pmatrix}^{-1} \\ &\times \begin{pmatrix}\sum_{i=1}^N w_i \frac{\partial \ln\mathcal{P}(x_i|\{\vec{\lambda}\})}{\partial\lambda_1}\Big|_{\vec{\lambda}_0} \\ \vdots \\ \sum_{i=1}^N w_i \frac{\partial \ln\mathcal{P}(x_i|\{\vec{\lambda}\})}{\partial\lambda_{N_P}}\Big|_{\vec{\lambda}_0}\end{pmatrix}.\end{aligned} \tag{4.62}$$

Therefore the variance of the covariance matrix, in the asymptotic limit with weights w_i, is [34],

$$\begin{aligned} V_{lj} &= \left\langle \left(\hat{\lambda}_l-\lambda_{0l}\right)\left(\hat{\lambda}_j-\lambda_{0j}\right)\right\rangle = V_{lk}C_{km}^{-1}V_{mj} \\ &= \left(\sum_{i=1}^N w_i \frac{\partial^2 \ln\mathcal{P}(x_i|\{\vec{\lambda}\})}{\partial\lambda_l\partial\lambda_k}\Big|_{\hat{\vec{\lambda}}}\right)^{-1} \times \left(\sum_{i=1}^N w_i^2 \frac{\partial^2 \ln\mathcal{P}(x_i|\{\vec{\lambda}\})}{\partial\lambda_k\partial\lambda_m}\Big|_{\hat{\vec{\lambda}}}\right) \\ &\times \left(\sum_{i=1}^N w_i \frac{\partial^2 \ln\mathcal{P}(x_i|\{\vec{\lambda}\})}{\partial\lambda_m\partial\lambda_j}\Big|_{\hat{\vec{\lambda}}}\right)^{-1}, \end{aligned} \tag{4.63}$$

where $V_{lk(mj)}$ is the weighted covariance matrix (4.59) and C_{km} is the inverse of the Hessian matrix, with squared event-weights w_i^2. Explicitly, the correctly weighted covariance matrix (4.63) is thus,

$$\begin{aligned} V_{lj} = &\begin{pmatrix} \sum_{i=1}^N w_i \frac{\partial^2 \ln\mathcal{P}(x_i|\{\vec{\lambda}\})}{\partial\lambda_1^2}\Big|_{\hat{\vec{\lambda}}} & \cdots & \sum_{i=1}^N w_i \frac{\partial^2 \ln\mathcal{P}(x_i|\{\vec{\lambda}\})}{\partial\lambda_1\partial\lambda_{N_P}}\Big|_{\hat{\vec{\lambda}}} \\ \vdots & \ddots & \vdots \\ \sum_{i=1}^N w_i \frac{\partial^2 \ln\mathcal{P}(x_i|\{\vec{\lambda}\})}{\partial\lambda_{N_P}\partial\lambda_1}\Big|_{\hat{\vec{\lambda}}} & \cdots & \sum_{i=1}^N w_i \frac{\partial^2 \ln\mathcal{P}(x_i|\{\vec{\lambda}\})}{\partial\lambda_{N_P}^2}\Big|_{\hat{\vec{\lambda}}}\end{pmatrix}^{-1} \\ &\times \begin{pmatrix} \sum_{i=1}^N w_i^2 \left[\frac{\partial \ln\mathcal{P}(x_i|\{\vec{\lambda}\})}{\partial\lambda_1}\Big|_{\hat{\vec{\lambda}}}\right]^2 & \cdots & \sum_{i=1}^N w_i^2 \left[\frac{\partial \ln\mathcal{P}(x_i|\{\vec{\lambda}\})}{\partial\lambda_1}\Big|_{\hat{\vec{\lambda}}}\right]\left[\frac{\partial \ln\mathcal{P}(x_i|\{\vec{\lambda}\})}{\partial\lambda_{N_P}}\Big|_{\hat{\vec{\lambda}}}\right] \\ \vdots & \ddots & \vdots \\ \sum_{i=1}^N w_i^2 \left[\frac{\partial \ln\mathcal{P}(x_i|\{\vec{\lambda}\})}{\partial\lambda_{N_P}}\Big|_{\hat{\vec{\lambda}}}\right]\left[\frac{\partial \ln\mathcal{P}(x_i|\{\vec{\lambda}\})}{\partial\lambda_1}\Big|_{\hat{\vec{\lambda}}}\right] & \cdots & \sum_{i=1}^N w_i^2 \left[\frac{\partial \ln\mathcal{P}(x_i|\{\vec{\lambda}\})}{\partial\lambda_{N_P}}\Big|_{\hat{\vec{\lambda}}}\right]^2 \end{pmatrix} \\ &\times \begin{pmatrix} \sum_{i=1}^N w_i \frac{\partial^2 \ln\mathcal{P}(x_i|\{\vec{\lambda}\})}{\partial\lambda_1^2}\Big|_{\hat{\vec{\lambda}}} & \cdots & \sum_{i=1}^N w_i \frac{\partial^2 \ln\mathcal{P}(x_i|\{\vec{\lambda}\})}{\partial\lambda_1\partial\lambda_{N_P}}\Big|_{\hat{\vec{\lambda}}} \\ \vdots & \ddots & \vdots \\ \sum_{i=1}^N w_i \frac{\partial^2 \ln\mathcal{P}(x_i|\{\vec{\lambda}\})}{\partial\lambda_{N_P}\partial\lambda_1}\Big|_{\hat{\vec{\lambda}}} & \cdots & \sum_{i=1}^N w_i \frac{\partial^2 \ln\mathcal{P}(x_i|\{\vec{\lambda}\})}{\partial\lambda_{N_P}^2}\Big|_{\hat{\vec{\lambda}}}\end{pmatrix}^{-1}. \end{aligned} \tag{4.64}$$

Trivially, one can verify that if the event-weights are all unity, $w_i = 1$ (or if they all take the form of some constant $w_i = w$), then the corrected weighted covariance matrix (4.63) reduces to,

$$V_{lj} = \left(\sum_{i=1}^{N} \frac{\partial^2 \ln \mathcal{P}(x_i|\{\vec{\lambda}\})}{\partial \lambda_l \partial \lambda_j} \bigg|_{\hat{\vec{\lambda}}} \right)^{-1}, \tag{4.65}$$

which is just the covariance matrix with of no event-weights (4.57). Although this approach yields the asymptotically correct uncertainties using event-weights w_i, it might be impractical in its implementation. A more expedient method than the one highlighted previously is to simply re-scale the weights within a Likelihood function by the ratio of the sum of the weights w_i over the sum of the squared weights w_i^2. This defines a new set of scaled-weights $w_i^{'}$ given by [34],

$$w_i^{'} = w_i \cdot \frac{\sum_{i=1}^{N} w_i}{\sum_{i=1}^{N} w_i^2} = w_i \alpha_w, \tag{4.66}$$

where we defined the following parameter of interest to a Maximum Likelihood analysis [23, 58],

$$\alpha_w \equiv \frac{\sum_{i=1}^{N} w_i}{\sum_{i=1}^{N} w_i^2}. \tag{4.67}$$

Replacing all the event-weights w_i in (4.59) by the event-weights $w_i^{'}$ will re-scale all weights so that the total statistical power of the data matches that of an N-number of events. However, generally speaking, this won't reproduce the result shown in equation (4.64) [34]. Nonetheless, many current analyses include this extra α_w factor to better account for the effects that the background subtraction method has on the uncertainties obtained via the MLF method [58].

For the particular analysis at hand, the objective was to perform a simultaneous extraction of the polarization observables $\{\vec{\lambda}\} = \{C_x,\, P,\, C_z\}$ for each $(\cos\theta^{\Sigma^+}_{\text{c.m.}},\, E_\gamma)$ bin that maximized the Likelihood function $\mathcal{L}$ modeling the physics of our reaction. The Unbinned Maximum Likelihood event-based fit is an extreme case of a binned method for which each bin is reduced until it contains either one or zero event(s) [40]. To define the Likelihood function for our reaction, a probability density function was, naturally, required. The PDF for observing *each individual event* in an experiment is defined as a function of the *fit parameters* of interest to an analysis. For this analysis, these parameters included the cosines of the proton scattering angles in the Σ^+ rest-frame (with respect to the scattering-plane axes), the photon's circular polarization $P_\odot$ and the set of observables $\{C_x,\, P,\, C_z\}$. The PDF for a particular given event i is thus defined by [2, 8, 24],

$$\mathcal{P}_i^{\pm}(\cos\theta^p_{x,i}, \cos\theta^p_{y,i}, \cos\theta^p_{z,i}|C_x, P, C_z) = 1 \pm \alpha P_\odot (C_x \cos\theta^p_{x,i} + C_z \cos\theta^p_{z,i}) + \alpha P \cos\theta^p_{y,i}, \tag{4.68}$$

where the ± denotes the helicity state of the incoming photon beam. Each event involved in this analysis was assigned an event-weight w_i, computed via the $Q-$factor method (see Section 3.6). Thus, the Likelihood function for N_{total} events, along with its negative natural log, is given by,

$$\begin{aligned}\mathcal{L} &= \prod_{i=1}^{N_{\text{total}}} [\mathcal{P}_i^{\pm}(x_i|\{\vec{\lambda}\})]^{Q_i}, \\ -\ln\mathcal{L} &= -\sum_{i=1}^{N_{\text{total}}} Q_i \ln\mathcal{P}_i^{\pm}(x_i|\{\vec{\lambda}\}).\end{aligned} \tag{4.69}$$

However, generally speaking expression (4.69) won't lead to a correct estimation of the uncertainties of the most likely parameters (i.e. the polarization observables) that maximize the Likelihood function $\mathcal{L}$, in accordance to the constraint outlined by (4.56). In order to accurately approximate the uncertainties obtained via the MLF, the addition of an the extra parameter α_Q (4.67), becomes necessary to define the logarithmic-Likelihood function,

$$-\ln\mathcal{L} = -\alpha_Q \sum_{i=1}^{N_{\text{total}}} Q_i \ln\mathcal{P}_i^{\pm}(x_i|\{\vec{\lambda}\}), \tag{4.70}$$

where α_Q accounts for the effect of the background subtraction (from the $Q-$values) on the statistical uncertainty of the parameters obtained via the minimization of (4.70). Lack of this α_Q term would otherwise over (or alternatively, under) estimate the values of the parameters' uncertainties.

The total number of events N_{total} in our analysis was divided into two sets of events representing the total number of positive (N^+) and negative (N^-) helicity states stemming from the incoming photon beam. Therefore, the total log-Likelihood function, written explicitly in terms of the full PDF (4.68), is given by the sum of all log-Likelihood functions for every individual event i,

$$\begin{aligned}-\ln\mathcal{L} = &-\alpha_Q \sum_{i=1}^{N^+} Q_i \ln(1 + \alpha P_{\odot}(C_x \cos\theta_{x,i}^p + C_z \cos\theta_{z,i}^p) + \alpha P \cos\theta_{y,i}^p) \\ &-\alpha_Q \sum_{i=1}^{N^-} Q_i \ln(1 - \alpha P_{\odot}(C_x \cos\theta_{x,i}^p + C_z \cos\theta_{z,i}^p) + \alpha P \cos\theta_{y,i}^p),\end{aligned} \tag{4.71}$$

where Q_i represents the $Q-$value for each event i, with a fixed helicity state. Expression (4.71) saw extensive use in our analysis as it is exclusively a function of the observables set of interest to this analysis, namely $\{C_x,\, P,\, C_z\}$. Minimizing (4.71) with the CERNLIB package MINUIT, using the minimization algorithm MIGRAD, we found the most likely observable values given the $g12$ data set $\{\cos\theta_x^p,\, \cos\theta_y^p,\, \cos\theta_z^p\}$ (i.e. a proton angular distribution in the hyperon's (Σ^+) rest-frame). These results are discussed further in Chapter 5.

CHAPTER 5

SYSTEMATIC UNCERTAINTIES & FINAL RESULTS

The overall uncertainties pertaining to the set of polarization observables $\{C_x,\ P,\ C_z\}$ have two different contributing factors: *statistical* and *systematic uncertainties.* On the one hand, statistical uncertainties stem from any set of measurements based on the total number of counts for each kinematic bin (see Sub-section 4.3.1). On the other hand, systematic uncertainties are inherent to any given experiment; these uncertainties originate from multiple sources, including (but not limited to): detector acceptances, detector resolution, background contributions, among others. Great care must be taken in order to separate the contributing factors to the uncertainties stemming from statistical and systematic errors.

However, due to lack of time, it became unfeasible to carry out the appropriate systematic uncertainties pertaining to this analysis. Instead, this Section will serve as a guideline for the systematics that could in principle be studied for the photoproduction reaction $\gamma p \to K^0\Sigma^+$, and their individual contributions to the analysis. For a more throughout study of these systematics, see References [3, 55]. Furthermore, this Section will discuss the acceptance corrections and results obtained from this analysis, i.e. the set of observables $\{C_x,\ P,\ C_z\}$, as they were extracted from the isospin channel $K^0\Sigma^+$, via the application of the linear and Maximum Likelihood fit methods.

5.1 Systematic Uncertainties in the $g12$ Analysis

5.1.1 Systematics from the $Q-$Factor Method

The $Q-$factor method, employed to subtract off any interfering background effects, naturally contributed to the systematic uncertainties. The assignment of a $Q-$factor to an event required a fit of the event's mass distributions, and those of its neighboring events, via the application of the MLF technique [3]. Consequently, the uncertainty of the $Q-$value for said event is given by,

$$\sigma_Q^2 = \sum_{i,j} \frac{\partial Q}{\partial \eta_i}(C_\eta^{-1})\frac{\partial Q}{\partial \eta_j}, \tag{5.1}$$

where C_η denotes the covariance matrix for the set of fit parameters $\vec{\eta}$. Furthermore, the $Q-$factor method could also lead to a series of systematic "correlations" between the events and their nearest neighbors [3]. For instance, consider the *counting* experiment used to find the induced hyperon polarization observable P from the proton angular distribution of the Σ^+ (4.53),

$$P = \frac{2}{\alpha} \cdot \left[\frac{N_\mathrm{U} - N_\mathrm{D}}{N_\mathrm{U} + N_\mathrm{D}}\right] = \frac{2A}{\alpha},$$

where A denotes the counting asymmetry, while N_U and N_D represent the total number of events with protons above and below the scattering plane, respectively. Any uncertainty originating from the $Q-$factor for each event exclusively affected the number of counts, and not the weak decay parameter α. Therefore, the systematic correlation uncertainty stemming from the number of counts within a bin, due to the $Q-$factor, is given by,

$$\sigma_N^2 = \sum_{i,j} \sigma_Q^i \rho_{ij} \sigma_Q^j, \tag{5.2}$$

where N denotes the total number of events, σ_Q^i represents the fit error in the $Q-$value for the i^th event, and ρ_{ij} constitutes the correlation between the i^th and j^th events (this is equal to a fraction of the number of common nearest neighbors to the event) [3]. Often times, it is computationally convenient to work under the assumption that all given events are 100% correlated, thus overestimating the uncertainties and avoiding the calculation of the ρ_{ij} correlations [3].

Emulating the calculation from Sub-section 4.3.1, and writing the P observable as a function of the number of counts, $P = f(N_\mathrm{U}, N_\mathrm{D})$, standard error propagation dictates that,

$$\begin{aligned} \sigma_P &= \sqrt{\left(\frac{\partial f}{\partial N_\mathrm{U}}\right)^2 \sigma_{N_\mathrm{U}}^2 + \left(\frac{\partial f}{\partial N_\mathrm{D}}\right)^2 \sigma_{N_\mathrm{D}}^2} \\ &= \frac{4}{\alpha(N_\mathrm{U} + N_\mathrm{D})^2} \cdot \sqrt{N_\mathrm{D}^2 \sigma_{N_\mathrm{U}}^2 + N_\mathrm{U}^2 \sigma_{N_\mathrm{D}}^2}. \end{aligned} \tag{5.3}$$

However, if $\sigma_{N_\mathrm{U}} = \sigma_{N_\mathrm{D}} = \sigma_N$, then we may simplify (5.3) as follows,

$$\sigma_P = \frac{4\sigma_N}{\alpha(N_\mathrm{U} + N_\mathrm{D})^2} \cdot \sqrt{N_\mathrm{U}^2 + N_\mathrm{D}^2}. \tag{5.4}$$

Consequently, it follows that we can use expression (5.2) in order to find σ_{N_U} and σ_{N_D}, which can then be inserted into (5.3) to find the systematic uncertainty from the $Q-$values on the P observable, i.e. σ_P [3].

5.1.2 Systematics from the Confidence Level (CL) Cut

A further source contributing to the total systematic uncertainties stems from the confidence level (CL) cut. To determine the uncertainty accrued by this cut, the nominal CL cut for the event statistics of the reaction needs to be recalculated. Denoting the originally measured value for an asymmetry with a given kinematic bin as A_o, and a newly measured value based with the newly applied CL cut as A_n, we can quantify the absolute uncertainty as follows [3],

$$\sigma_{\mathrm{CL}} = \frac{|A_n - A_o|}{A_o}. \tag{5.5}$$

5.1.3 Systematic Uncertainties in the Determination of Polarization Observables

Let us consider Taylor expanding the Likelihood function $-\ln\mathcal{L}(\alpha)$ around its best parameter estimator $\alpha = \hat{\alpha}$, where $\hat{\alpha}$ denotes the best-fit parameter that minimizes $-\ln\mathcal{L}(\alpha)$ [3, 39],

$$-\ln\mathcal{L}(\alpha) = -\ln\mathcal{L}(\hat{\alpha}) - \frac{1}{2}(\alpha-\hat{\alpha})^2 \frac{d^2\ln\mathcal{L}}{d\alpha^2}\bigg|_{\alpha=\hat{\alpha}} - \cdots . \tag{5.6}$$

From the above, it follows that we can write the log-Likelihood function $-\ln\mathcal{L}$ as follows,

$$-\ln\mathcal{L} \approx \text{const}\cdot e^{-\frac{1}{2}\left\{(\alpha-\hat{\alpha})^2\frac{d^2\ln\mathcal{L}}{d\alpha^2}\right\}}\Big|_{\alpha=\hat{\alpha}}, \tag{5.7}$$

such that the statistical uncertainty (variance) placed by the Likelihood function on a measurement is given by,

$$\sigma_\alpha^2 = \left(\frac{d^2\ln\mathcal{L}}{d\alpha^2}\bigg|_{\alpha=\hat{\alpha}}\right)^{-1}. \tag{5.8}$$

Therefore, it follows that $-\ln\mathcal{L}$ is approximately Gaussian, with σ_α being the statistical uncertainty provided by MINUIT [3, 28]. Equivalently however, it is common practice [28, 58] to multiply the log-Likelihood $-\ln\mathcal{L}$ by a factor of two, so as to make it coincide with the *method of least squares* (χ^2-distribution) [28, 61]. Hence, the interpretation of the ensuing deviation (uncertainty) is approximately that of the sum of the squares in a least-square regression study [3, 61]. Hence, the function to be minimized is rather $-2\ln\mathcal{L}$, with a statistical uncertainty given by,

$$\sigma_\alpha^2 = \frac{1}{2}\left(\frac{d^2\ln\mathcal{L}}{d\alpha^2}\bigg|_{\alpha=\hat{\alpha}}\right)^{-1}. \tag{5.9}$$

Adhering to a procedure from a previous analysis, which used the same $g12$ data as this thesis [3], the systematic uncertainties for the observables could be taken as the propagated $Q-$value uncertainties. Thus, this applies the following variation performed on the $Q-$values [3]: $Q - \sigma_Q < Q < Q + \sigma_Q$, where σ_Q represent the uncertainties of Q. Representing the original measured value for a given observable by A_o and the newly obtained observable values (determined by the variation on Q) by A_n, we find that the uncertainty can be calculated using,

$$\sigma_{\text{obs.}} = \frac{|A_n - A_o|}{A_o}. \tag{5.10}$$

5.1.4 Systematics Arising from the Photon Polarization $P_\odot$ and Weak Decay Asymmetry Parameter α

Let us recall that each observable from the set $\{C_x, P, C_z\}$, has a direct dependence on some externally determined parameters. On one hand, the double-polarization observables C_x and C_z depend on both the weak decay asymmetry parameter α, and the degree of photon polarization $P_\odot$. On the other hand, the hyperon-recoil polarization P depends exclusively on α. Clearly, this leads us to conclude that the systematic uncertainties for C_x and C_z derive from both α and $P_\odot$, while the uncertainty from P comes from α alone [2]. We briefly describe these systematics below.

Systematic Uncertainty from the Weak Decay α. From the asymmetry in equation (4.43), we find that the uncertainty in the double-polarization observables C_x and C_z, due to the uncertainty in the decay parameter α ($\delta\alpha = 0.016$ [59]), follows from standard error propagation,

$$\delta_\alpha(C_i) = \left| \delta\alpha \cdot \frac{1}{\alpha P_\odot \cos\theta_i^p} \cdot \frac{\partial A(\cos\theta_i^p)}{\partial\alpha} \right| = \left| C_i \cdot \frac{\delta\alpha}{\alpha} \right| = 0.0163|C_i|, \tag{5.11}$$

resulting in a relative 1.63% error. Similarly for the P observable, expression (4.52) yields,

$$\delta_\alpha(P) = \left| P \cdot \frac{\delta\alpha}{\alpha} \right| = 0.0163|P|. \tag{5.12}$$

Systematic Uncertainty from Photon Polarization $P_\odot$. Working under the assumption that the electron and photon energies present in expression (3.10) were accurately measured, the uncertainty inherent to the photon polarization $P_\odot$ stems solely from the electron polarization P_{elec}. From Table 3.2, it can be observed that the average uncertainty on the electron beam polarization P_{elec} from different runs is approximately ≈ 1.4%. Employing the same error propagation methods as before, and using an average beam polarization $P_\odot$, we find,

$$\delta_{P_\odot}(C_i) = \left| C_i \cdot \frac{\delta P_\odot}{P_\odot} \right| = 0.05|C_i|, \tag{5.13}$$

resulting in a relative systematic error of 5% for the double-polarization observables C_x and C_z.

5.2 Results for the $\gamma p \rightarrow K^0\Sigma^+$ Reaction

The following Sub-sections discuss acceptance corrections, and our final results found for the set of polarization observables $\{C_x,\, P,\, C_z\}$, for the photoproduction reaction $\gamma p \rightarrow K^0\Sigma^+$.

5.2.1 Acceptance Corrections and Monte Carlo (MC) Simulations

An important element involved in the extraction of observables relies on a series of corrections accounting for any detector effects on the analysis data. Consider a set of $N_{\rm e}$ events that hit a region of the detector, with only $N_{\rm m}$ events ($N_{\rm m} < N_{\rm e}$) actually being measured. Consequently, it becomes necessary to account for such discrepancies from the measured yields.

To apply these corrections, the CLAS detector needs to be modeled and fed randomly generated events to determine the appropriate acceptance correction factor. The acceptance for the photoproduction reaction $\gamma p \rightarrow K^0\Sigma^+$ was thus determined by producing evenly distributed *Generated Monte Carlo* events (these represent all events that can happen [20]) across their available flat phase-space, with equally distributed kinematic properties [38]. The detector performance was modeled using GEANT3-based Monte Carlo studies. A set of forty million $\gamma p \rightarrow K^0\Sigma^+$ events were generated via the use of the genr8 program, making no reference to CLAS properties, and were subsequently processed through the GSIM and GPP packages to simulate detector effects [3, 38].

Afterwards, any surviving generated MC events were subsequently analyzed using the same reconstruction and selection criteria applied to the measured data events (Section 3). This resulted in a set of *Reconstructed Monte Carlo* events [57] (which represent all detected events [20]). Since every MC event is a $K^0_S\Sigma^+$ signal event ($Q = 1$), the $Q-$values for each MC event need not be determined [38]. Therefore, the detector acceptance correction for each kinematic bin was defined as the ratio of the yield for Reconstructed to Generated MC events [57],

$$A\big(E_\gamma, \cos\theta^{\Sigma^+}_{\rm c.m.}\big)_{\gamma p \rightarrow K^0\Sigma^+} = \frac{N(E_\gamma, \cos\theta^{\Sigma^+}_{\rm c.m.})_{\rm rec\ MC}}{N(E_\gamma, \cos\theta^{\Sigma^+}_{\rm c.m.})_{\rm gen\ MC}}. \tag{5.14}$$

Expression (5.14) may be interpreted as the likelihood that if an event happens, it is indeed detected and survives through the analysis chain. Hence, while a detector only measures $N(E_\gamma, \cos\theta^{\Sigma^+}_{\rm c.m.})_{\rm data}$ events, in actuality there were $N(E_\gamma, \cos\theta^{\Sigma^+}_{\rm c.m.})_{\rm data}/A\big(E_\gamma, \cos\theta^{\Sigma^+}_{\rm c.m.}\big)_{\gamma p \rightarrow K^0\Sigma^+}$ events. The acceptance correction (5.14) accounts for events which exist, but were undetected. Figures 5.1, 5.3 and 5.5 display the C_x, C_z and P observables, with and without acceptance corrections, while Figures 5.2, 5.4 and 5.6 display their ratio.

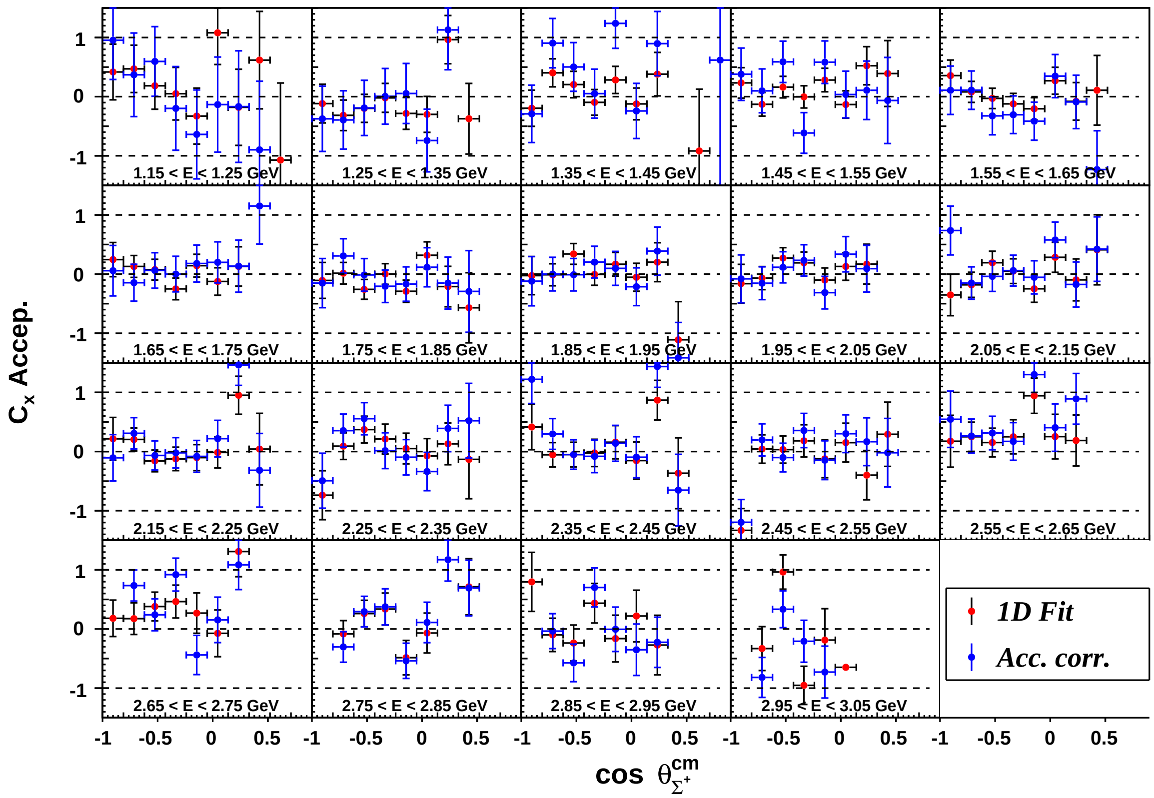

Figure 5.1: Double beam-recoil observable C_x vs. $\cos\theta^{\Sigma^+}_{\text{c.m.}}$ binned in energy, with a range of $1.15 < E_\gamma < 3.05$ GeV. Red dots represent the extracted C_x observable via a linear fit to the asymmetry in (4.43), while the blue dots represent the acceptance corrections performed on C_x (5.14). The acceptance $A_{\gamma p \to K^0\Sigma^+}$ for C_x appears to have an effect across most of the lower energy bins, over their backward and forward angular regions, with some minor effects in the high energy bins. The given uncertainties for the red-dots are statistical with the $Q-$value uncertainties added in quadrature, while the blue dots uncertainties are statistical in nature.

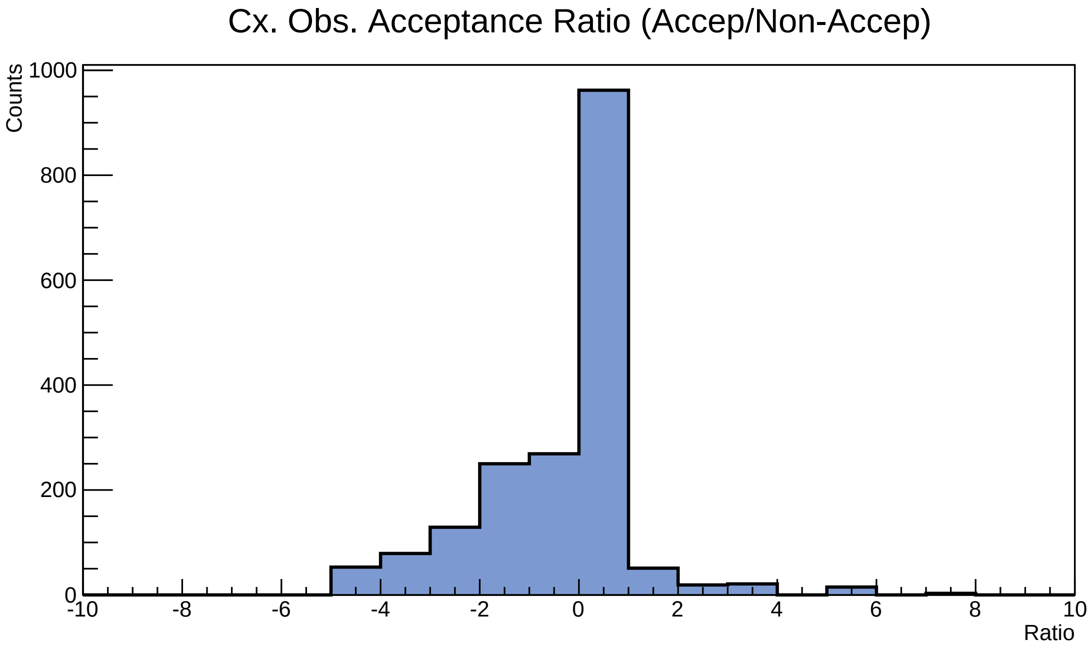

Figure 5.2: Ratio of the histograms with and without the implemented acceptance corrections (see Figure 5.1) $A_{\gamma p \to K^0 \Sigma^+}$, for the beam-recoil polarization observable C_x. The histogram is approximately Gaussian and roughly centered around 1.0, with a lower left-most tail. Consequently, the acceptance corrections play a greater, however slight, role for the C_x observable, than for the other observables considered in this analysis; see Figures 5.4 and 5.6

.

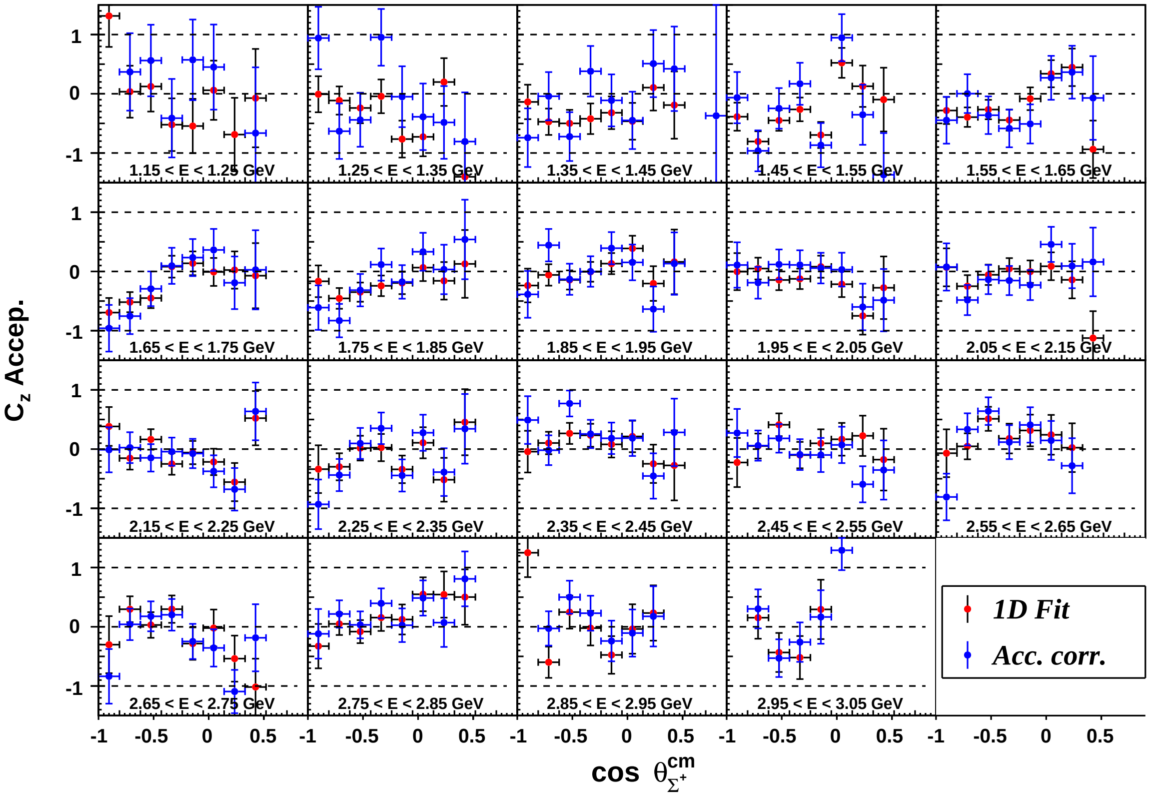

Figure 5.3: Double beam-recoil observable C_z vs. $\cos\theta^{\Sigma^+}_{\mathrm{c.m.}}$ binned in energy, with a range of $1.15 < E_\gamma < 3.05$ GeV. Red dots represent the extracted C_z observable via a linear fit to (4.43), while the blue dots represent the acceptance corrections performed on C_z (5.14). Similar to Figure (5.1), the acceptance $A_{\gamma p \to K^0\Sigma^+}$ for C_z appears to play a role across most of the lower energy bins, over their backward/forward angular regions, with some minor effects for the higher energy bins. The given uncertainties for the red-dots are statistical with the $Q-$value uncertainties added in quadrature, while the blue dots uncertainties are statistical in nature.

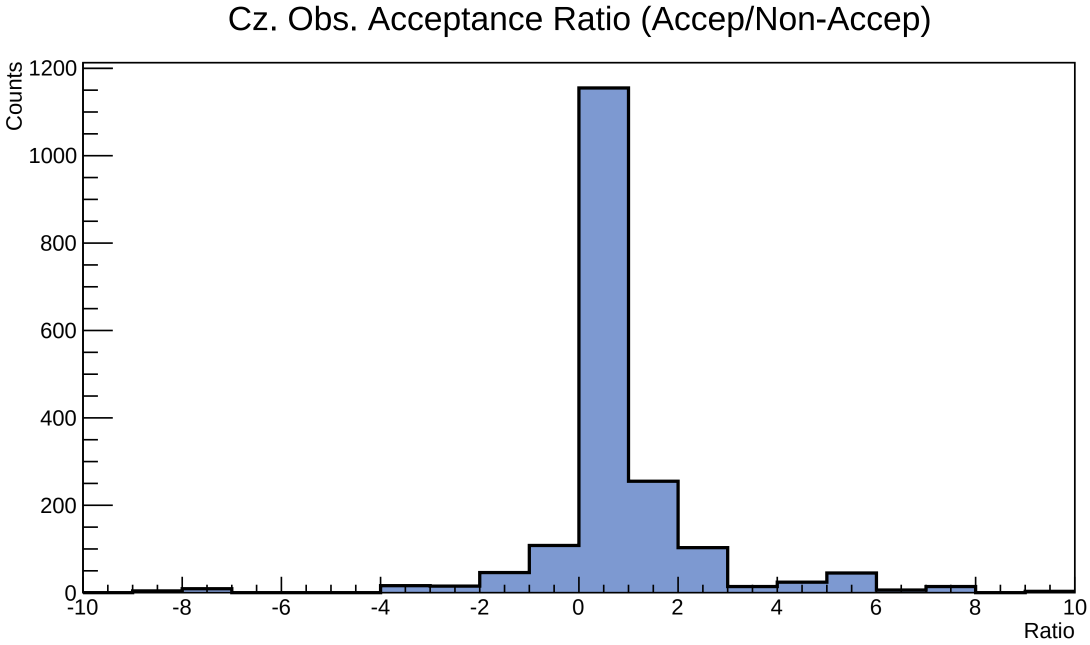

Figure 5.4: Ratio of the histograms with and without the implemented acceptance corrections (see Figure 5.1) $A_{\gamma p \to K^0 \Sigma^+}$ for the beam-recoil polarization observable C_z. The histogram is approximately Gaussian and centered around 1.0, thus indicating that the acceptance corrections have little influence on the C_z observable.

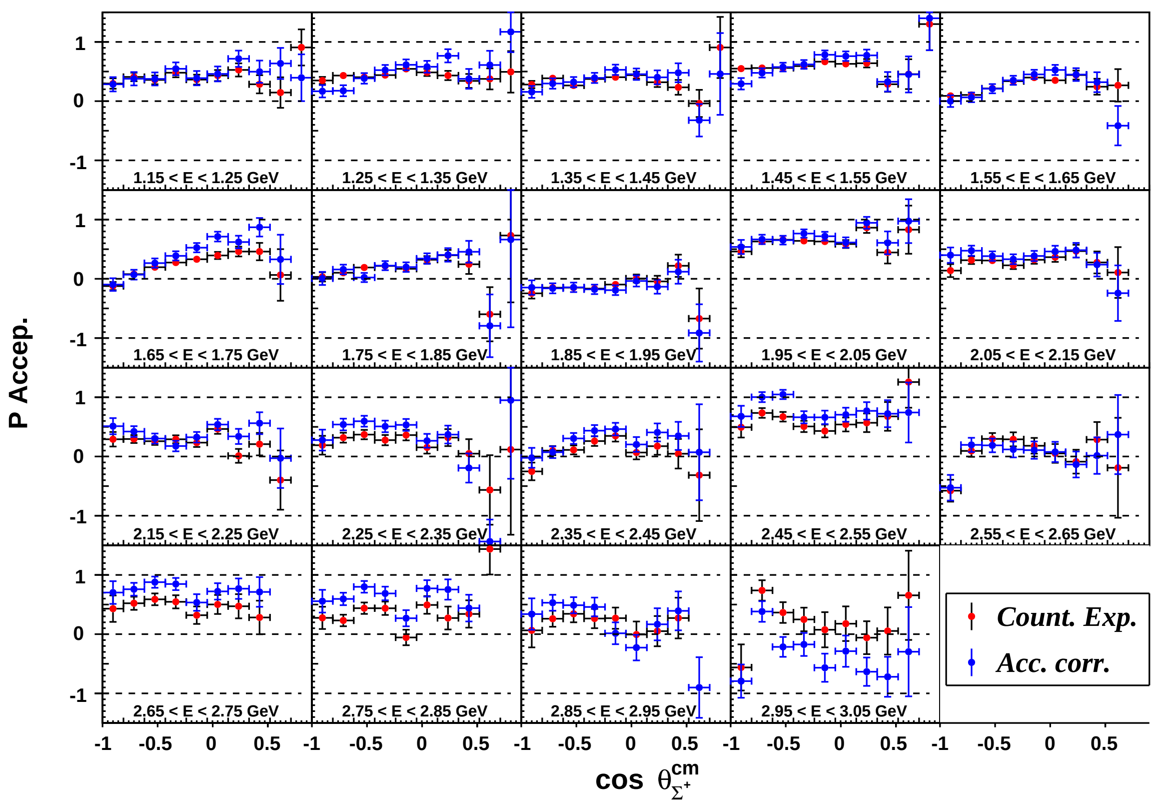

Figure 5.5: Single hyperon-recoil observable P vs. $\cos\theta^{\Sigma^+}_{\text{c.m.}}$ binned in energy, with a range of $1.15 < E_\gamma < 3.05$ GeV. Red dots represent the extracted P observable via a the use of the counting asymmetry in (4.52), while the blue dots denote the acceptance corrections performed on P (5.14). We find good agreement between both measurements before and after acceptance corrections were applied, across most of energy bins. Some minor discrepancies (i.e. shifts between the extracted P observable values) are found in the higher energy bins, which could be attributed to the underlying statistics of the data. As such, the acceptance corrections do not play a considerable role for the P observable. The given uncertainties for the red-dots are statistical with the $Q-$value uncertainties added in quadrature, while the blue dots uncertainties are statistical in nature.

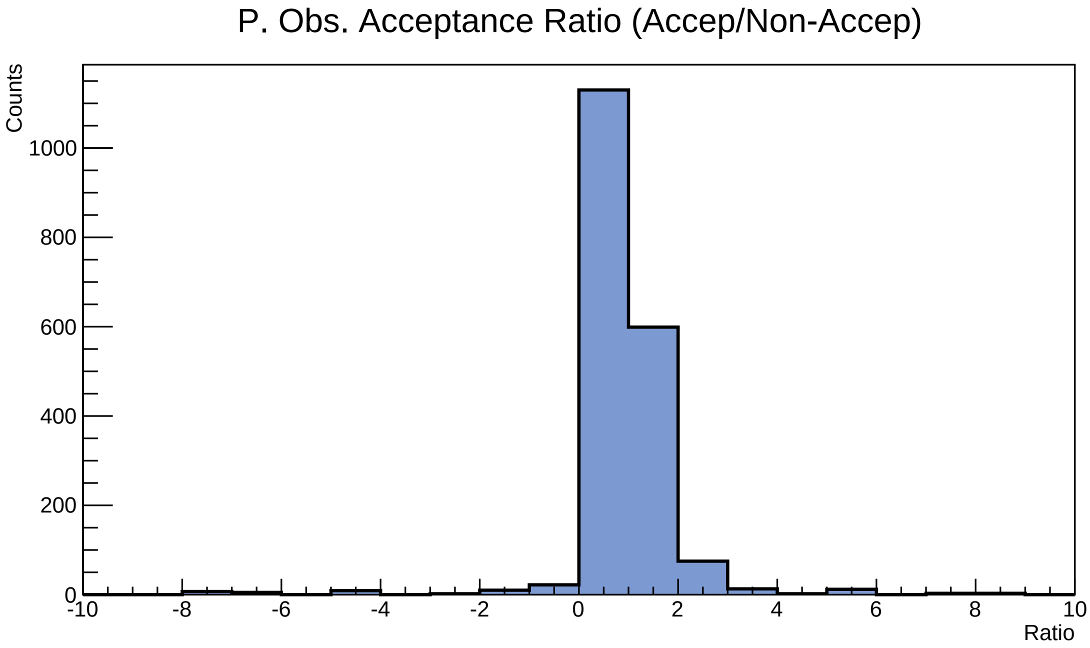

Figure 5.6: Ratio of the histograms with and without implemented acceptance corrections (see Figure 5.1) $A_{\gamma p \to K^0 \Sigma^+}$ for the hyperon-recoil polarization observable P. The histogram is roughly centered around 1.0, thus indicating that the acceptance corrections have little influence on the P observable.

5.2.2 The Double-Polarization Observables C_x and C_z

The photoproduction of charged Kaons, such as in the reaction $\gamma p \to K^0\Sigma^+$, has undergone extensive investigation in recent years at CLAS. Nonetheless, the K^0 channel has been mostly ignored, with no apparent justification. The photoproduction of neutral Kaons (K^0) offers a clear advantage over the production of charged ones ($K^{\pm}$) since photons cannot couple to the (vanishing) charge of the K^0 meson. Furthermore, in order to disentangle contributions stemming from N^* and Δ^* resonances it is necessary to have data on the isospin-related $K^0(d\bar{s})\Sigma^+(uus)$ and $K^+(u\bar{s})\Sigma^0(uds)$ channels. The helicity dependent beam-recoil polarization observables C_x and C_z were extracted using both the linear and the Maximum Likelihood fits. Figures 5.7 and 5.8 display the comparison between both methods, as applied to C_x and C_z, as functions of $\cos\theta^{\Sigma^+}_{\text{c.m.}}$, for fixed energy E_γ.

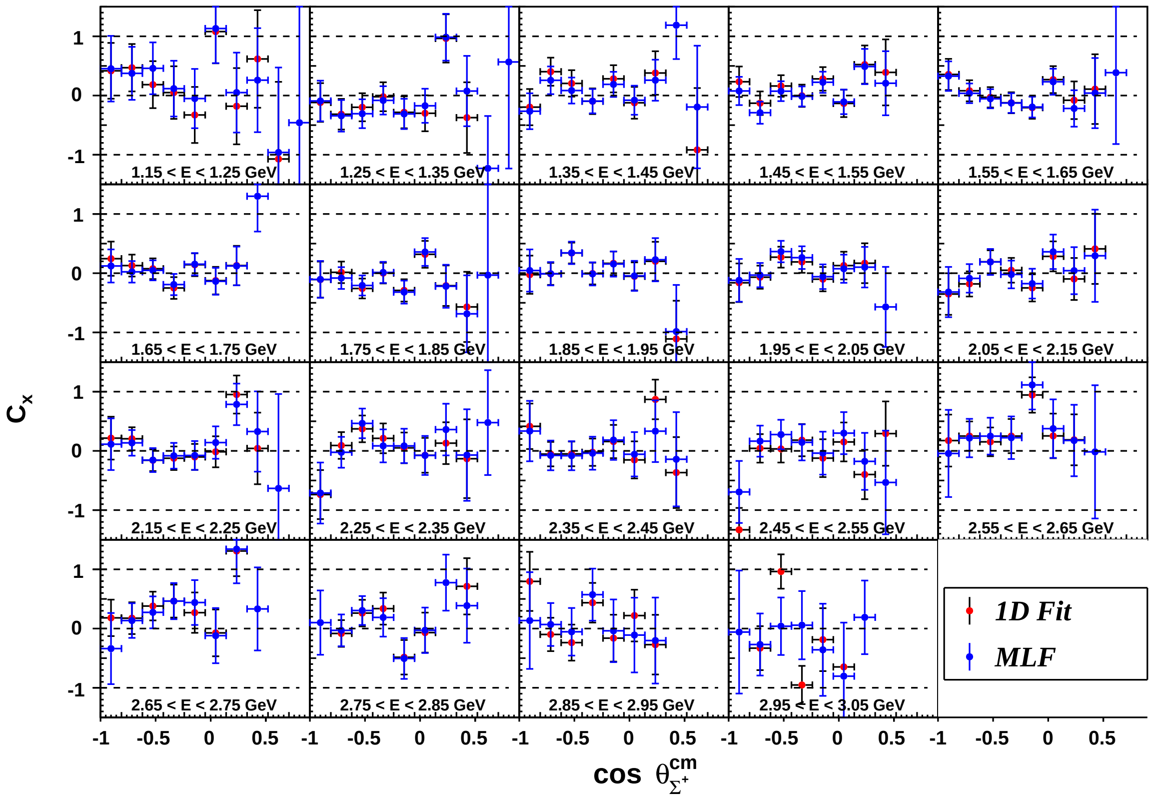

Figure 5.7: Beam-recoil polarization observable C_x for the reaction $\gamma p \to K^0\Sigma^+$, using CLAS $g12$ data, with a set of 100-MeV-wide energy bins and an incident photon energy of $1.15 < E_\gamma < 3.05$ GeV. The red dots denote the C_x observable extracted via a linear fit to the asymmetry (4.43), while the blue dots denote the same observable as obtained via the Maximum Likelihood fit method.

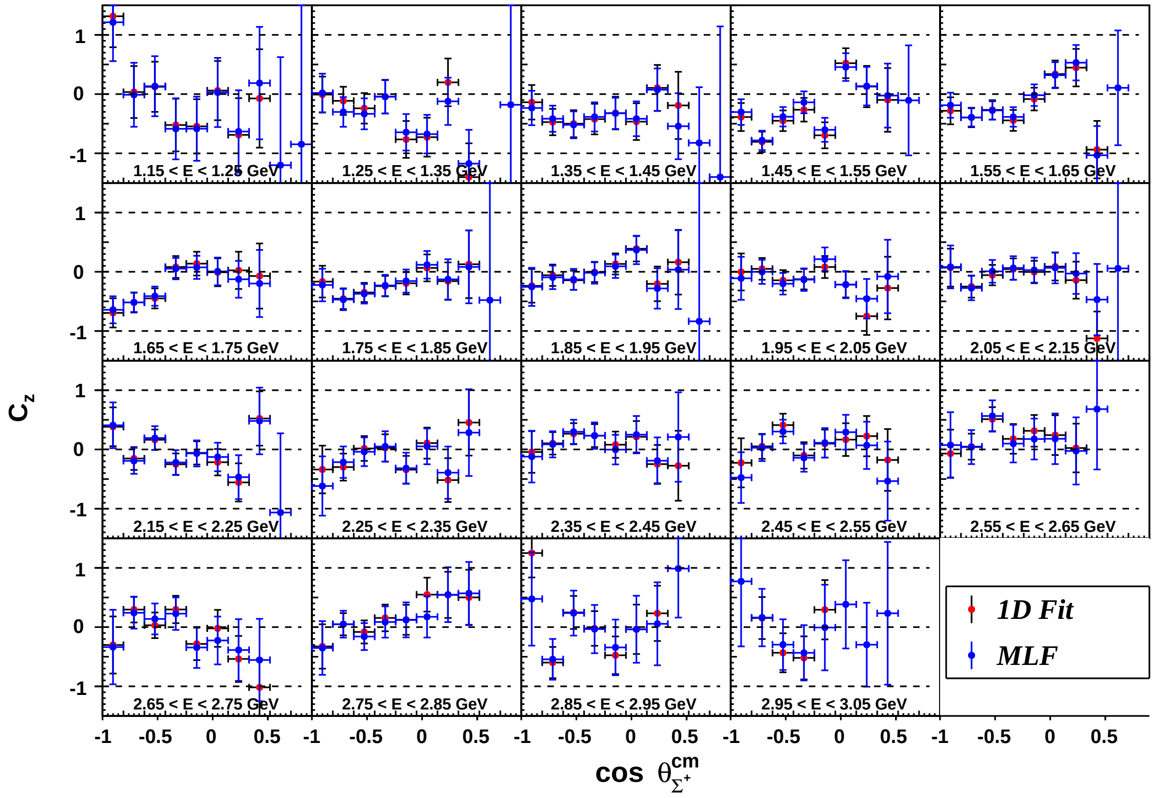

Figure 5.8: Beam-recoil polarization observable C_z for the reaction $\gamma p \to K^0\Sigma^+$, using CLAS $g12$ data, with a set of 100-MeV-wide energy bins and an incident photon energy of $1.15 < E_\gamma < 3.05$ GeV. The red dots denote the C_z observable extracted via a linear fit to the asymmetry (4.43), while the blue dots denote the same observable as obtained via the Maximum Likelihood fit method.

Figures 5.7 and 5.8 display an overall good agreement for both the C_x and C_z observables, across all energy bins (with some minor exceptions for some of the higher energy bins), between the linear (red dots) and Maximum Likelihood (blue dots) fit values. The Likelihood fit error bars are, on average, smaller than those from the linear fit. It was noticed that for both C_x and C_z observables their values remained consistently near zero for the energy and angular bins considered for this analysis. Due to their helicity dependence, both observables C_x and C_z were further binned in angles for the construction of their asymmetries. The given uncertainties of the red and blue points in Figures 5.7 and 5.8 are statistical with the $Q-$value uncertainties added in quadrature, and purely statistical, respectively. Lastly, Figures 5.9 and 5.10 display the ratio of the observable values found via the linear and Maximum Likelihood fit methods, shown in Figures 5.7 and 5.8.

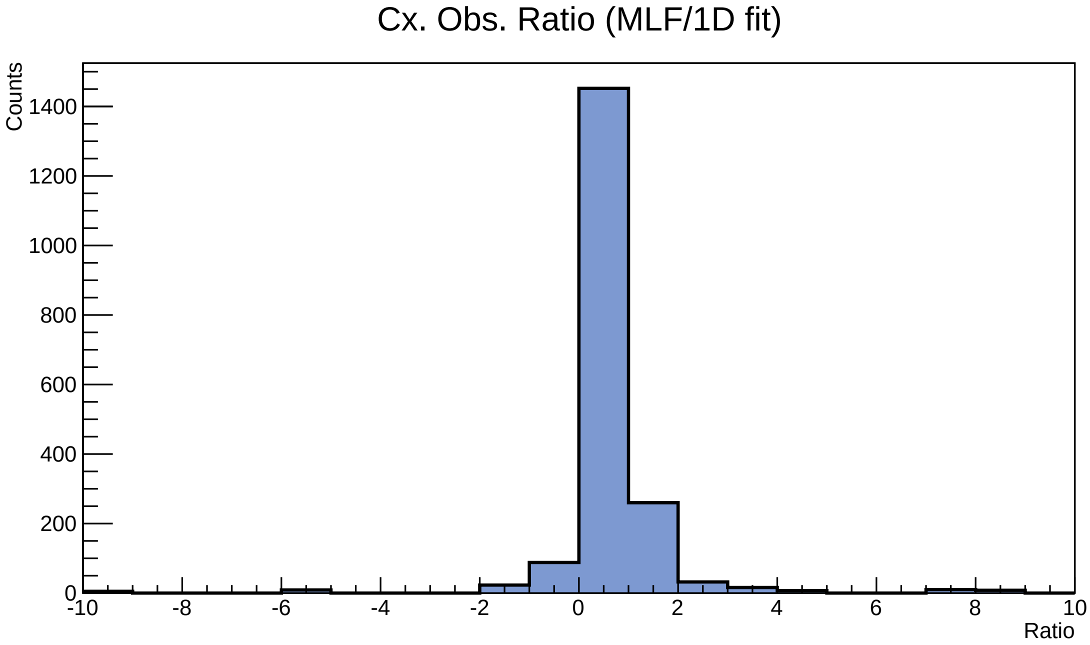

Figure 5.9: Ratio histogram of C_x observable values obtained via the ML and linear fit methods.

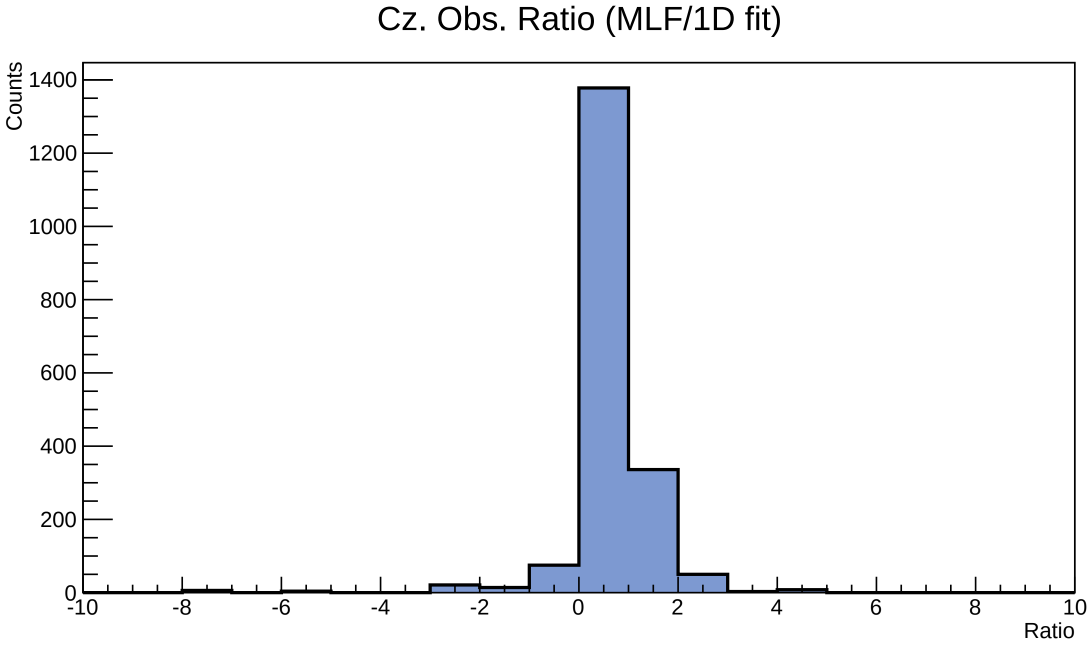

Figure 5.10: Ratio histogram of C_z observable values obtained via the ML and linear fit methods.

5.2.3 The Hyperon Polarization Observable P

Unlike the beam-recoil polarization observables C_x and C_z, the hyperon-recoil polarization observable P was helicity independent, binned exclusively in 19 incoming photon beam energy E_γ bins, and extracted via a counting experiment (see Sub-section 4.3.2). Figure 5.11 shows the hyperon polarization in the reaction $\gamma p \to K^0\Sigma^+$, extracted from CLAS $g12$ data, and compared with a previous measurement carried out by the CBELSA/TAPS Collaboration [56].

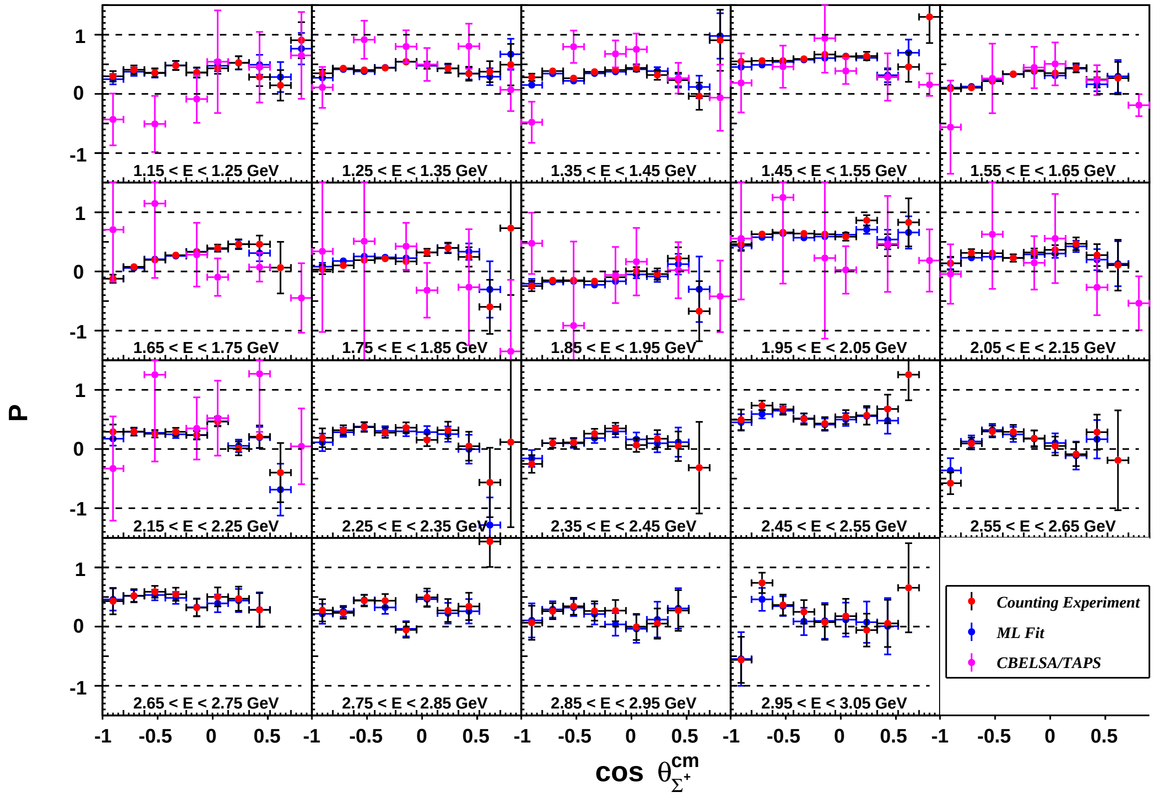

Figure 5.11: Hyperon-recoil polarization observable P for the reaction $\gamma p \to K^0\Sigma^+$, using CLAS $g12$ data, with a set of 100-MeV-wide energy bins and an incident photon energy of $1.15 < E_\gamma < 3.05$ GeV. The red dots denote the P observable as extracted using the asymmetry in (4.52), while the blue dots denote P as obtained via the Maximum Likelihood fit method, and the magenta dots show previous CBELSA/TAPS Collaboration measurements [56]. The given uncertainties for the $g12$ (red) data are statistical with the $Q-$values added in quadrature, while the Maximum Likelihood (blue) uncertainties are statistical.

Overall, good agreement was found between the counting experiment (red dots) and Maximum Likelihood fit (blue dots) measurements for the P observable, across all energy and angular bins.

Figure 5.12 shows the ratio of the observable values obtained via the 1-Dimensional and Maximum Likelihood fit methods (Figure 5.11).

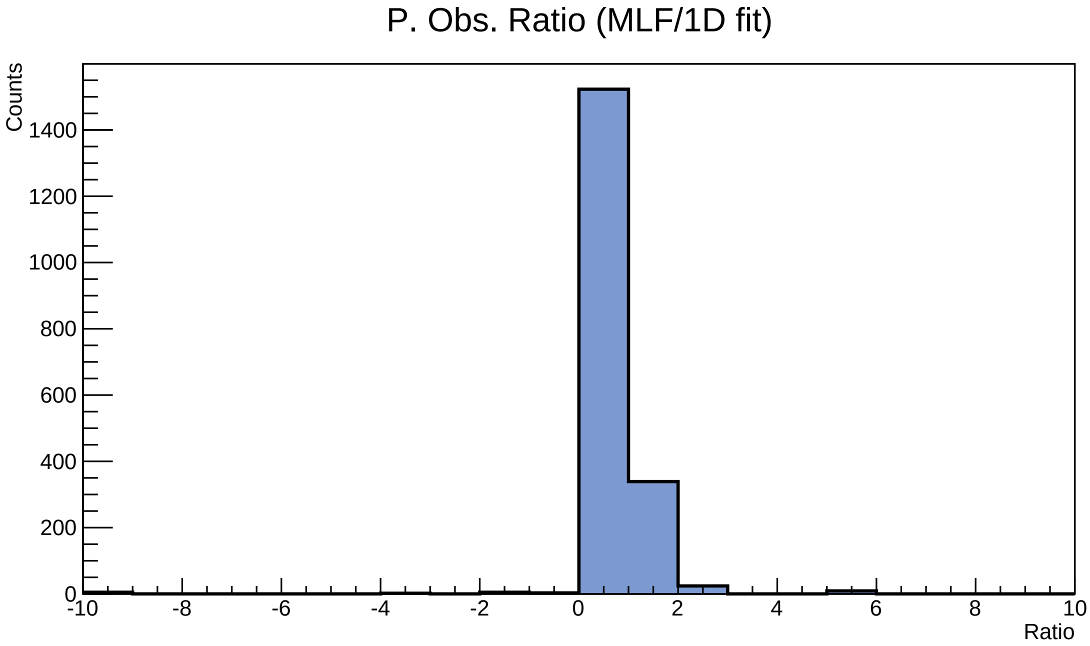

Figure 5.12: Ratio histogram of P observable values obtained via the linear and MLF methods.

Lastly, the polarization observables for $K^0\Sigma^+$ photoproduction off the proton must satisfy a set of inequalities. In particular, for a circularly polarized beam there exists the following relation [50],

$$R^2 \equiv P^2 + C_x^2 + C_z^2 \leq 1. \tag{5.15}$$

The role of expression (5.15) is to place an upper bound on the value of R^2, while not constraining it to a specific value. Given a 100% circularly polarized photon beam, the vector $\vec{R}$ would thus be equivalent to $\vec{P}_{\Sigma^+}$, given in expression (4.38). For this extreme case, the inequality in (5.15) dictates that the magnitude of the three orthogonal polarization components may take on any value, up to unity, with no *a priori* requirements on the hyperon being fully polarized, save for the forward and backward regions, in which the orbital angular momentum of the system $\vec{L}$ plays no role [50]. Furthermore, the value of R^2 serves as a systematic check for the analysis since, if the data were to yield R^2 values well outside the upper bound laid out by (5.15), then that would be indicative of a source of systematic error which would need to be subsequently eliminated.

5.3 Summary and Outlook

Among the most challenging problems currently facing nuclear physics today is understanding the underlying mechanism involved in allowing quark-gluon interactions to give rise to the protons and neutrons, which comprise all visible matter. It is within this non-perturbative regime that we find the phenomenon of *confinement*, responsible for holding quarks within the nucleon. And in spite of its awesome predictive power, the Quantum Field Theory of the strong nuclear force, Quantum Chromodynamics (QCD), cannot be analytically solved within this energy regime. In order to circumvent this glaring issue, physicists developed alternative tools, such as *baryon spectroscopy*, to attack this problem.

Similar in spirit to atomic spectroscopy, which is crucial for understanding the electromagnetic interactions within an atom, baryon spectroscopy likewise allows one to peer deeply into the QCD interactions within a baryon (a nucleon composed of three valence quarks). Through diligent and careful studies of the baryon spectrum, one can not only obtain insights into the underlying degrees of freedom within a baryon, but also gain an understanding of the baryon's dependency on the energy of the system.

However, unlike atomic spectroscopy, the study of baryon spectroscopy is far more complex due to the *overlapping* nature of its baryon resonances. Consequently, to disentangle these resonances it becomes crucial to carry out polarized experiments from which to extract sets of *polarization observables*, in addition to the differential cross sections, in order to disentangle the resonances.

Complicating matters further, the baryon spectrum is not completely understood, as there exist discrepancies between the predicted states and those that have been observed. This is known as the *missing baryon problem.* It has been proposed that these missing resonances perhaps do not couple strongly to the traditionally employed probes used to perform baryon spectroscopy, namely pion beams, but are instead predicted to couple strongly to photon beams, and preferentially decay to final-states involving heavier meson states, such as the vector mesons ω, ρ and ϕ.

The channel of interest presented in this work is the strangeness production in $\gamma p \to K^0\Sigma^+$, which has been previously understudied. The emergence of strange quarks in this reaction gives rise to another degree of freedom, thus resulting in additional information unavailable from nucleon-nucleon scattering alone. We have measured the induced hyperon observable P, along with the degree of polarization transfer from a circularly polarized photon beam to an unpolarized target in the form of the C_x and C_z observables, both of these being first-time measurements at all energies and angles for the $K^0\Sigma^+$ channel in our analysis. We employed the parity-violating weak decay α of the Σ^+ hyperon as a means of extracting its polarization P through the ensuing angular distribution of its decay products. A Maximum Likelihood fit technique was also implemented in order to extract the three aforementioned observables, simultaneously.

In spite of this progress however, the measurements extracted for this thesis do not currently offer a deeper insight into the physics of the reaction at hand, namely how to go from an initial γp state to a $K^0\Sigma^+$ final-state, let alone what happens in-between this reaction. To that end, further analyses shall be required, in the form of a Partial Wave Analysis (PWA), in order to understand the overall amplitudes (Feynman diagrams) that contribute to the final $K^0\Sigma^+$ state; additionally, finalizing the systematic uncertainties will also be a priority. The measurements of these observables were carried out using a circularly polarized photon beam, incident on an unpolarized liquid Hydrogen (lH_2) target, for the CLAS $g12$ experiment at the Jefferson Lab.

Lastly, it is hoped that our results will stimulate further research into the remaining observables pertaining to the $K^0\Sigma^+$ channel, and assist in expanding and bringing about a phenomenological understanding of the photoproduction of strangeness, and the non-perturbative nature which currently shrouds the low-energy regime of Quantum Chromodynamics in awe, and mystery.

BIBLIOGRAPHY

[1] R. A. Adelseck and B. Saghai. Kaon photoproduction: Data consistency, coupling constants, and polarization observables. *Phys. Rev. C*, 42:108, 1990.

[2] S. D. Adhikari. *Polarization Observables for $\gamma p \to K^+\Lambda$ at Photon Energies up to 5.45 GeV.* PhD thesis, Florida International University, 2018.

[3] Z. Akbar. *The Search for N^* Resonances: Measurement of Differential Cross Sections and Polarization Observables for $\gamma p \to p\omega$ and $\gamma p \to K^0\Sigma^+$ Using Circularly-Polarized Photons at CLAS, Jefferson Lab.* PhD thesis, Florida State University, 2018.

[4] W. I. Andersson. *Explorinh the Merits and Challenges of Hyperon Physics with $\overline{P}$ANDA at FAIR.* PhD thesis, Uppsala University, 2020.

[5] I. S. Barker, A. Donnachie, and J.K. Storrow. Complete Experiments in Pseudoscalar Photoproduction. *Nucl. Phys.*, B95:347–356, 1975.

[6] S. Bethke. Experimental Tests of Asymptotic Freedom. *Prog. Part. Nucl. Phys.*, 58:351–386, 2007.

[7] C. Blocker. Maximum Likelihood Primer, April 2002.

[8] T. Cao. *Determination of the Polarization Observables C_x, C_z and P_y for Final-State Interactions in the Reaction $\vec{\gamma} d \to K^+\vec{\Lambda} n$.* PhD thesis, University of South Carolina, 2016.

[9] S. Capstick and W. Roberts. Strange Decays of Nonstrange Baryons. *Prog. Rev. D.*, 58:074011, 1998.

[10] S. Capstick and W. Roberts. Quark Models of Baryon Masses and Decays. *Prog. Part. Nucl. Phys.*, 45:S241–S331, 2000.

[11] R. J. J. Castelijn. *"Photoproduction of strange mesons and hyperons on the proton.* PhD thesis, University of Groningen, 2006.

[12] G. F. Chew, M. L. Goldberger, F. E. Low, and Y. Nambu. Application of Dispersion Relations to Low-Energy Meson-Nucleon Scattering. *Phys. Rev.*, 106:1345, 1957.

[13] Wen-Tai Chiang and Frank Tabakin. Completeness Rules for Spin Observables Pseudoscalar Meson Photoproduction. *Phys. Rev.*, C55:2054–2066, 1997.

[14] S. Christo. The g11a Target Cell. `http://www.jlab.org/christo/g11atarget.html`.

[15] Louise Clark. Private communication; CLAS Collaboration Meeting, November 2019.

[16] T. Corthals, T. Van Cauteren, J. Ryckebusch, and D. G. Ireland. Regge-Plus Resonance Treatment of the $p(\gamma, K^+)\Sigma^0$ and $p(\gamma, K^0)\Sigma^+$ Reactions at Forward Kaon Angles. *Phys. Rev. C*, 75:045204, 2007.

[17] V. Crede and W. Roberts. Progress Towards Understanding Baryon Resonances. *Rept. Prog. Phys.*, 76:076301, 2013.

[18] J. W. Cronin and O. E. Overseth. Measurement of the Decay Parameters of the Λ^0 Particle. *Phys. Rev.*, 129:1795, 1963.

[19] M. Dugger and C. Hanretty. Correction to the incident-photon energy for g8b data. *CLAS Note*, 2009-030, 2009.

[20] Ashley Ernst. Private communication.

[21] Steve Gagnon. Originally posted on the Jefferson Lab Site Tour website. `http://education.jlab.org/sitetour/guidedtour05.l.alt.html`.

[22] M. Gell-Mann and A. Pais. Behavior of Neutral Particles under Charge Conjugation. *Phys. Rev*, 97:1387, 1955.

[23] Derek Glazier. Analysis Tools for CLAS12: Application of RooFit. CLAS Joint Working Groups, Jefferson Lab, 2019.

[24] C. Gleason and Y. Ilieva [CLAS Collaboration]. Determination of the Polarization Observables C_x, C_z and P for the $\gamma d \to K^0\Lambda(p)$ Reaction. *Few-Body Syst.*, 59:129, 2018.

[25] S. Godfrey and N. Isgur. Mesons in a relativized quark model with chromodynamics. *Phys. Rev. D*, 32:189, 1985.

[26] D. Griffiths. *Introduction to Elementary Particles.* ISBN 978-3-527-40601-2, WILEY-VCH, 2 edition, 2008.

[27] C. Hanretty. *Measurements of The Polarization Observables I^S and I^C for $\gamma p \to p\pi^+\pi^-$ Using The CLAS Spectrometer.* PhD thesis, Florida State University, 2011.

[28] F. James. MINUIT Function Minimization and Error Analysis: Reference Manual Version 94.1, 1994.

[29] G. Knöchlein, D. Drechsel, and L. Tiator. Photo- and electroproduction of eta mesons. *Phys. A*, 352:327, 1995.

[30] Jefferson Laboratory. CLAS - Magnets. `https://www.jlab.org/Hall-B/album/CLAS%20-%20Magnets/index.html#HallB-torus-empty.jpeg`.

[31] Jefferson Laboratory. CLAS - Start Counter. `https://www.jlab.org/Hall-B/album/CLAS%20-%20Start%20Counter/index.html#100_1812.jpg`.

[32] Jefferson Laboratory. The Jefferson Lab Picture Exchange. `https://www.flickr.com/photos/jeffersonlab/32094641754/`.

[33] Jefferson Laboratory. The Jefferson Lab Picture Exchange. `https://www.flickr.com/photos/jeffersonlab/24150599344/`.

[34] C. Langenbruch. Parameter uncertainties in weighted unbinned maximum likelihood fits. *arXiv e-prints*, page arXiv:1911.01303, 2019.

[35] H. Olsen and L. C. Maximon. Photon and Electron Polarization in High-Energy Bremsstrahlung and Pair Production with Screening. *Phys. Rev.*, 114:887, 1959.

[36] E. Pasyuk. Energy-loss corrections for charged particles in CLAS. *CLAS Note*, 2007-016, 2007.

[37] Charles E. Reece. Continuous Wave Superconducting Radio Frequency Electron Linac for Nuclear Physics Research. *Phys. Rev. Accelerators and Beams*, 19:124801, 2016.

[38] K. Romines. Photoproduction of $K^0\Sigma^+$ at CLAS. B.S., Honor's Thesis, Florida State University, 2017.

[39] C. Rosemann. Parameter Estimation Part A: The Likelihood Method, November 2014.

[40] P. Roy. *Measurement of Polarization Observables in Vector Meson Photoproduction Using a Transversely-Polarized Frozen-Spin Target and Polarized Photons at CLAS, Jefferson Lab.* PhD thesis, Florida State University, 2016.

[41] J. J. Sakurai and J. Napolitano. *Modern Quantum Mechanics.* ISBN 978-0-8053-8291-4, Addison-Wesley, 2 edition, 2010.

[42] Jean Tate. Atomic Spectra. Originally published on the website Universe Today. `https://www.universetoday.com/50883/atomic-spectra/`.

[43] B.A. Mecking *et al.* The CEBAF large acceptance spectrometer (CLAS). *Nucl. Instrum. Meth.*, A 503:513, 2003.

[44] C. S. Nepali *et al.* Transverse polarization of $\Sigma^+(1189)$ in photoproduction on a hydrogen target in CLAS. *Phys. Rev. C*, 87:045206, 2013.

[45] D. I. Sober *et al.* The Bremsstrahlung Tagged Photon Beam in Hall B at JLab. *Nucl. Instrum. Meth.*, A 440:263, 2000.

[46] D. S. Carman *et al.* First Measurement of Transferred Polarization in the $\gamma p \to K^+\Lambda$ in Polarized-Lambda Reaction. *Phys. Rev. Lett.*, 90:131804, 2003.

[47] E. S. Smith *et al.* The Time-of-Flight System for CLAS. *Nucl. Instrum. Meth.*, A 432:265, 1999.

[48] M. D. Mestayer *et al.* The CLAS Drift Chamber System. *Nucl. Instrum. Meth.*, A 449:81, 2000.

[49] M. G. Doncel *et al.* Properties of Polarization Density Matrix in Regge-Pole Models. *Phy. Rev. D*, 7:815, 1973.

[50] R. Bradford *et al.* First Measurement of Beam-Recoil Observables C_x and C_z in Hyperon Photoproduction. *Phys. Rev. C*, 75:035205, 2007.

[51] R. Dupré *et al.* A radial time projection chamber for α detection in CLAS at JLab. *Nucl. Instrum. Meth.*, A 898:90, 2018.

[52] R. G. Edwards *et al.* Excited State Baryon Spectroscopy from Lattice QCD. *Phys. Rev. D*, 84:074508, 2011.

[53] S. Stepanyan *et al.* Energy Calibration of the JLab Bremsstrahlung Tagging System. *Nucl. Instrum. Meth.*, A 572:654, 2007.

[54] Z. Akbar *et al.* g12 Analysis Procedures, Statistics and Systematics. *CLAS Note*, 2017-002, 2017.

[55] Z. Akbar *et al.* Study of Meson Photoproduction resulting in Multitrack-Final States using CLAS-g12 Data. 2018.

[56] R. Ewald *et al.* [CBELSA/TAPS Collaboration]. Measurement of polarisation observables in $K^0_s\Sigma^+$ photoproduction off the proton. *Phys. Lett. B*, 738:268, 2014.

[57] T. Hu *et al.* [CLAS Collaboration]. Photoproduction of η mesons off the proton for $1.2 < E_\gamma < 4.7$ GeV using CLAS at Jefferson Laboratory. *arXiv e-prints*, page arXiv:2006.01361, 2020.

[58] R. Aaij *et al.* [LHCb Collaboration]. Observation of $J/\psi p$ Resonances Consistent with Pentaquark States in $\Lambda^0_b \to J/\psi K^- p$ Decays. *Phys. Rev. Letters*, 115:072001, 2015.

[59] C. Patrignani *et al.* [Particle Data Group]. Review of Particle Physics. *Chin. Phys. C*, 40(10):100001, 2016.

[60] J. Beringer *et al.* [Particle Data Group]. Review of Particle Physics. *Phys. Rev. D*, 86:010001, 2012.

[61] M. Tanabashi *et al.* [Particle Data Group]. Review of Particle Physics. *Phys. Rev. D*, 98:030001, 2018.

[62] W.-M. Yao *et al.* [Particle Data Group]. Review of Particle Physics. *J. Phys. G*, 33:1, 2006.

[63] E. Thomé. *Multi-Strange and Charmed Antihyperon-Hyperon Physics for PANDA*. PhD thesis, Uppsala University, 2012.

[64] M. Thomson. *Modern Particle Physics*. ISBN 978-1-107-03426-6, Cambridge University Press, 1 edition, 2013.

[65] M. Williams. *Measurements of Differential Cross Sections and Spin Density Matrix Elements along with a Partial Wave Analysis for* $\gamma p \rightarrow p\omega$ *using CLAS at Jefferson Lab*. PhD thesis, Carnegie Mellon University, 2007.

[66] M. Williams, M. Bellis, and C. A. Meyer. Multivariate side-band subtraction using probabilistic event weights. *J. Instrum.*, 4:P10003, 2009.

BIOGRAPHICAL SKETCH

The author obtained a B.S. in Physics (with a minor in Mathematics) at the California Polytechnic State University, San Luis Obispo, on Spring of 2018. As an undergraduate student, he performed research on experimental nuclear physics under the direction of Dr. Jennifer Klay as part of the NIFFTE Collaboration. His research resulted in a poster and an *APS Far West Research Meeting* talk titled: "*Investigating the Kinematics of Neutron Induced Fission*", given at the University of California, Davis, during the Fall of 2016. Subsequently, he worked on a study pertaining to alpha accompanied fission using Monte Carlo simulations, also under the supervision of Dr. Klay.

Working on more theoretical grounds, the author moved on to perform research in the realm of Lorentz and CPT violations, under the guidance of Dr. Matthew Mewes. The author's research consisted of simplifying the mathematical complexity of a given perturbation expansion of the Newtonian gravitational potential. Along the way, his advisor and him found a new way of reformulating the spherical harmonics into symmetric trace-free tensors. This proved to be a brand new way of dealing with the spherical harmonics that will extend well-beyond the domain of Lorentz violations. This research resulted in a poster titled: "*Lorentz-Violating Gravitational Potentials*", and was subsequently presented at the *2018 Standard Model Extension Summer School*, held at Indiana University, Bloomington. Furthermore, the fruits of this project resulted in a publication titled: *Spherical-harmonic tensors*, that, at the time of this writing, is currently under review.

During the Fall of 2018, the author began graduate school (working on an M.S.) with the Physics Department at Florida State University. This time around, the author performed research in the field of hadronic spectroscopy, under the direction of Dr. Volker Credé, for the CLAS Collaboration. Working with $g12$ data recorded at the Jefferson Lab, the author searched for a set of polarization observables $\{C_x, P, C_z\}$ stemming from the under-explored photoproduction reaction $\gamma p \to K^0\Sigma^+$. This research resulted in two talks given at JLab, titled: "*Measurement of Polarization Observables for the reaction* $\gamma p \to K^0\Sigma^+$." The labor of this work resulted in an M.S. in Physics, and a future paper, to be published sometime within the near future (around Fall 2021).

In the next chapter of his graduate school adventures, the author will continue his Physics education and begin pursuing a Ph.D. in Computational Nuclear Particle Physics at the University of California, Davis, beginning in the Fall of 2020.